INTERDIFFUSION BEHAVIOR OF U-Mo ALLOYS IN CONTACT WITH Al AND Al-Si ALLOYS

by
EMMANUEL PEREZ
B.E. Columbia University, 1995
M.S. University of Central Florida, 2005

A dissertation submitted in partial fulfillment of the requirements
for the degree of Doctor of Philosophy
in the Department of Mechanical, Materials and Aerospace Engineering
in the College of Engineering and Computer Science
at the University of Central Florida,
Orlando, Florida

Spring Term
2011

Major Professor: Dr. Y.H. Sohn

ABSTRACT

U-Mo dispersion and monolithic fuels embedded in Al-alloy matrix are under development to fulfill the requirements of research reactors to use low-enriched molybdenum stabilized uranium alloys as fuels. The system under consideration in this study consisted of body centered cubic (γ) U-Mo alloys embedded in an Al structural matrix. Significant interaction has been observed to take place between the U-Mo fuel and the Al matrix during manufacturing of the fuel-plate system assembly and during irradiation in reactors. These interactions produce Al-rich phases with physical and thermal properties that adversely affect the performance of the fuel system and can lead to premature failure.

In this study, interdiffusion and microstructural development in the U-Mo vs. Al system was examined using solid-to-solid diffusion couples consisting of U-7wt.%Mo, U-10wt.%Mo and U-12wt.%Mo vs. pure Al, annealed at 600°C for 24 hours. The influence of Si alloying addition (up to 5 wt.%) in Al on the interdiffusion microstructural development was also examined using solid-to-solid diffusion couples consisting of U-7wt.%Mo, U-10wt.%Mo and U-12wt.%Mo vs. pure Al, Al-2wt.%Si, and Al-5wt.%Si annealed at 550°C for 1, 5 and 20 hours. To further clarify the diffusional behavior in the U-Mo-Al and U-Mo-Al-Si systems, Al-rich 85.7Al-11.44U-2.86Mo, 87.5Al-10U-2.5Mo, 56.1Al-18.9Si-21.9U-3.1Mo and 69.3Al-11.9Si-18.8U (at.%) alloys were cast and homogenized at 500°C to determine the equilibrium phases of the system. Scanning electron microscopy (SEM), transmission electron microscopy (TEM) and electron probe microanalysis (EPMA) and X-ray diffraction (XRD) were employed to examine the phase development in the diffusion couples and the cast alloys.

In ternary U-Mo-Al diffusion couples annealed at 600°C for 24 hours, the interdiffusion microstructure consisted of finely dispersed UAl_3, UAl_4, $U_6Mo_4Al_{43}$, and UMo_2Al_{20} phases while the average composition throughout the interdiffusion zone remained constant at approximately 80 at.% Al. The interdiffusion microstructures observed by EPMA, SEM and TEM analyses were correlated to explain the observed morphological development in the interdiffusion zones. The concept of thermodynamic degrees of freedom was used to justify that, although deviations are apparent, the interdiffusion zones did not significantly deviate from an equilibrium condition in order for the observed microstructures to develop. Selected diffusion couples developed periodic bands within the interdiffusion zone as sub-layers in the three-phase regions. Observation of periodic banding was utilized to augment the hypothesis that internal stresses play a significant role in the phase development and evolution of U-Mo vs. pure Al diffusion couples.

The addition of Si (up to 5 wt.%) to the Al significantly reduced the growth rate of the interdiffusion zone. The constituent phases and composition within the interdiffusion zone were also modified. When Si was present in the Al terminal alloys, the interdiffusion zones developed layered morphologies with fine distributions of the $(U,Mo)(Al,Si)_3$ and UMo_2Al_{20} phases. The $U_6Mo_4Al_{43}$ phase was observed scarcely in Si depleted regions within the interdiffusion zone. The phase development and evolution of the interdiffusion zone was described in terms of thermodynamic degrees of freedom with minimal deviations from equilibrium.

This dissertation is dedicated to my family and friends who guided me through my life and who helped me become the person I am. This document is, above all, dedicated to all the lives and the environments that may be preserved as result of the work presented here.

ACKNOWLEDGMENTS

This work was financially supported by Idaho National Laboratory (Contract No. 00051953) under the operation of U.S. Department of Energy – Battelle Energy Alliance, LLC (DE-AC07-05ID14517). I would like to thank Dr. Yong-ho Sohn for his support, encouragement and advice throughout my career at the University of Central Florida (UCF), for the education he provided and for serving as the chair of the dissertation committee. I would also like to thank Dr. Dennis D. Keiser, Jr. for the opportunity to engage in the work discussed in this document and for his service as a committee member. I would like to express my gratitude to the additional committee members, Dr. Linan An, Dr. Kevin Coffey, Dr. Helge Heinrich and Dr. Challapalli Suryanarayana for all the education they provided me and for taking the time to examine and critique this document.

I would like to express my gratitude to all of my coworkers for their continuous help with the laboratory facilities and experiments. Special thanks to Ashley Ewh, who helped set up the laboratory for radioactive materials handling, helped with the initial experiments, and helped develop the experimental procedures that became standard procedures to the laboratory facility.
I would also like to thank all of the Advanced Materials Processing and Analysis (AMPAC) faculty and staff for their teachings and support throughout my years of study.

TABLE OF CONTENTS

LIST OF FIGURES

LIST OF TABLES

1. INTRODUCTION

Research and test reactors, commonly referred to as non-power reactors, are a class of nuclear reactors designed for the purposes of research, development, and training. The primary purpose of these reactors is to provide sources of neutron or gamma radiation for scientific development. The Reduced Enrichment Fuels for Research Test Reactors (RERTR) program [1] was introduced in 1978 by the United States Department of Energy (DOE) in order to minimize the use of U^{235} fissile isotope in research and test reactors. The program is managed by the Office of Nuclear Material Threat Reduction within the National Nuclear Security Administration (NNSA). The RERTR program targets to develop the technologies necessary to implement the use of low-enriched-uranium (LEU) fuels in these reactors; fuels with U^{235} to U^{238} isotope concentrations lower than 20% are considered LEU [2,3]. The program seeks to develop technologies for new reactor designs, and reduce the enrichment of high-enriched-uranium (HEU) fuels in research reactors originally designed to use HEU. Most research reactors have been converted to use LEU with existing technologies. Some reactors still require fuel redesign to safely achieve the required fuel densities for reactor operations. In order to convert these reactors, the RERTR program initiated an investigation to consider the use of very high density U-Mo fuels.

This study focuses on the class of fuels of γ-U-Mo alloys encased in Al. U-Mo alloys have undergone extensive research to determine the phase equilibrium [4-35] and irradiation stability [36-43] of the phases in order to determine the alloy's potential as a fuel. The γ-U-Mo phase alloy is able to provide a high uranium density, and the γ-U phase was found to be stable under irradiation conditions at low temperature. The Al serves structural purposes, and it is preferred because of its low neutron absorption [44], good corrosion resistance and high thermal conductivity. During fabrication and irradiation, U-Mo and Al were found to readily interact and experience complex interactions [45-62]. The interaction products have lower U-densities than desired for normal reactor operations; they have significantly larger molar volumes than the parent alloys which results in volumetric expansion of the bulk fuel plate system [45]. Deformation requires that internal stresses develop between the U-Mo and the Al alloys. These stresses can lead to failure due to fracturing at the interaction regions between the alloys, and can affect the microstructural development of the interaction regions between the U-Mo and the Al. Periodic layer development within the microstructures of some of the U-Mo vs. Al diffusion couples in this study was used as an indication of stress within the interdiffusion zones, and was used to explain the observed morphologies.

Sample dispersion or monolithic fuel plates can be used to analyze the interdiffusion zones that develop due to interactions between U-Mo and Al in these systems. However, the plate manufacturing processes may introduce variables, such as contamination/impurities, temperature and/or pressure variations that may influence the development of the interaction regions. Other complications involve oxidation of the alloy surfaces prior to plate assembly, which prevents proper bonding of the alloys, and is not desired. Furthermore, reactor plate assemblies are typically manufactured with commercial alloys (6061Al) that typically contain element additions of Si, Fe, Cu, Mn, Mg, Cr, Zn, Ti and other trace elements; these elements tend to interact within the interdiffusion zones to develop unexpected phases that modify the observed microstructures.

This study was carried out to develop a fundamental understanding of the phase and microstructural development that takes place due to diffusional interactions between the U-Mo and Al. Diffusion couple experiments with high purity U-7wt.%Mo, U-10wt.%Mo and U-12wt.%Mo versus Al, Al-2wt.%Si and Al-5wt.%Si alloys were used in this study to examine the microstructural and phase development in detail. Diffusion couple experiments allowed for experiments to be conducted under controlled isothermal conditions and atmospheres, and allowed for detailed characterization of the interdiffusion zone's microstructural and phase development through Scanning Electron Microscopy (SEM), Electron Probe Microanalysis (EPMA), and Transmission Electron Microscopy (TEM). Complex microstructures and phase distributions were observed within the interdiffusion zones. Combination of the data from several diffusion couple assemblies allowed for the study of the microstructural and phase evolution of the interdiffusion zone in the U-Mo/Al system as a function of time and composition, and allowed for confirmation of the growth constant as a function of composition. The results from the diffusion couples were then used to suggest modifications to the current fuel plate system designs to improve performance and increase irradiation stability.

Although, through the progress of this study, other parallel studies [45-62] have carried out characterization of the interaction regions between U-Mo and Al, this study carried out a detailed analysis of the interdiffusion zone through TEM characterization to determine the precise location and distribution of the different phases observed in the U-Mo vs. Al diffusion couples, and to explain the observed typical morphological development. Confirmation of the phase development and phase equilibria under the annealed conditions was carried out through analysis of castings of Al-rich U-Mo-Al alloys through x-ray diffraction (XRD), SEM and TEM, where the alloys' compositions were chosen to represent that typically observed in the interdiffusion zones of diffusion couples. Contributions were made to the Al-rich side of the ternary U-Mo-Al phase diagram at 500°C based on the results of the study [62].

Irradiation experiments [63-66] on U-Mo/Al samples have shown that the $U_6Mo_4Al_{43}$ phase performs poorly under irradiation. In order to affect the phase development to mitigate or eliminate this phase from the interdiffusion zone, Si was added to the Al in diffusion couples of U-Mo vs. Al-Si. Characterization by SEM and TEM was carried out to develop a detailed understanding of the phase development and distributions in this system. Complex microstructures and reduced interaction rates are reported along with the minimization of the $U_6Mo_4Al_{43}$ phase in the interdiffusion zones. Confirmation of the phase development and phase stability was confirmed through Al-rich U-Mo-Al-Si alloys with compositions chosen, again, to closely match the observed average composition of the interdiffusion zones. Based on the observed positive effects of Si, suggestions are made to design a more effective fuel system.

2. LITERATURE REVIEW

2.1 Reduced Enrichment for Research Test Reactors Program

Interactions between U-Mo alloys and Al have gained interest due to the systems application as nuclear fuels. U-Mo alloys can achieve high U-density [2,3], necessary for reactor operations, allowing for the reduction of fissile U^{235} from the alloy while maintaining the densities necessary to maintain proper nuclear reactions. The Reduced Enrichment Fuels for Research test Reactors (RERTR) program [1] was introduced in 1978 by the United States Department of Energy (DOE) in order to minimize the use of U^{235} fissile isotope in research and test reactors. The program is managed by the Office of Nuclear Material Threat Reduction within the National Nuclear Security Administration (NNSA). The RERTR program targets to develop the technologies necessary to implement the use of low-enriched-uranium (LEU) fuels in these reactors: fuels with U^{235} to U^{238} isotope concentrations lower than 20% are considered LEU [2,3]. The program seeks to develop technologies for new reactor designs, and to convert reactors that use high-enriched-uranium (HEU) fuels to LEU fuels in research and test reactors originally designed to use HEU. Most research reactors have been converted to use LEU with existing technologies. Some reactors still require fuel redesign to safely achieve the required fuel densities for reactor operations. In order to convert these reactors, the RERTR program initiated an investigation to consider the use of very high density U-Mo fuels. Two types of these fuels are U-Mo alloy dispersions and U-Mo monolithic type fuels where the fuel is a thin foil encased in Al alloy (6061Al) cladding.

The U-Mo and the Al alloys were found to experience a set of complex and adverse interactions that can result in fuel system failure. The interaction products have lower U-densities than desired for proper reactor operations [45]. These products also have lower thermal conductivities than the parent alloys [46,47] that result in heat concentration, that in turn, results in accelerated reaction rates between the U-Mo and the Al. The interaction products also have different molar volumes than the parent alloys that result in residual stress concentration at the interaction regions between the U-Mo and the Al alloys. These stresses can lead to failure due to fracturing at the interaction regions between the alloys, and affect the development of the interaction regions between the U-Mo and the Al; they are discussed in more detail below.

2.2 Research Test Reactors

Research and test reactors [67] are a class of nuclear reactors used for the purposes of irradiation studies or as neutron sources rather than power generation. They range in size from 0.1watt to about 100MW; the Advanced Test Reactor (ATR) at the Idaho National Laboratories (INL) for example has a maximum power output of 250MW. Typical power reactors on the other hand tend to operate in the 1GW range. The low power outputs of research reactors reduce the risk of reactor failure, and make them ideal for safe installation at universities or other similar research facilities.

These reactors can be separated into three groups [67] according to their typical application. The first type includes low power reactors typically found at universities and are used for the purposes of basic science, and activation studies. Another type of reactor is used for materials testing and can produce high neutron flux for high irradiation studies. The third type provides an intermediate power range and is typically used for testing prototype fuel elements, the coolants, or a prototype mechanism to operate other reactors.

Prior to the inception of the RERTR program in 1978, research reactors typically operated with Highly-Enriched-Uranium (HEU) composed of UAl_x-Al dispersions, U_3O_8/Al dispersions and $UZrH_x$ alloy fuels with fuel loading densities of 1.7, 1.3 and 0.5 g/cm^3 respectively[68, 69]. Since 1978, these reactors have been undergoing decommissioning or conversion to use Low-Enriched-Uranium (LEU) fuels. The UAl_x-Al, U_3O_8/Al and $UZrH_x$ alloy fuels have also been qualified as LEU fuels with 2.3, 3.2, 3.7 g/cm^3 loading densities[68, 69]. Other qualified fuels include U_3Si_2/Al dispersions, with 4.8 g/cm^3. U_3Si/Al fuels did not meet safety requirements for reactor operation. U-Mo fuels are in the process of qualification because the metastable γ-U-Mo can provide a high uranium density and the phase is stable under irradiation [36-39].

2.3 U-Mo Alloys

The equilibrium binary U-Mo phase diagram [4,5,70] is shown in Figure 1. The γ-U-Mo phase has a body-centered-cubic (bcc) crystal structure, Im-3m (229) [71], with solubility for Mo. Extensive early studies in the U-Mo system [4-42] were carried out in order to develop an understanding on the phase equilibria in this system. Relevant to this study, the works of Dwight [16], O.S. Ivanov et al. [17, 18] and Streets et al. [19] reported the $\gamma \rightarrow (\alpha+\delta)$ decomposition, where the α-phase, orthorhombic Cmcm (63) [72], has a Mo solubility limit of approximately 0.12 at% at 600°C according to Comozov et al.[20], and the δ-phase is U_2Mo with a tetragonal, I4/mmm (139) crystal structure[73,74]. The Mo stabilizes the γ-U phase in the alloy, delaying the γ→(α+δ) decomposition at low temperature, while maintaining the U-density necessary for proper reactor operation. P.E. Repas et al. [21] and Y. Golstein et al. [22] developed the Time-Temperature-Transformation (TTT) diagrams for U-Mo alloys ranging from 8 to 14 wt.% Mo reporting the γ-phase stability as a function of Mo concentration. S.C Parida et al. [23] reported the thermodynamic functions to explain the phase stability of the γ-phase. Figure 2 shows the U-10Mo TTT diagram summarizing the alloy's phase transformations.

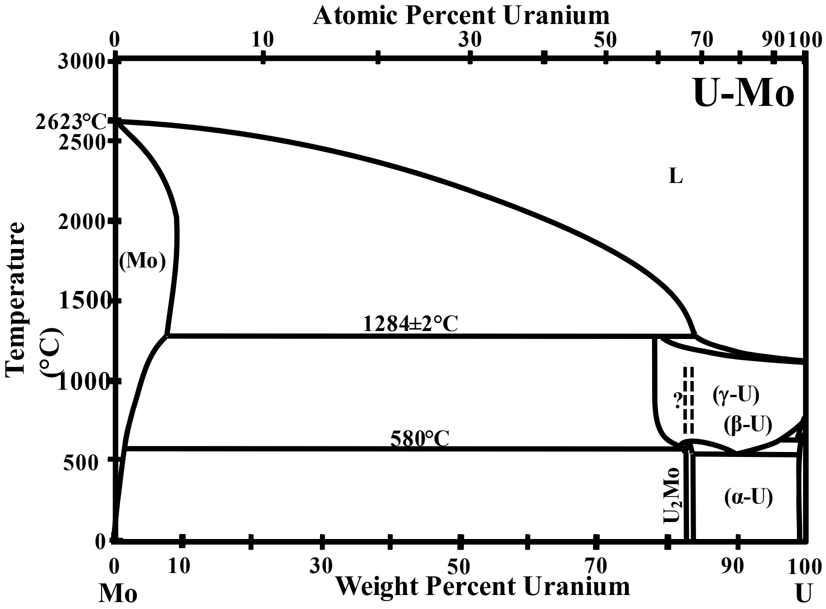

Figure 1. Binary U-Mo phase diagram [70].

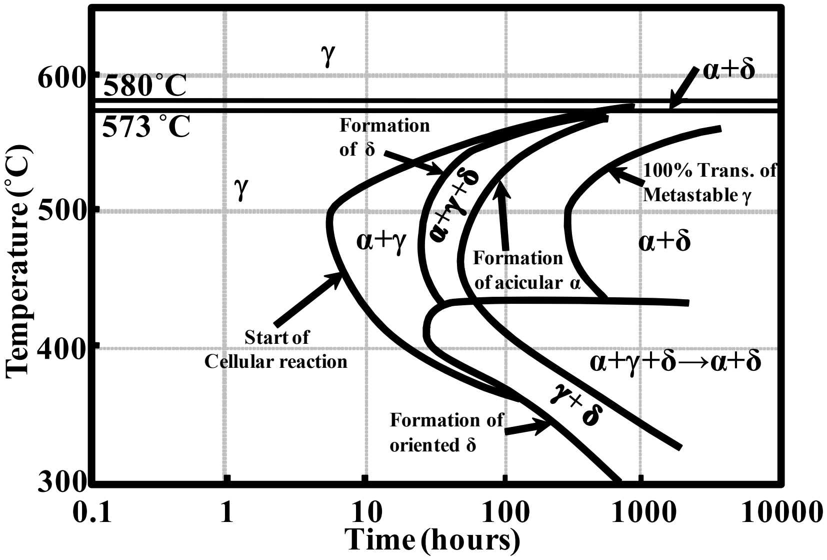

Figure 2. Time-Temperature-Transformation diagram for U-10 wt.%Mo [21].

Under irradiation the γ-U phase is considered stable [36-42]. At low temperature the γ→(α+δ) decomposition takes place. However, S.T. Konobeevsky [29,30] first reported that this two-phase region, where the (α+δ) phases are in equilibrium, the (α+δ) phase region reverts back to the high temperature γ-U phase upon irradiation. M.L. Bleiberg et al. [36,37,38], later confirmed this and provided a possible mechanism to explain this phenomenon.

Although higher purity U-alloys in the α- and β-phase regions in the U-Mo binary phase diagram may achieve high U-densities (up to 19 g/cm^3) at room temperature [1], the works by R.F. Hills et al. [24, 25], G.H. May [26], D.J. Marsh [27] and G.I. Terekhov [28] considered effects of cooling rates on rapidly-quenched alloys. They showed that the high temperature γ-U phase cannot be maintained in low Mo content alloys. R.F. Hills et al. [24,25] considered alloys with 2.5 to 15 at.% Mo, and further showed that, in alloys containing 2.5 at.% Mo or higher, decomposition of the γ-phase follows the γ→(α+δ) path directly without the development of intermediate phases. G.H. May [26] studied U-5at.% Mo alloy annealed samples after quenching and reported the phase development from 15 seconds to 1000 hours at 550°C. The α and δ phases are observed within a minute of anneal time, suggesting the rapid transformation kinetics at this temperature and composition. D.J. Harsh [27] showed that on cooling at rates greater than 4000 °C/min, a martensitic α-phase develops.

2.4 Al and Al-Si alloys

Al alloys are commonly used as the dispersion's matrix in U-Mo dispersion fuel systems. Al has face-centered-cubic, Fm-3m (225) [75], crystal structure, and melts at 660°C. Si has a diamond cubic, Fd-3m (227), crystal structure [76] and melts at 1412°C. The equilibrium binary Al-Si phase diagram [77] in Figure 3 shows that Al and Si have low solid solubilities for each other in the solid state.

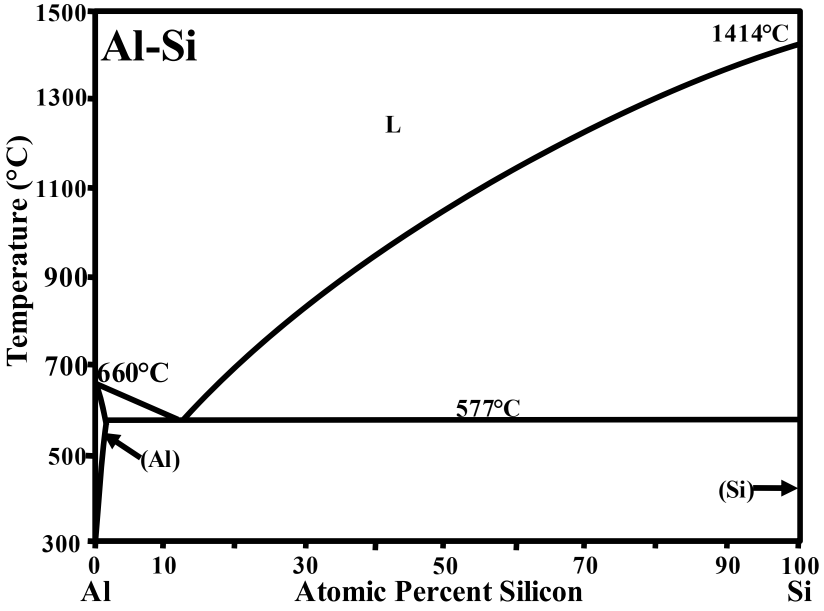

Figure 3. Binary Al-Si phase diagram [77].

2.5 Al-rich U-Mo-Al and U-Mo-Al-Si Cast Alloys

Al-rich cast U-Mo-Al alloys with compositions near to the average compositions of the interaction regions between U-Mo and Al have been studied in parallel to develop a better understanding of the phase development in the system. D.D Keiser [60] prepared alloys with compositions $U_{0.8}Mo_{0.2}Al_6$ (85.7Al-11.44U-2.86Mo at.%) and $U_{0.8}Mo_{0.2}Al_7$ (87.5Al-10U-2.5Mo at.%) and annealed them at 500°C for 200 hours. Based on wavelength dispersive spectroscopy (WDS), they observed the UAl_3 and $(U,Mo)_{0.9}Al_4$ in the as cast condition, and the $U_{0.9}Al_4$, $(U,Mo)_{0.9}Al_4$ with remaining excess Al in the annealed condition, and suggested that the observed $(U,Mo)_{0.9}Al_4$ may be the $U_6Mo_4Al_{43}$ and/or UMo_2Al_{20}. H. Noél et al. [61] studied the entire composition range in the U-Mo-Al system with forty sample compositions at 400 and 800°C for 2 months and 2 weeks, respectively, and re-wrote the ternary phase compositions, $U_6Mo_{4+x}Al_{43-X}$ and $UMo_{2-x}Al_{20+x}$, to allow for some homogeneity in the phase formation at high temperature. E. Perez et al. [62], examined different sections of the same samples used by D.D. Keiser [60], and carried out detailed characterization through TEM analysis of the different phases.

2.6 U-Mo/Al Dispersion and Monolithic Fuel Systems

U-Mo dispersion in Al and monolithic fuel systems [1] are typically plate type reactor fuel core elements designed to provide the required LEU densities. The Al cladding serves primarily as the structural component of the fuel system. Typical U-Mo/Al dispersion and monolithic type fuels, shown in Figure 4 (a,b) and (c,d) respectively, are being developed and tested, based on the results on the U-Mo/Al alloy interactions and phase stabilities under irradiation. Figure 4 shows how the U-Mo and the Al matrix interact after diffusion anneal and/or irradiation to develop significant interaction regions (mid gray) due to interdiffusion between the U-Mo particles and the Al matrix. Figure 4 (a-b) show typical optical micrographs of irradiated dispersion fuels. Figure 4 (c–d) show backscatter electron micrographs of monolithic fuel plates after thermal anneal; they additionally show significant volumetric expansion of the interaction region that takes place as the U-Mo fuel interacts with the Al.

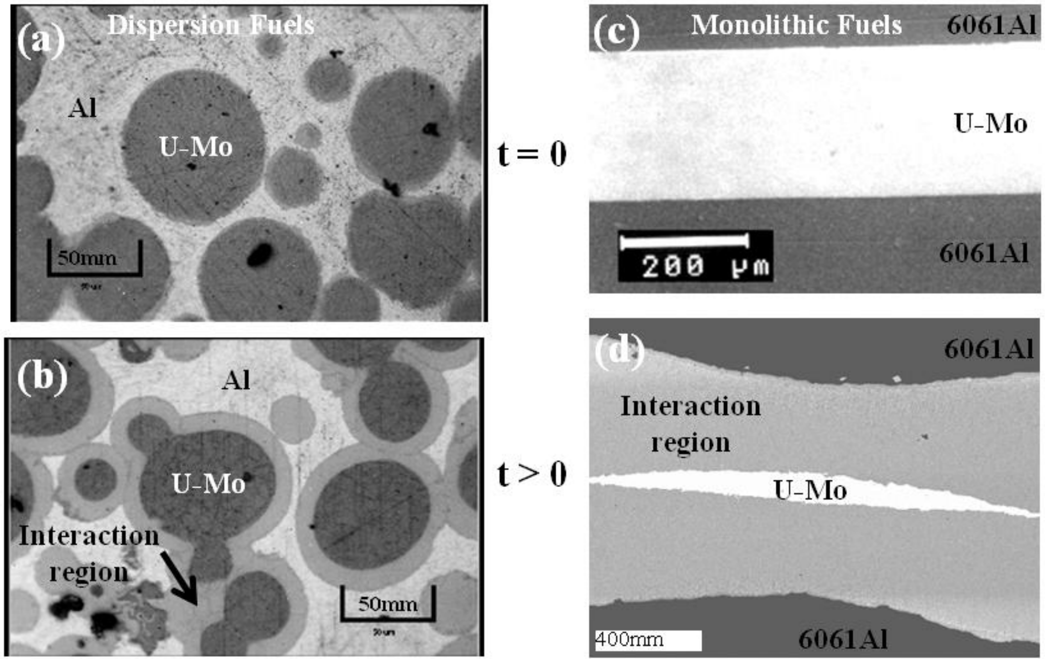

Figure 4. Typical cross sections of U-Mo dispersions in Al matrix (a) after fabrication and (b) after irradiation, and U-Mo monolithic fuel in Al matrix (c) after fabrication and (d) after diffusion anneal.

K.H. Kim et al. [33], J.-S. Lee et al. [31], B.-S. Seong et al.[48] and V.P. Sinha et al. [49] studied the preparation of dispersion particles and their phase evolution with time and temperature by thermal anneal of depleted U alloys. Their results were in good agreement with the literature, where the phase development agreed well with previous studies on U-Mo alloys, with the exception that B.-S. Seong et al. showed the development of an U_3Mo phase. This phase, however, has not been typically observed elsewhere.

U-Mo dispersions in Al have been analyzed through out-of-pile diffusion anneal experiments. J.-S. Lee et al. [50] and H.J. Ryu et al. [51, 52] reported complex interdiffusion regions that develop between the U-Mo and the Al alloys. J.-S. Lee et al. [50] reported the development of the UAl_2 and UAl_3 phases and the $\gamma \rightarrow (\alpha+\delta)$ decomposition of the U-Mo. H.J. Ryu et al. observed the UAl_3 phase based on XRD analysis. H.J. Ryu et al. also assembled diffusion couples of U-10Mo vs. Al and annealed them at 550°C for 5 and 40 hours. Based on EDS and EPMA average compositions and XRD data, they concluded that the $(U,Mo)Al_3$ and $(U,Mo)Al_4$ phases developed in the interdiffusion zones, allowing for Mo solubility in the UAl_3 and UAl_4 respectively.

2.7 U-Mo vs. Al Diffusion Couple Experiments

In this document atomic percents are typically used to describe compositions. However, in order to maintain consistency with the literature, the binary U-Mo alloys are typically described in terms of weight percents unless otherwise specified. D.D. Keiser [53] examined diffusion couples assembled through friction stir welding of U-7Mo, U-10Mo and U-12Mo vs. Al6061 alloy and reported the development of the $(U,Mo)(Al,Si)_4$ and $(U,Mo)(Al,Si)_2$ phases based on compositions. E. Perez annealed a series of diffusion couples of U-7Mo, U-10Mo and U-12Mo vs. pure Al (99.999%) at 550°C [54], and determined the $(U,Mo)Al_4$ as the average composition of the interdiffusion zone based on SEM and EPMA analysis. M.I. Mirandou et al. [55] also reported the (U,Mo)Al_3 and (U,Mo)Al_4 phase compositions, along with the $U_6Mo_4Al_{43}$ phase, and obtained very low intensity XRD peaks that suggested the UMo_2Al_{20} phase was present. H. Palancher et al. [56] and F. Mazaudier et al. [57] positively identified the $U_6Mo_4Al_{43}$ and UMo_2Al_{20} phases through micro-XRD analysis, and observed the $\gamma \rightarrow (\alpha+\delta)$ decomposition of the U-Mo, but did not find the UAl_2 phase in their studies. H. Palancher et al. annealed diffusion couples of $U_{0.85}Mo_{0.15}$ (U-6.6 wt.% Mo) vs. 1050 Al-alloy at 600°C for 4 hours and dispersions with the same $U_{0.85}Mo_{0.15}$ composition in Al-matrix at 500°C also for 4 hours. F. Mazaudier et al. annealed diffusion couples of U-5Mo, U-7Mo and U-10Mo vs. 1050A and 5754 Al-alloys from 440° to 600°C for times from 20 minutes to 10 hours, and dispersions of U-7Mo in 1050A matrix with 5754 cladding annealed under the same conditions. They observed ($\alpha+\delta$) microstructure in the U-5Mo after casting. More recently, Mi. Mirandou et al. [58] examined diffusion couples of U-7Mo vs. Al6061 in anneal-steps at 550°C for a total of 3 hours and at 340°C for a total of 3216 hours. At 550°C they observed the $U_6Mo_4Al_{43}$, UAl_3 and $U(Al,Si)_3$ phases. Differentiating UAl_3 and $U(Al,Si)_3$ from twin peaks with lower intensities in the XRD patterns, that resulted from the change in the lattice parameter. At 340°C their interdiffusion microstructure contained only the U_3Si_5 phase, suggesting different reaction mechanisms at low temperature or very slow diffusion kinetics. E. Perez et al. [59] recently reported diffusion couples of U-7Mo, U-10Mo and U-12Mo vs. pure Al (99.999%) and Al6061 at 600°C for 24 hours. Site specific characterization of the U-10Mo vs. pure Al couple by TEM showed the presence of the UAl_3, UAl_4, $U_6Mo_4Al_{43}$ and UMo_2Al_{20} and the α-U phases, but the δ-U_2Mo phase was not observed.

D.D. Keiser et. al [53], H. Palancher [56] with M.I. Mazaudier[57], and E. Perez [54,59] generated relatively thick concentration profiles where the concentration profiles developed negligible gradients, and the average concentrations of the individual components did not change through the thickness of the interdiffusion zone. H. Palancher and M.I Mazaudier also used the μ-XRD data to plot phase concentrations in the interdiffusion zones as a function of distance. They showed that the UAl_3, UAl_4, $U_6Mo_4Al_{43}$ and UMo_2Al_{20} are distributed in layered microstructures composed of two- and three phase regions. They, however, did not have the resolution to distinguish the specific grains within each region.

2.8 U-Mo vs. Al-Si Diffusion Couple Experiments

Several studies have reported that the introduction of Si into Al-alloys significantly reduces the growth rate of the interdiffusion zone and alters the phase development. Dwight [78] examined the phase equilibria on the U-Al-Si system from 400 to 950°C, and found full solubility between UAl_3 and USi_3 phases. He also reported that a miscibility gap may exist at lower temperatures (<900°C), but did not specify its transition temperature. Rhee et *al.* [79] studied the phase development in diffusion couples, U_3Si vs. Al annealed between 510° and 670°C for up to 300 hours, and reported that $U(Al,Si)_2$ and $U(Al,Si)_3$ phases developed in the interdiffusion zone. Ugajin et *al.* [80], J.W. Richardson et *al.*[81], Finlay et *al.* [82] and Kim et *al.* [83] conducted irradiation studies on the U_3Si and U_3Si_2 systems in contact with Al, and observed similar initial phase development pre-irradiation, followed by amorphization of the interdiffusion zones under irradiation. They determined that the irradiation behavior of these fuel systems was acceptable. Recently, in order to understand the benefits of Si addition, Ryu [84] measured the heats of formation in the (U,Mo)Al_3 and U(Al,Si)$_3$ and determined that Mo decreases the stability of the (U,Mo)Al_3, but Si increases the U(Al,Si)$_3$ stability. Mirandou et *al.* [85], Keiser et *al.* [86], Kim et *al.* [83] and Perez et *al.* [87] reported that the interdiffusion zone was enriched with Si, and the average composition within the interaction layer corresponded to an (U,Mo)(Al,Si)$_3$ type phase. Mirandou [85] also observed the development of the U(Al,Si)$_3$ along with UMo_2Al_{20} and U_3Si_5 phases. During irradiation, the interdiffusion zone has also shown acceptable behavior [88].

2.9 Binary UAl_3, $U_{0.9}Al_4$ and Ternary $U_6Mo_4Al_{43}$ and UMo_2Al_{20} Phases

The UAl_3, $U_{0.9}Al_4$, $U_6Mo_4Al_{43}$ and UMo_2Al_{20} phases have been studied separately to identify their properties and crystal structures. The cubic-UAl_3 [89] has the $AuCu_3$ structure, Pm-3m (221), with 4 atoms per cell. The Orthorhombic-UAl_4 [90,91,92], Imma (74), has 20 atoms per unit cell. The cubic-UMo_2Al_{20} [93], Fd-3M (227) has 184 atoms per cell. The hexagonal-$U_6Mo_4Al_{43}$ [94], P63/mcm, has 106 atoms per unit cell. The UAl_3 phases contain a relatively simple crystal structure. B.S. Borie Jr. [91] and V.Y. Zenou et al. [92] considered the $U_{0.9}Al_4$. V.Y. Zenou showed that the $U_{0.9}Al_4$ phase deviations from the expected UAl_4 stoichiometry are a result of vacancies at the U-sites in the crystal lattice resulting in a 92% U-site occupation in the phase.

The ternary UMo_2Al_{20} [93] and $U_6Mo_4Al_{43}$ [94] phase crystal structures are composed of complex sub structures that form the crystal lattice. S. Nieman et. al [95,97,98] synthesized the phases and determined that the crystal lattice sites are occupied by coordination polyhedra that occupy the lattice positions in the crystal. The cubic-UMo_2Al_{20} has the $Cr_2Mg_3Al_{18}$ [93] and

$CeCr_2Al_{20}$ [98] type structures. The work by H. Noél et al. [61] showed that the Mo and Al have homogeneity ranges, $U_6Mo_{4+x}Al_{43-x}$ and $UMo_{2-x}Al_{20+x}$, in the phases that expand with higher temperatures.

General agreement between the phases that develop in the interdiffusion zone between U-Mo and Al exist between 400 and 600°C. The UAl_3, $U_{0.9}Al_4$, $U_6Mo_4Al_{43}$ and UMo_2Al_{20} phases have been observed in layered microstructures in the interdiffusion zones, but until this document, no one has reported grain specific analysis of the phases in the interdiffusion zones. This study carried out an analysis of single grains through TEM of the different phase regions observed in a U-10Mo vs. Al (99.999%) diffusion couple annealed at 600°C for 24 hours. Most of the works mentioned above used Al-alloys to carry out their analysis. Unfortunately, trace element additions can significantly affect the phase development of the interdiffusion zone. This study used high purity alloys and controlled environments to avoid the development of unexpected phases. The microstructural development and crystallographic analysis by TEM is used to explain the phase development in the interdiffusion zone, and the analysis is discussed with respect to the behavior of the fuel systems during irradiation conditions.

2.10 Stress development as a result of phase transformations.

The interdiffusion zones with diffusion couple experiments showed that the interdiffusion zone divided into layered microstructures, where each layer evolved according to the local composition of the interdiffusion zone. The phase distributions were explained by the diffusion path from the concentration profiles plotted in the ternary U-Mo-Al phase diagram. Three-phase regions developed within the interdiffusion zones, indicating that additional factors needed to be considered in order to explain the observed microstructures. The microstructures of the observed three-phase regions developed periodic banding as a sub-layer within the interdiffusion zone.

The development of periodic bands in the interaction layers has been observed in the interdiffusion zones of some alloy systems. V.A. Van Rooijen et al. [99] observed them in oxidized alloys. K. Osinski et al. [100] observed periodic pattern formation in Fe-Si vs. Zn diffusion couples. The group of M.R. Rijnders et al. [101,102] and A.A. Kodenstov [103] et al. observed similar results in Fe_3Si, Co_2Si and Ni_3Si_2 vs. Zn, in $Ni_{50}Co_{20}Fe_{30}$ vs. Mg, and in SiC vs. Pt diffusion couples. X. Su [104] also considered the Ni_3Si_2 vs. Zn and reached similar conclusions as M.R. Rijnders and A.A. Kodenstov. In their systems, the development of secondary phases at the interface resulted in periodic bands. A qualitative description of the model by C.Wagner [105] provided an acceptable and more likely partial explanation for the periodic layer development in the U-Mo vs. Al system.

Based on the results of the above studies, development of periodic banding requires that internal stresses develop within the interdiffusion zones in diffusion couples. In this study the presence of periodic banding within the interdiffusion zones of the diffusion couples was used as evidence that internal stresses were present within the interdiffusion zones. Stress was then used to explain the observed microstructural and phase development of the interdiffusion zones.

3. EXPERIMENTAL DETAILS

3.1 Laboratory Facility

To prevent oxidation of the U-Mo alloys, and contamination of the laboratory facility, the alloys were continuously handled and stored under an Ar atmosphere. To accomplish this, the alloys remained in the glove box shown in Figure 5. The glove box was setup to maintain an inert atmosphere by feeding Argon through an inlet on the rear bottom of the box as shown in the schematic in Figure 6. Argon then exited the box through an outlet that was positioned at the center top of the box. The gas flowed towards a chemical fume-hood. Prior to exiting, Ar passed through a flask filled with oil. This set-up prevented back flow of air into the glove box and trapped any airborne particulate. To further ensure trapping of airborne particulate, an air filter was also placed prior to the gas outlet. When the alloys are handled in the glove box, the chemical fume-hood remained engaged. This entire set-up was placed in an isolated laboratory with limited access.

All U-alloy preparation and diffusion couple assembly were carried out in the glove box in an inert atmosphere to prevent, or minimize the oxidation of the alloys. The alloys that underwent homogenization anneal and all the diffusion couples in this study were placed in the quartz capsules shown in Figure 7. Figure 8 shows a schematic of a diffusion couple assembly inserted into the quartz capsule. The capsules were flushed with H_2 gas several times and sealed under Ar atmosphere using the vacuum system shown in Figure 9. Finally, the alloys or couples were treated in the Lindberg/Blue™ three-zone tube furnace shown in Figure 10.

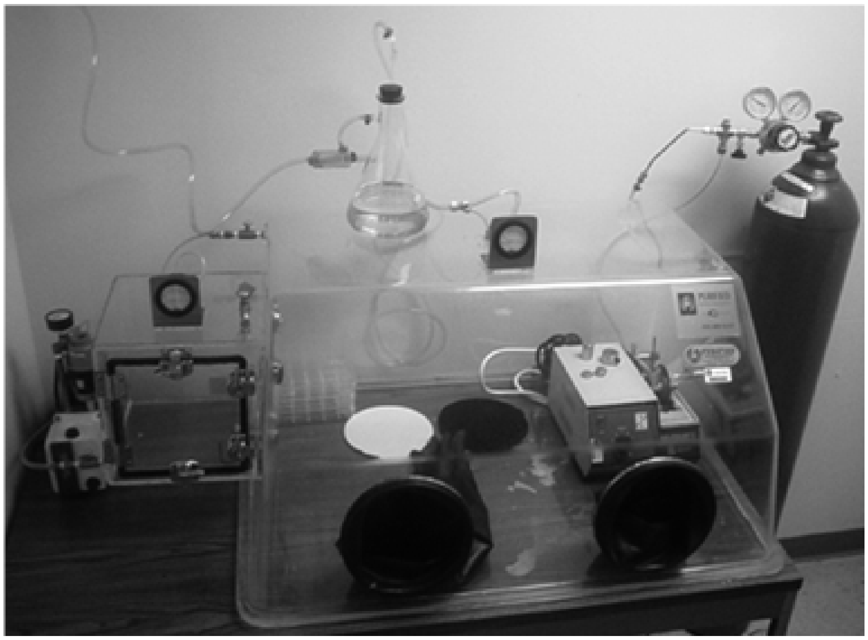

Figure 5. Glove box setup for the handling and storage of materials under a controlled Argon atmosphere.

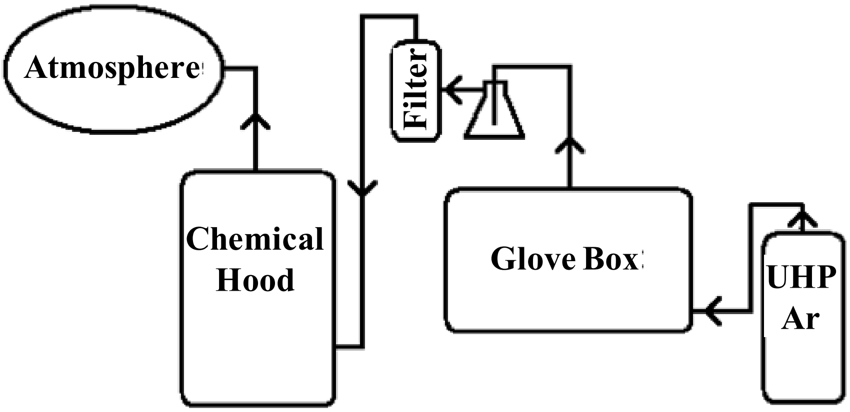

Figure 6. A schematic diagram showing the Ar flow through the glove box.

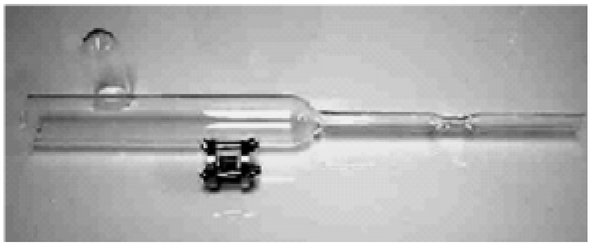

Figure 7. Quartz capsule for heat treatment of diffusion couples, and a diffusion couple jig assembly holding a diffusion couple before diffusion anneal.

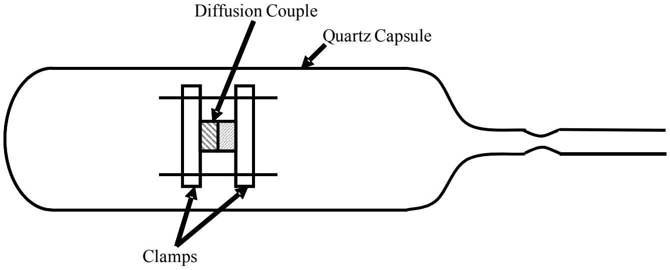

Figure 8. A schematic of a diffusion couple inserted in a quartz capsule in preparation for the vacuum flush procedure.

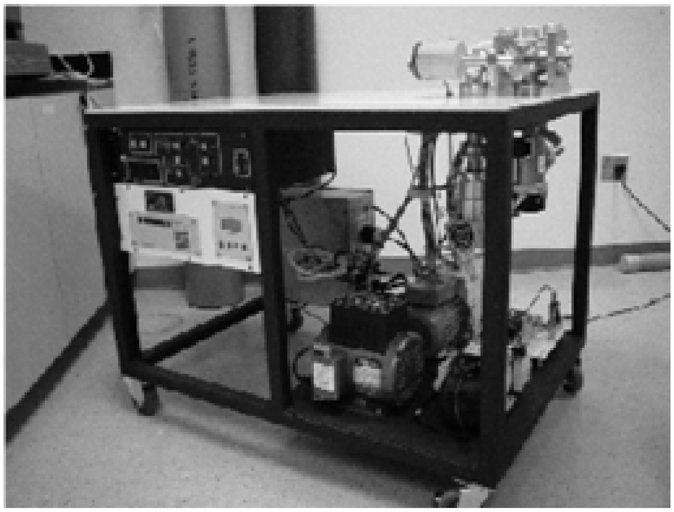

Figure 9. Custom fabricated high vacuum system for evacuating quartz capsule.

Figure 10. Lindberg/Blue™ three-zone tube furnace used for the heat treatment of alloys and diffusion couples.

3.2 U-Mo, Al and Al-Si alloy preparation

Depleted uranium (DU) alloys consisting of solid solution γ-phase with U-7 wt.% Mo, U-10 wt.% Mo and U-12 wt.% Mo were used for the experiments. The alloys were cast using high-purity DU and Mo via arc melting at Idaho National Laboratory (INL), Idaho Falls, ID. They were melted three times to ensure the homogeneity and then drop-cast to form rods with 6.35 mm diameter. The as-cast rods were then homogenized in quartz capsules under an Ar atmosphere at 950°C for 96 hours. All U-Mo alloys were water-quenched after homogenization to retain the high temperature γ-phase. The homogeneity in composition, phase constituents and microstructure of the alloys were examined by x-ray diffraction (XRD, Rigaku^{TM} DMAX-B), and scanning electron microscopy (SEM, Hitach^{TM} 3500N) equipped with X-ray energy dispersive spectroscopy (XEDS). The pure Al (99.999 wt.%) alloy was obtained from a commercial source (Alpha-Aesar^{TM}). The Al-Si alloys were prepared with high purity Al (99.999 wt.%) and Si (99.9999 wt.%) by triple arc melting at Ames National Laboratory, Ames, Iowa.

Both U-Mo and Al alloy rods were sectioned into disks 6.35 mm in diameter and 3 mm in thickness. Faces of the U-Mo and pure Al disks were metallographically polished using a final step of 1μm diamond paste to obtain a near mirror surface. Immediately prior to assembly of diffusion couples, the pure Al and Al-Si discs were further cleaned with concentrated HNO_3 to dissolve remaining traces of Al_2O_3.

3.3 Diffusion couple assembly and characterization

After preparation of the alloys for experiments, the prepared surfaces were placed in contact with each other and held together by two clamping disks with stainless steel rods to form a jig as shown in Figure 7. The jig assembly was then encapsulated, as schematically shown in Figure 8, in a quartz capsule and sealed under an Ar atmosphere after repeated vacuum (10^{-6} torr) and H_2 purge. Ta foil was placed inside the capsules prior to sealing to serve as an oxygen trap. All couples were annealed using a Lindberg/Blue™ three-zone tube furnace. The diffusion couples, U-7Mo, U-10Mo and U-12Mo vs. Al, were annealed at 600°C to avoid decomposition of the γ-U phase to obtain relatively thick layers of interaction. Diffusion couples of U-7Mo, U-10Mo and U-12Mo vs. Al, Al-2 wt.% Si and Al-5 wt.% Si were annealed at 550°C to allow some of the U-Mo alloys in the couple assemblies to undergo the $\gamma\text{-U}\rightarrow\alpha\text{-U}+\delta\text{-U}_2\text{Mo}$ decomposition. After anneal the diffusion couples were quenched by breaking the quartz capsule in cold water. Each diffusion couple was then mounted in epoxy for microstructural examination and was cross-sectioned and polished to a near mirror polish by using a 1μm diamond paste for the final step.

For each diffusion couple, SEM was carried out to examine the quality of diffusion bonding and the thickness of the interaction layer. Selected regions within the interdiffusion zone were examined using backscatter electron microscopy to document the presence of fine-scale (in the order of 100 nm grain size) microstructure. Concentration profiles were determined by EPMA (JEOL 733 Superprobe^{TM}) using stoichiometric UO_2, pure Mo and pure Al standards provided by the EPMA manufacturer. A point-to-point counting technique ($\Delta x = 5\mu m$) was employed for the measurement and the ZAF correction was used for the determination of the concentrations for individual components. Since EPMA measurement has a resolution of several micrometers and the microstructure of the interdiffusion zone was extremely fine, the measured composition represented an average concentration.

Selected regions within the interdiffusion zone of the diffusion couple U-10Mo vs. Al were examined by TEM and scanning TEM (STEM). The TEM specimens were prepared by using a Focused Ion Beam (FIB) in-situ lift-out (INLO) technique. A FEI/Tecnai™ F30 300keV TEM equipped with a Fischione^{TM} high angle annular dark field (HAADF) detector and X-ray energy dispersive spectroscopy (XEDS) was employed. Selected Area Electron Diffraction (SAED) and convergent beam electron diffraction (CBED) coupled with XEDS for various fine-scaled phases were collected and examined. Indexing of diffraction patterns was performed using the Digital Micrograph™, Microsoft Excel™ and Adobe Illustrator™ software packages.

3.4 Characterization of 85.7Al-11.44U-2.86Mo, 87.5Al-10U-2.5Mo, 56.1Al-18.9Si-21.9U-3.1Mo and 69.3Al-11.9Si-18.8U (at.%) Cast Alloys

Alloys with nominal compositions 85.7Al-11.44U-2.86Mo, 87.5Al-10U-2.5Mo, 56.1Al-18.9Si-21.9U-3.1Mo and 69.3Al-11.9Si-18.8U in at.% were cast by arc melting of high purity Al, U and Mo. The alloys were re-melted three times to ensure complete melting of the original materials in order to minimize macro-scale segregation. The alloys were then annealed at 500°C for 200 hours in an Ar atmosphere. For the 85.7Al-11.44U-2.86Mo, 87.5Al-10U-2.5Mo alloys, one specimen, roughly 3mm by 3mm by 3mm, was removed from each casting for this study [60]. -½in. by ½in. by ½in. samples were obtained from each of the 56.1Al-18.9Si-21.9U-3.1Mo and 69.3Al-11.9Si-18.8U alloys. X-ray diffraction (XRD) patterns were collected for these alloys using a Rigaku^{TM} D-MaxB diffractometer operating with Cu-K$_\alpha$ radiation at 40 kV and 30 mA with a 1° divergence slit. For microstructural analysis, the specimens were then mounted in epoxy, sectioned and metallographically polished down to 1μm using diamond paste. The microstructures of these alloys were then examined using a Hitachi^{TM} S3500N scanning electron microscope (SEM) and a JEOL^{TM} 6400F field-emission SEM. Backscatter electron (BSE) micrographs and standardless semi-quantitative X-ray energy dispersive spectroscopy (XEDS), using the ZAF correction, were employed for microstructural and compositional analysis. Errors in accuracy are typically expected in the XEDS measurements due to the assumptions made in the quantitative standardless analysis. The instrument's precision was not affected; thus the XEDS was reliably used for determination of solid solubility in the observed phases. In this study, errors of up to 3 at% from the expected phase compositions were observed in the XEDS results.

In this study, the 85.7Al-11.44U-2.86Mo, 87.5Al-10U-2.5Mo alloys were analyzed by TEM. Specimens for TEM were prepared with a focus ion beam (FIB) in-situ lift-out (INLO) technique using a FEI^{TM} 200TEM. The specimens were selected from specific regions in the alloys to capture the phases observed by SEM. The samples were thinned to 100nm in order to obtain electron transparency during TEM analysis. A FEI/Tecnai^{TM} F30 300keV TEM/STEM, equipped with a Fischione^{TM} HAADF detector and XEDS, was used for analysis of phase constituents and microstructure. Bright field and high angle annular dark field (HAADF) imaging, along with selected area electron diffraction (SAED), were used to carry out the analysis.

4. RESULTS

4.1 Cast 85.7Al-11.44U-2.86Mo and 87.5Al-10U-2.5Mo Alloys characterization [62]

Figure 11 and Figure 12 present typical backscatter electron micrographs obtained from the 85.7Al-11.44U-2.86Mo and 87.5Al-10U-2.5Mo cast alloys. In total, five different phases were observed. This indicates that complete phase equilibrium was not achieved despite the homogenization at 500°C for 200 hours. Four of the phases, identified as regions A through D, were distributed in both alloys as shown in Figure 11 and Figure 12. The fifth phase, identified as region E in Figure 13, was observed only in the 85.7Al-11.44U-2.86Mo alloy in extremely small quantities. Approximate compositional analysis for these phases (i.e., regions A through E) was conducted by XEDS on the SEM. Table 1 reports the average composition of regions A through D; each composition was determined from a minimum of five measurements per region. Only two measurements were carried out for the small residual phase, (i.e., region E) shown in Figure 13, due to its size and quantity. The standard deviations for the measured phase compositions, also reported in Table 1, demonstrated little variation in the compositions of the observed phases. The UAl_3 and UAl_4 phases exhibited little or no solubility for Mo.

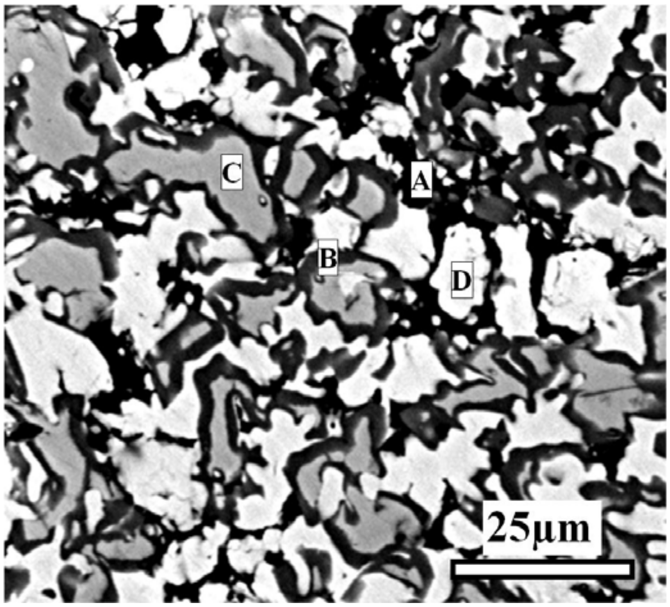

Figure 11. Backscatter micrograph showing the typical microstructure of the 85.7Al-11.44U-2.86Mo alloy. Four different phases are visible based on image contrast.

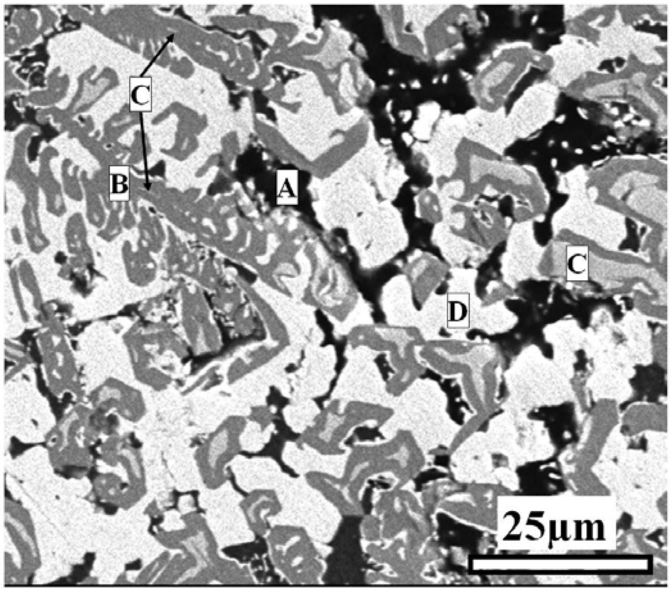

Figure 12. Backscatter micrograph showing the typical microstructure of the 87.5Al-10U-2.5Mo alloy. Four different phases are visible based on image contrast.

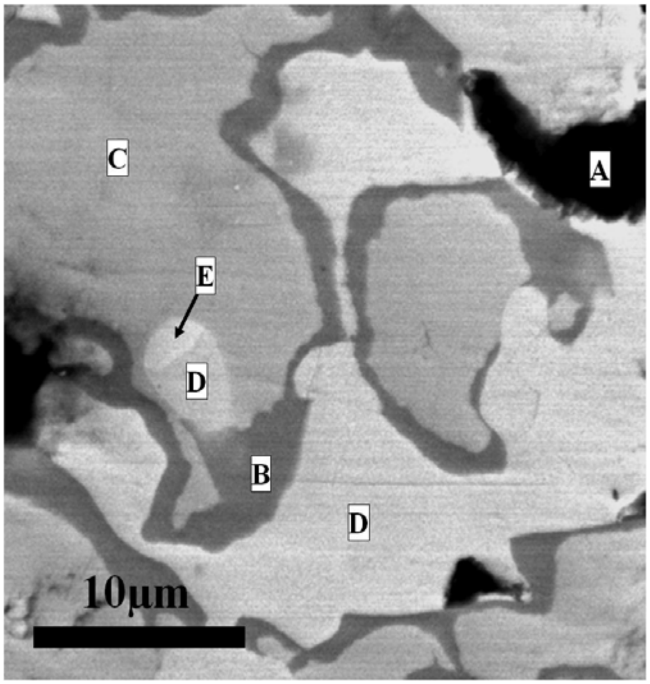

Figure 13. Backscatter micrograph of the 85.7Al-11.44U-2.86Mo alloy showing an additional small region containing the (E) UAl_3 phase observed in this alloy.

Table 1. Microstructural and compositional characteristics of the phases observed in the 85.7Al–11.44U–2.86Mo and 87.5Al–10U–2.5Mo alloys.

Alloy	Region	Contrast Color	Phase	Composition (at.%)		
				U	Mo	Al
85.7Al-11.44U-2.86Mo	A	Black	Al	2.1±1.1	0.6±0.5	97.4±1.4
	B	Dark Gray	UMo_2Al_{20}	5.2±0.5	5.7±0.6	89.1±0.3
	C	Light Gray	$U_6Mo_4Al_{43}$	12.2±3.1	6.4±3.2	81.3±0.6
	D	White	UAl_4	18.0±0.4	0.7±0.4	81.3±0.4
	E	Residual	UAl_3	22.3±0.4	0.7±0.1	77.0±0.5
87.5Al-10U-2.5Mo	A	Black	Al	0.9±0.4	0.2±0.1	98.9±0.3
	B	Dark Gray	UMo_2Al_{20}	4.8±0.8	5.6±0.9	89.5±0.4
	C	Light Gray	$U_6Mo_4Al_{43}$	10.5±0.3	8.0±0.6	81.6±0.8
	D	White	UAl_4	18.2±0.3	0.3±0.1	81.5±0.3

Alloy specimens were prepared for TEM/STEM analysis via FIB-INLO for detailed examination of phase constituents. Figure 14(a) shows a HAADF STEM micrograph of 85.7Al-11.44U-2.86Mo alloy. Based on electron diffraction patterns shown in Figure 14(b-d), and composition reported in Table 1, the three phases presented in Figure 14(a) were identified as orthorhombic-UAl_4, hexagonal-$U_6Mo_4Al_{43}$ and diamond-cubic-UMo_2Al_{20}. Despite the significant presence of overlapping peaks, XRD pattern from these alloys further suggested the presence of these phases as shown in Figure 15 for the 85.7Al-11.44U-2.86Mo alloy. The Al solid solution was not included in the TEM specimen for this alloy; nevertheless, SEM/EDS and XRD analysis both confirmed the presence of fcc-Al solid solution.

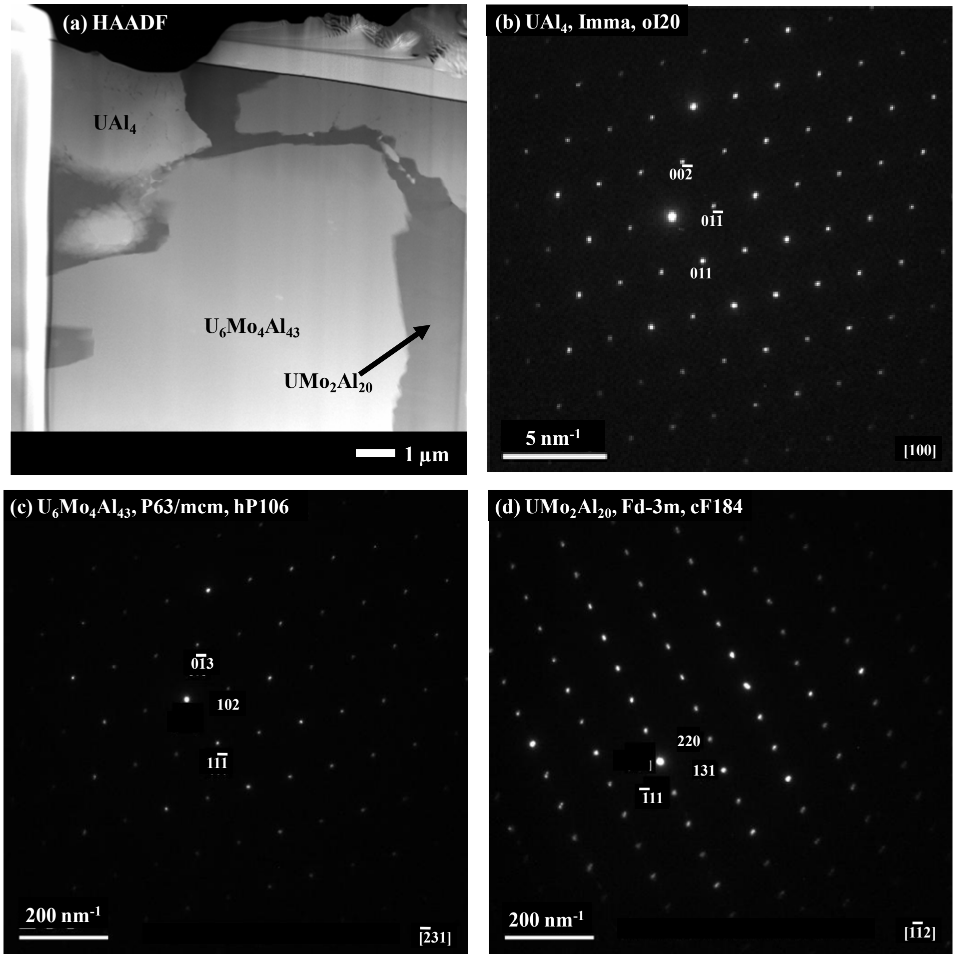

Figure 14. (a) High angle annular dark field (HAADF) TEM image of the 85.7Al-11.44U-2.86Mo alloy and (b–d) electron diffraction patterns for the same alloy.

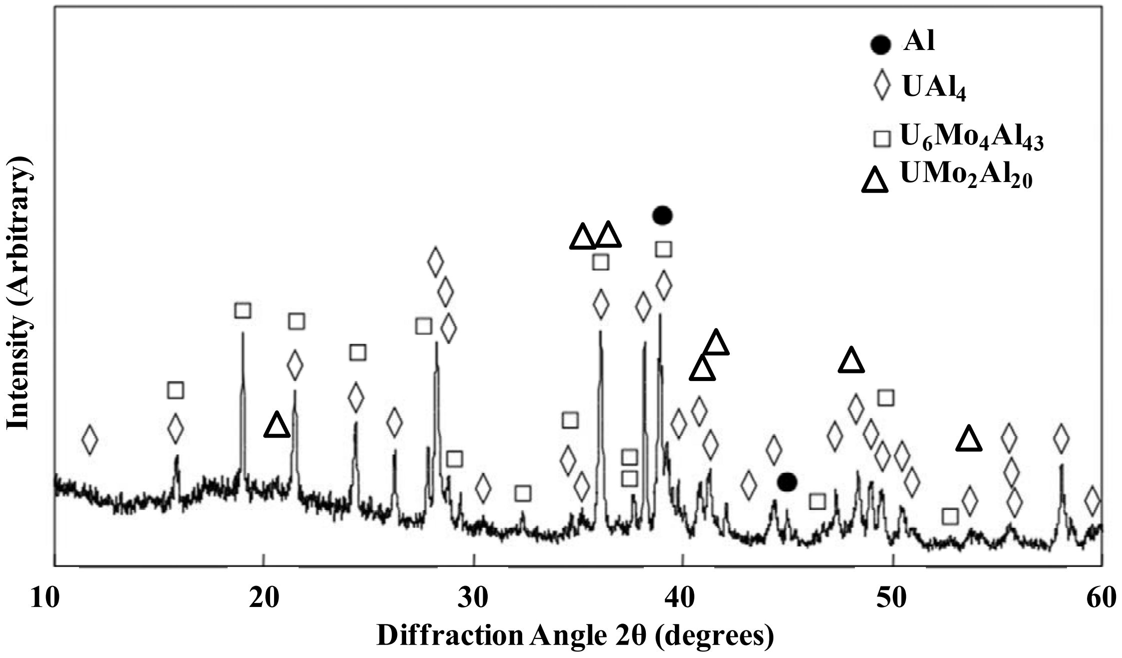

Figure 15. X-ray diffraction patterns of 85.7Al-11.44U-2.86Mo.

Figure 16(a) shows a HAADF STEM micrograph of the 85.7Al-11.44U-2.86Mo alloy specimen that was specifically prepared by FIB-INLO to contain the small phase (i.e., region E in Figure 13 and in Table I). Based on electron diffraction, summarized in Figure 16(b), this phase was identified as the cubic-UAl_3 phase found in the binary U-Al system. The composition of this phase, as measured by XEDS and shown in Table 1, agreed well with the binary UAl_3 phase with little solubility for Mo.

Figure 17 shows a HAADF STEM micrograph from the 87.5Al-10U-2.5Mo alloy specimen that contains fcc-Al, orthorhombic-UAl_4, and hexagonal-$U_6Mo_4Al_{43}$. These phase constituents were similar to those observed in 85.7Al-11.44U-2.86Mo alloy. The XRD pattern shown in Figure 18 for the 87.5Al-10U-2.5Mo also suggested the presence of these major phase constituents, and showed the presence of diamond cubic-UMo_2Al_{20} phase that was not presented in Figure 15 for the 85.7Al-11.44U-2.86Mo alloy. The relative peak intensities of the $U_6Mo_4Al_{43}$ phase in the 87.5Al-10U-2.5Mo alloy were significantly lower than those of the UAl_4 phase. As a result, some peaks may not be apparent in the collected pattern for the 87.5Al-10U-2.5Mo alloy and may be more prevalent in the 85.7Al-11.44U-2.86Mo alloy.

Comparison of Figure 11 and Figure 12 showed morphological differences in the microstructures of the alloys. The 87.5Al-10U-2.5Mo alloy contained a larger volume fraction of Al solid-solution and UMo_2Al_{20}, and lacked the UAl_3 phase. The volume fractions of the different phases varied between the two alloys. Nonetheless, the observed phases were found to be similar in the two alloys.

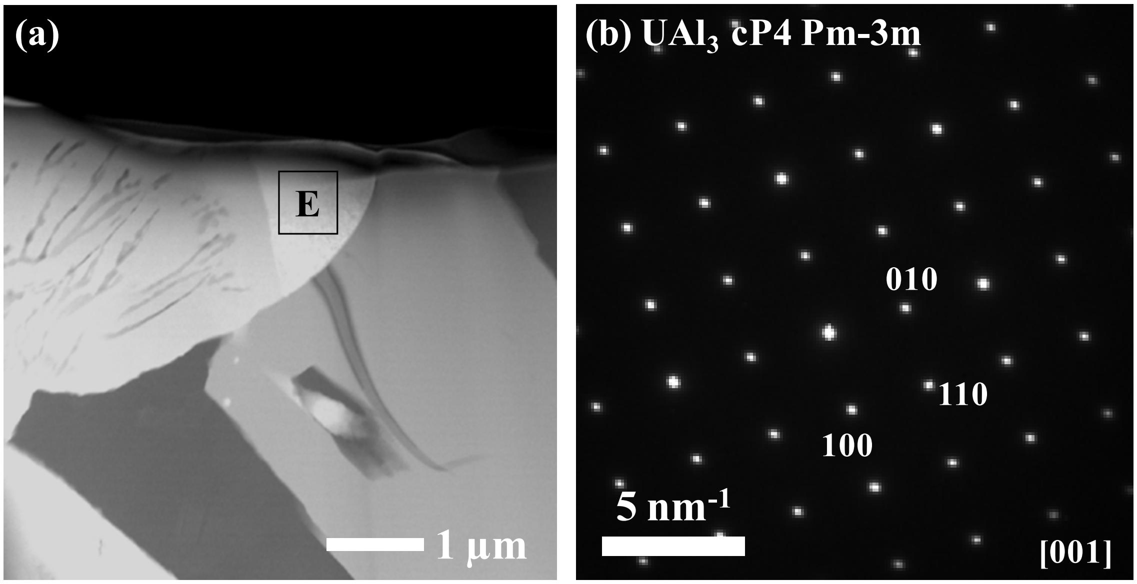

Figure 16. (a) High angle annular dark field (HAADF) TEM image of the 85.7Al-11.44U-2.86Mo alloy, and (b) selected electron diffraction patterns for the same alloy.

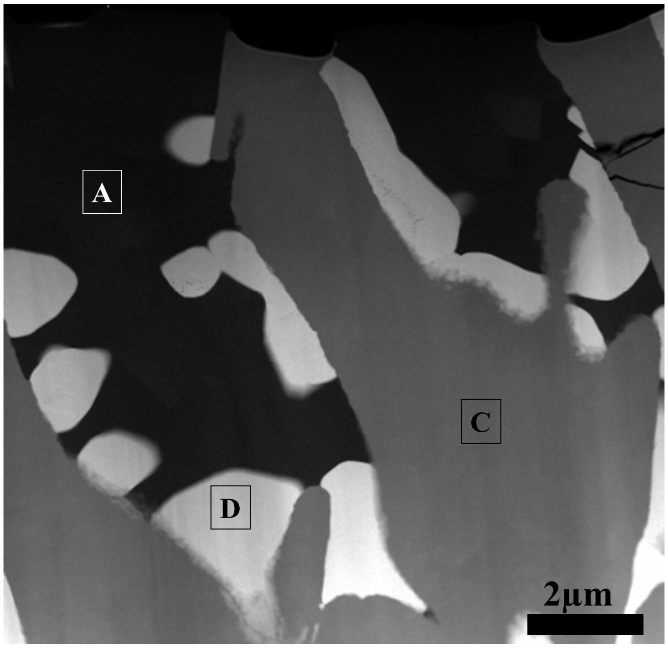

Figure 17. High angle annular dark field (HAADF) TEM image of the 87.5Al-10U-2.5Mo alloy.

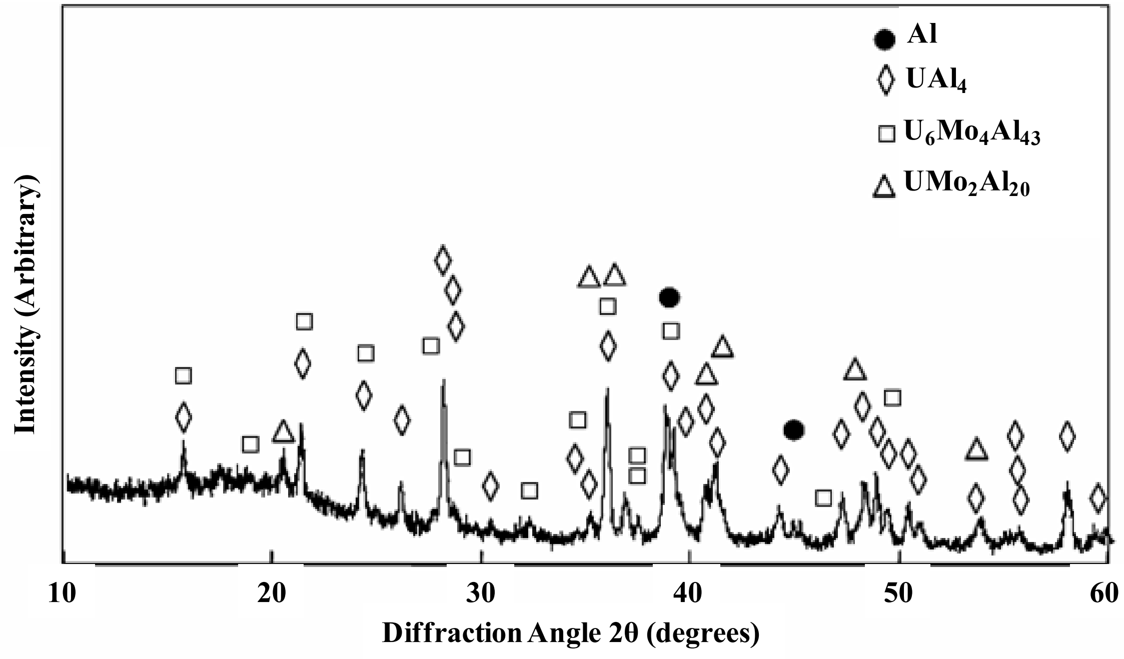

Figure 18. X-ray diffraction patterns of 87.5Al-10U-2.5Mo alloy.

4.2. Phase Constituents in 19U-69Al-12Si and 22U-3Mo-56Al-19Si (at.%) Cast Alloys

Alloys with nominal compositions 19U-69Al-12Si at.% and 22U-3Mo-56Al-19Si at.% were cast for this study. The alloys' bulk compositions were measured by SEM-XEDS standardless compositional analysis; Table 2 shows the bulk composition of the alloys obtained by one large area XEDS measurement for each alloy. The compositions were chosen to approximate those typically observed in the inter diffusion zones of U-Mo vs. Al-Si diffusion couple experiments. They were also chosen to examine the effect of Si in the U-Al system, and then to examine the effect of Mo into the U-Mo-Al system. Figure 19 (a, b) and Figure 20 (a, b) present backscatter electron micrographs for the 19U-69Al-12Si and 22U-3Mo-56Al-19Si after anneal at 500°C for 200 hours. The general microstructures show a dominant light gray phase, based on image contrast, and dark phases along the interdentritic regions.

Table 2. Bulk compositions of the 19U-69Al-12Si and 22U-3Mo-56Al-19 alloys as measured by standardless XEDS.

Alloy	U	Mo	Al	Si
	(at%)			
19U-69Al-12Si	17.4	0	76.0	6.3
22U-3Mo-56Al-19Si	18.8	2.6	61.4	17.2

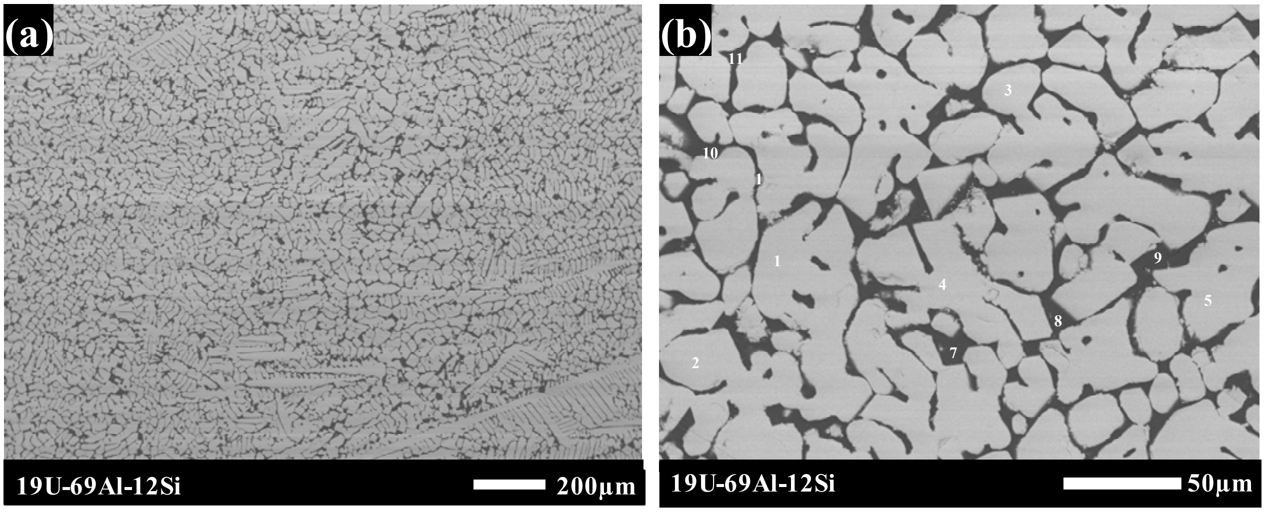

Figure 19. Backscatter electron micrograph of the 19U-69Al-12Si alloy showing a multiphase microstructure (a) low magnification, (b) detailed micrograph showing two-phase contrast for the bulk of the alloy.

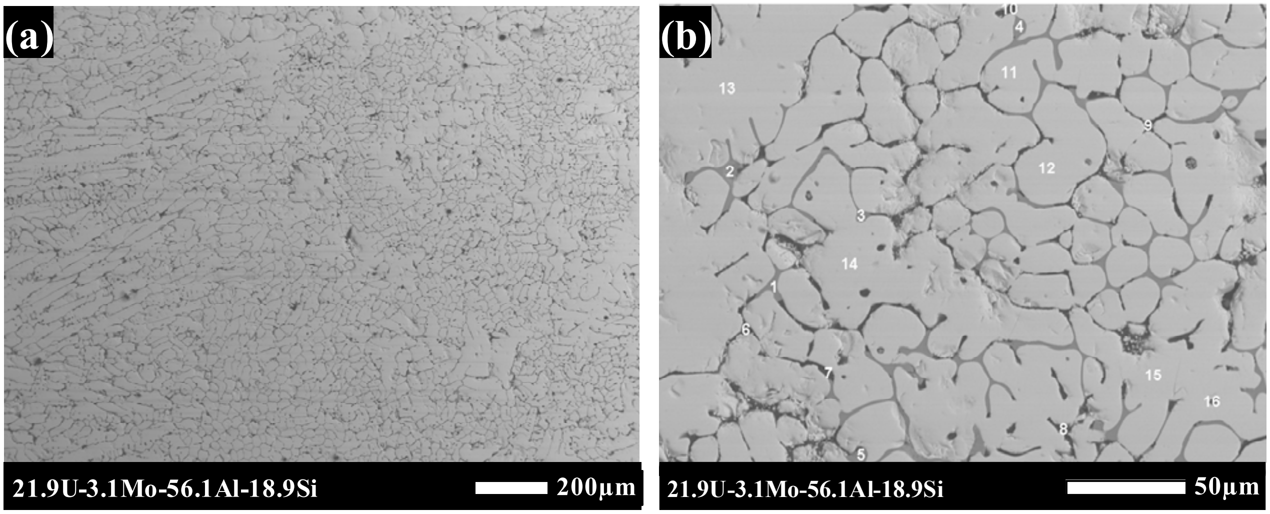

Figure 20. Backscatter electron micrograph of the 21.9U-3.1Mo-56.1Al-18.9Si alloy showing a multiphase microstructure (a) low magnification, (b) detailed micrograph showing three-phase contrast.

The 19U-69Al-12Si alloy, shown in Figure 19, based on image contrast and XEDS analysis, developed a two phase microstructure with the $U(Al,Si)_3$ grain composition and Al solid solution at the grain boundaries. A third phase, shown in Figure 21, was detected in very small concentrations. The XEDS data for this phase was not reliable due to the small size of the particle, but image contrast identified the different phase. The 22U-3Mo-56Al-19Si alloy showed three different phase compositions with a dominant phase composition of (U,Mo)(Al,Si)$_3$. Two other phases, detailed in Figure 20 (b), were restricted to the interdendritic regions, and had compositions that matched the Al solid solution and the UMo$_2$Al$_{20}$ phase. Table 3 summarizes the measured compositions for each phase. The numbers in Figure 19 (b) and Figure 20(b) represent the precise location where data was collected on each phase.

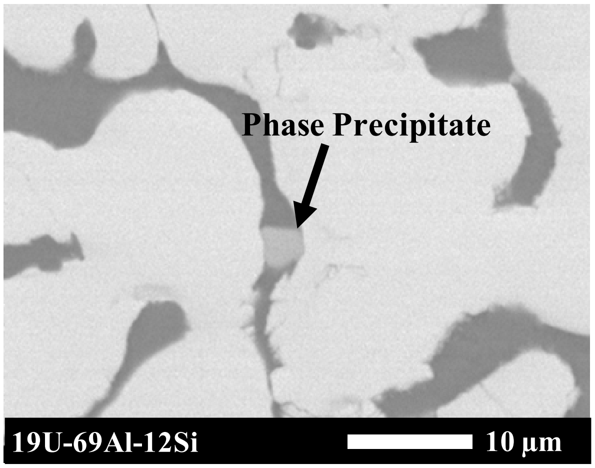

Figure 21. Detailed backscatter electron micrograph showing the small precipitate found in the 19U-69Al-12Si alloy.

Table 3. Compositions of the individual phases found in the alloys as measured by XEDS.

Alloy	Phase	U	Mo	Al	Si	Possible Phase
		(at%)				
19U-69Al-12Si	Black	0.2 ± 0.1	0.2 ± 0.1	99.6 ± 0.1	0.1 ± 0.3	Al Solid Sol.
	Light Gray	24.9±0.1	0.5±0.1	61.9±0.6	12.7±0.4	U(Al,Si)$_3$
	Residual	8.1	0.5	91.4	0.0	-
22U-3Mo-56Al-19Si	Black	0.5±0.1	0.1±0.1	98.9±0.3	0.5±0.2	Al Solid Sol.
	Light Gray	22.7 ± 0.4	3.0 ± 0.7	52.7 ± 0.5	21.6 ± 0.5	(U,Mo)(Al,Si)$_3$
	Dark Gray	4.4 ± 0.2	8.3 ± 0.2	87.2 ± 0.4	0.1 ± 0.3	UMo$_2$Al$_{20}$

Crystallographic analysis of the alloys was performed by x-ray diffraction (XRD). XRD patterns were collected from each sample and are shown in Figure 22(a) and (b). The UAl_3 phase was observed in both samples as the dominant phase based on peak relative intensities. The Al solid solution was discerned in both alloys. The UMo_2Al_{20} phase was discerned only in the 22U-3Mo-56Al-19Si sample as shown in Figure 23. The phase shown in Figure 21 remained within the XRD equipment background noise. XEDS showed distinct $U(Al,Si)_3$, $(U,Mo)(Al,Si)_3$ and UMo_2Al_{20} phase compositions in the in the 19U-69Al-12Si and 22U-3Mo-56Al-19Si alloys respectively indicating that the UAl_3 phase must have Si and Mo solid solubility.

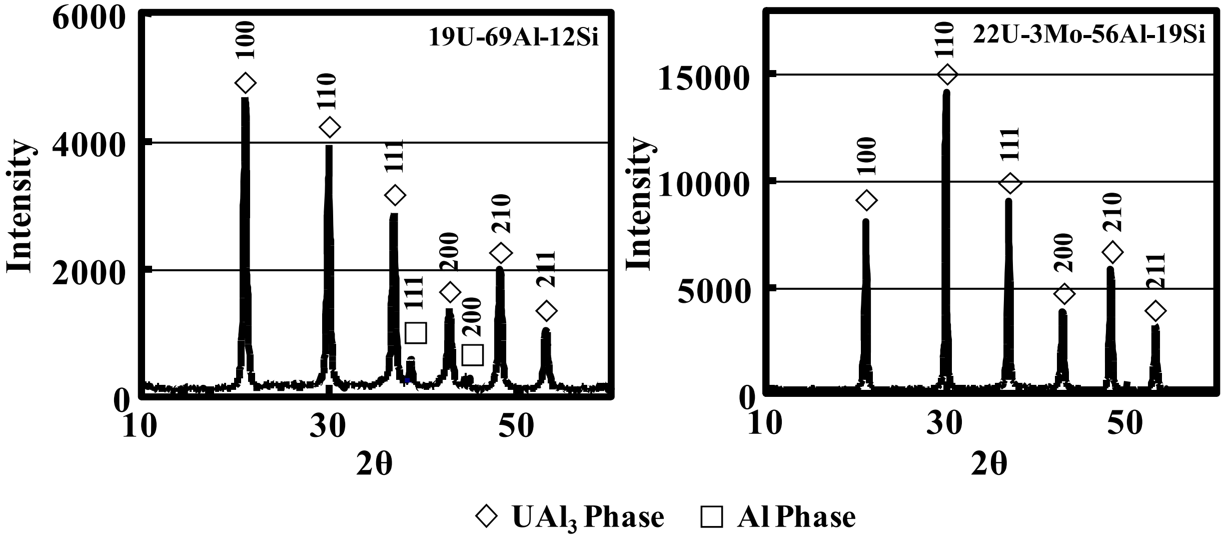

Figure 22. X-ray diffraction pattern from alloys with nominal compositions (a) 19U-69Al-12Si and (b) 22U-3Mo-56Al-19Si.

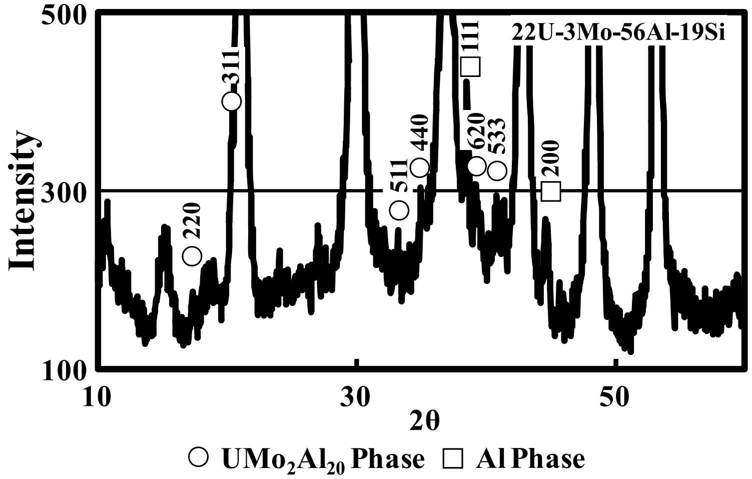

Figure 23. Selected region of the X-ray diffraction pattern from the 22U-3Mo-56Al-19Si alloy with nominal compositions detailing the UMo_2Al_{20} phase.

In order to confirm solid solubility of Si and Mo in the UAl_3 phase, the lattice parameters of the observed UAl_3-phases were measured for each alloy, and are reported in Table 4. The covalent atomic radii of U, Mo, Al and Si are 196 pm, 154 pm, 121 pm and 111pm. The published value of the UAl_3 phase is 0.4263 nm [89]. Based on atomic radii and Si substitution of Al, the UAl_3 phase should experience a decrease in lattice parameter with increasing Si and/or Mo concentrations. The data in Table 4 confirmed the expected decreases in lattice constant.

Table 4. Lattice parameters of UAl_3 type phase in 19U-69Al-12Si and 22U-3Mo-56Al-19Si alloys.

Alloy	Lattice Parameter a_o of UAl_3 (nm)
19U-69Al-12Si	0.4231
22U-3Mo-56Al-19Si	0.4218

4.3 Diffusion Couples: U-Mo vs. Pure Al Annealed at 600°C for 24 Hours

Figure 24 shows backscatter electron micrographs of the diffusion couples, (a) U-7 wt.% Mo, (b) U-10 wt.% Mo and (c) U-12 wt.% Mo vs. pure Al (99.999%), annealed at 600°C for 24 hours. In these micrographs, Al appears black on top, the U-Mo alloy appears light gray on the bottom, and the interdiffusion zone appears dark gray in the middle. These micrographs clearly demonstrate that the interdiffusion zone thicknesses were consistent through the width of the diffusion couples, except at the very-edges. This indicates that diffusion bonding in these diffusion couples was consistent. The interdiffusion zones are restricted to the dark gray regions observed in these micrographs. Interdiffusion of Al into the bcc U-Mo alloys (e.g., solid-solution of Al in U-Mo alloys) and of U or Mo into the fcc Al (e.g., solid-solution of U or Mo in Al) were not observed. Thus, the interaction region in the diffusion couples can be sharply defined by the Al/interdiffusion zone interface and U-Mo/interdiffusion zone interface.

Table 5 reports the measured thickness and growth constants of the interdiffusion zones, and based on the assumption of an entirely diffusion controlled system, where the interaction layer thickness, T, defines the growth constant, K, by $T = K*t^{1/2}$, where *t* is the diffusion anneal time. The interdiffusion zone thickness showed a dependence on the Mo concentration where the diffusion couples with U-10Mo showed the largest growth rate.

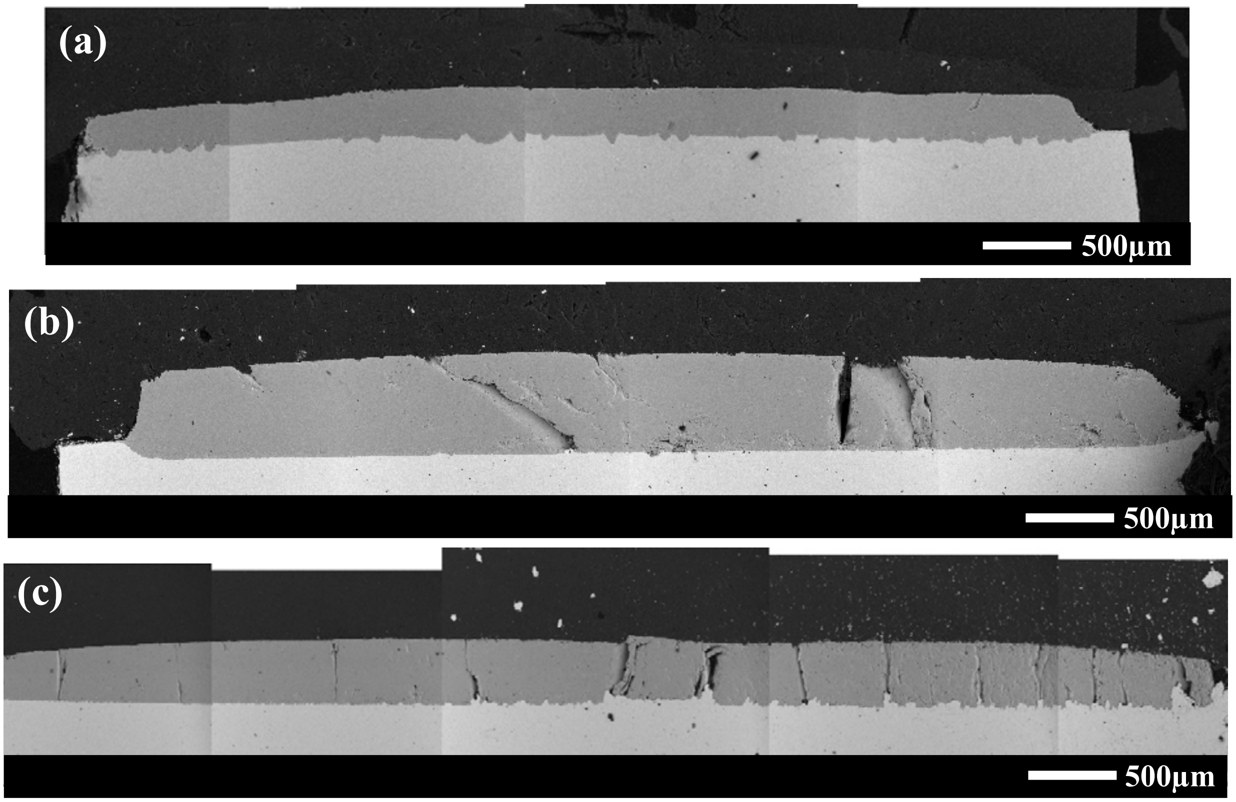

Figure 24. Backscatter electron micrographs of the diffusion couples: (a) U-7Mo vs. Al, (b) U-10Mo vs. Al and (c) U-12Mo vs. Al annealed at 600°C for 24 hours.

Table 5. Thickness of the interdiffusion zone measured from the U-Mo vs. Al diffusion couples annealed at 600°C for 24 hours. The growth rate constant was calculated based on the assumption of parabolic growth.

Diffusion Couple	Thickness (µm)	Growth Constant, K (µm/sec$^{1/2}$)
U-7Mo vs. Al	265	0.90
U-10Mo vs. Al	542	1.84
U-12Mo vs. Al	352	1.20

In the low magnification micrographs presented in Figure 24, there are cracks within the interdiffusion zone. The population of cracks appears to be dependent on the Mo concentration in the terminal U-Mo alloy, and more cracks are observed in diffusion couples with higher initial Mo content in the terminal U-Mo alloy. Although the hardness of the interdiffusion zone was not measured in the interests of preserving the excellent diffusion bonding, the amount of cracks observed qualitatively indicates that the interdiffusion zone is more brittle with higher Mo concentration.

Detailed characterization of the interdiffusion zone was first carried out by SEM. Qualitative compositional contrasts from numerous backscatter micrographs were examined to discern different phases. Figure 25 presents backscatter electron micrographs of the interdiffusion zone (i.e., interaction layer) developed on the diffusion couples, (a) U-7 wt.% Mo, (b) U-10 wt.% Mo and (c) U-12 wt.% Mo vs. pure Al (99.999%), annealed at 600°C for 24 hours. Upon closer examination of this interaction layer, several features within the interaction layer were observed, including finely distributed grains (~100 nm) and layered, stratified microstructures. These features can be identified to some extent on Figure 25(a) since these fine features were most pronounced in U-7 wt.% Mo vs. pure Al, and least observable in U-12 wt.% Mo vs. pure Al.

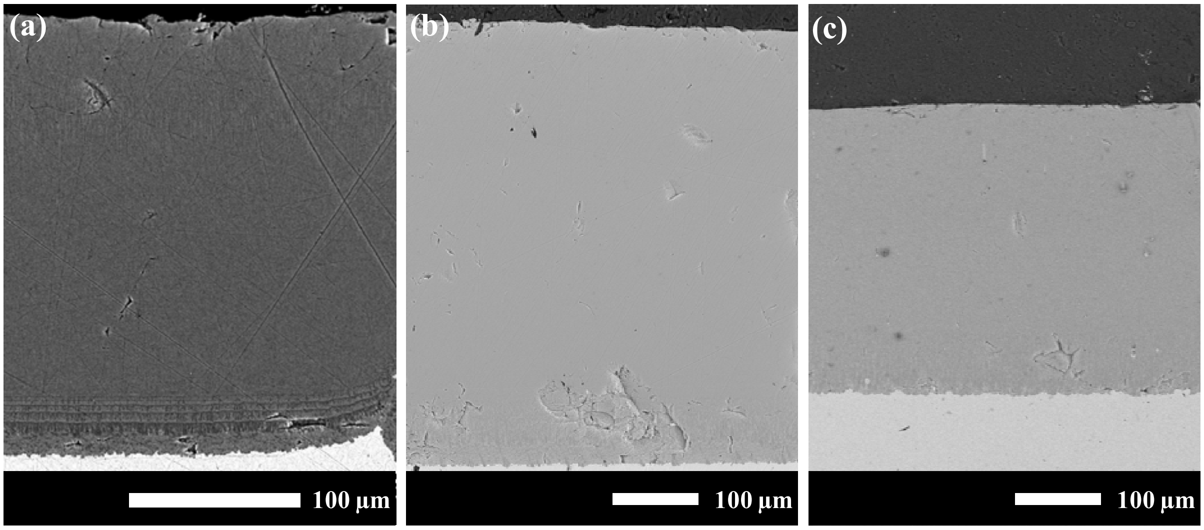

Figure 25. Backscatter electron micrographs of the interdiffusion zone defined as interaction layer in diffusion couples: (a) U-7Mo vs. Al, (b) U-10Mo vs. Al and (c) U-12Mo vs. Al annealed at 600°C for 24 hours.

Figure 26 through Figure 28 depict the complexity of microstructure within the interdiffusion zone for U-7 wt.% Mo, U-10 wt.% Mo and U-12 wt.% Mo, respectively, vs. pure Al (99.999%) diffusion couples, annealed at 600°C for 24 hours. In all three diffusion couples, a thin, two-phase region, approximately 1μm thick, developed within the interdiffusion zone, near to the Al/interdiffusion zone interface as presented in Figure 26(a), Figure 27(a) and Figure 28(a). Regions directly below the 1μm thick two-phase layer contain three phases with extremely fine grain size. These three-phase regions, shown by micrographs in Figure 26(a-f), Figure 27(a-f) and Figure 28(a-f) extend to make up most of the interdiffusion zone, and make up a layered morphology within the interdiffusion zone. SEM analysis did not permit detailed identification of the phase regions in the diffusion couples. The works of Palancher [56], Mazaudier [57] and Noël [61] found regions with differing phase distributions in their studies. In the current study, the observed layering through the interdiffusion zones may mark the boundaries between phase regions in these couples. Within the layers, backscatter contrasts showed that the phase regions near the center of the interdiffusion zones exhibited columnar microstructures as shown in Figure 26(d and e), Figure 27(c, d and e) and Figure 28(c, d, and e). Figure 26(b) also showed a columnar morphology near the Al/interdiffusion zone interface as shown in Figure 27(b). Near the U/Mo alloy, a non-continuous U-rich phase, in contact with the U-Mo/interdiffusion zone interface, was observed for all three couples as presented in Figure 26(f), Figure 27(f) and Figure 28(f). Qualitatively, the U-7Mo vs. Al diffusion couple showed the most complex microstructure within the interdiffusion zone, and the U-12Mo vs. Al couple showed the least complexity.

While no conclusive statements can be made regarding phase constituents from the complex micrographs presented in Figure 26, Figure 27 and Figure 28 due to the extremely fine-scaled microstructures and limited resolution of backscatter electron imaging, the interdiffusion zone clearly consisted of multiple phases and warranted detailed analyses by TEM, particularly using site-specific specimen preparation by FIB-INLO.

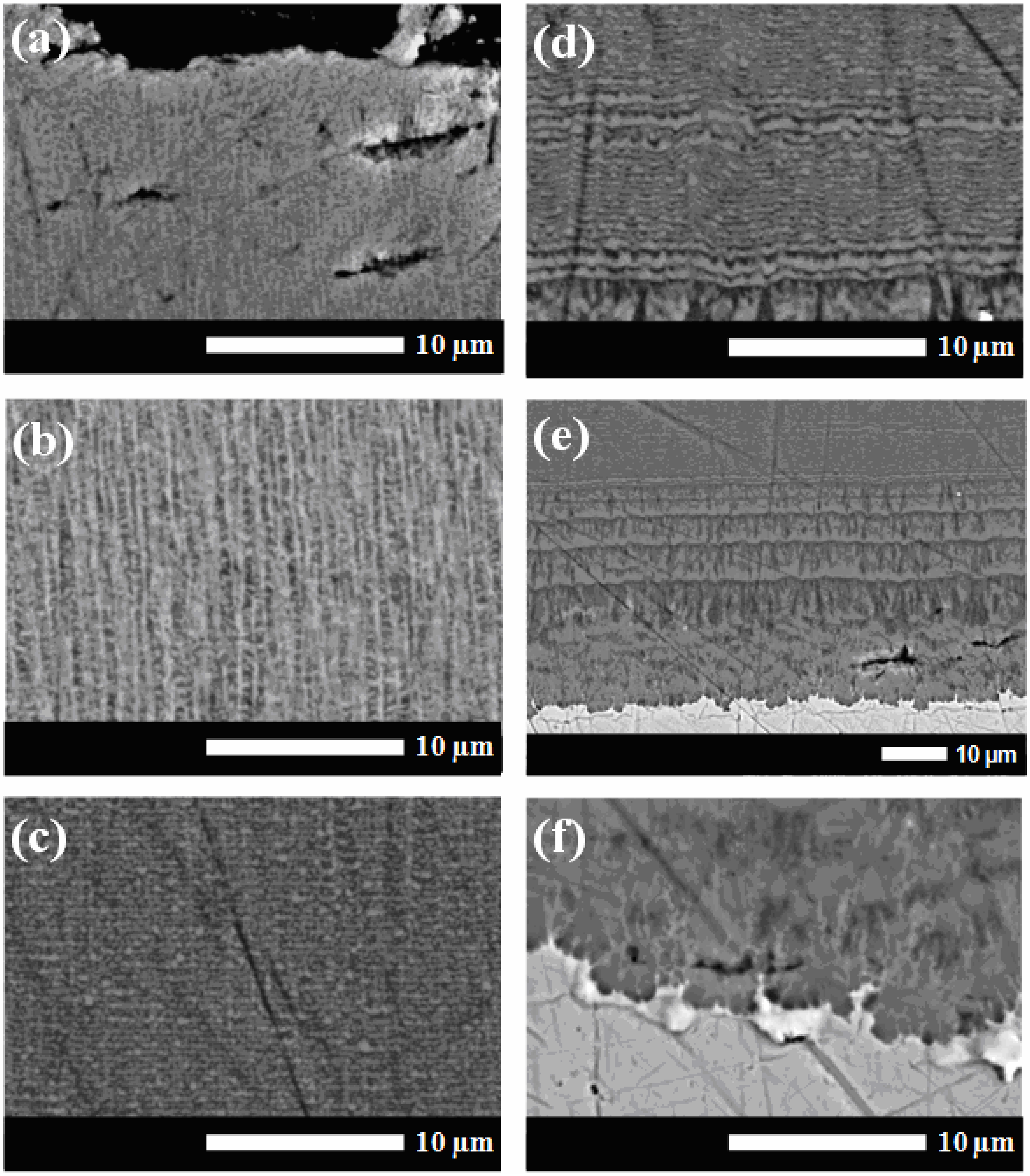

Figure 26. Detailed backscatter electron micrographs of the interdiffusion zone defined as interaction layer in U-7Mo vs. Al diffusion couple annealed at 600°C for 24 hours. (a) through (f) depict typical fine-scale microstructure from the Al/interdiffusion zone interface down to the interdiffusion zone/U-Mo interface.

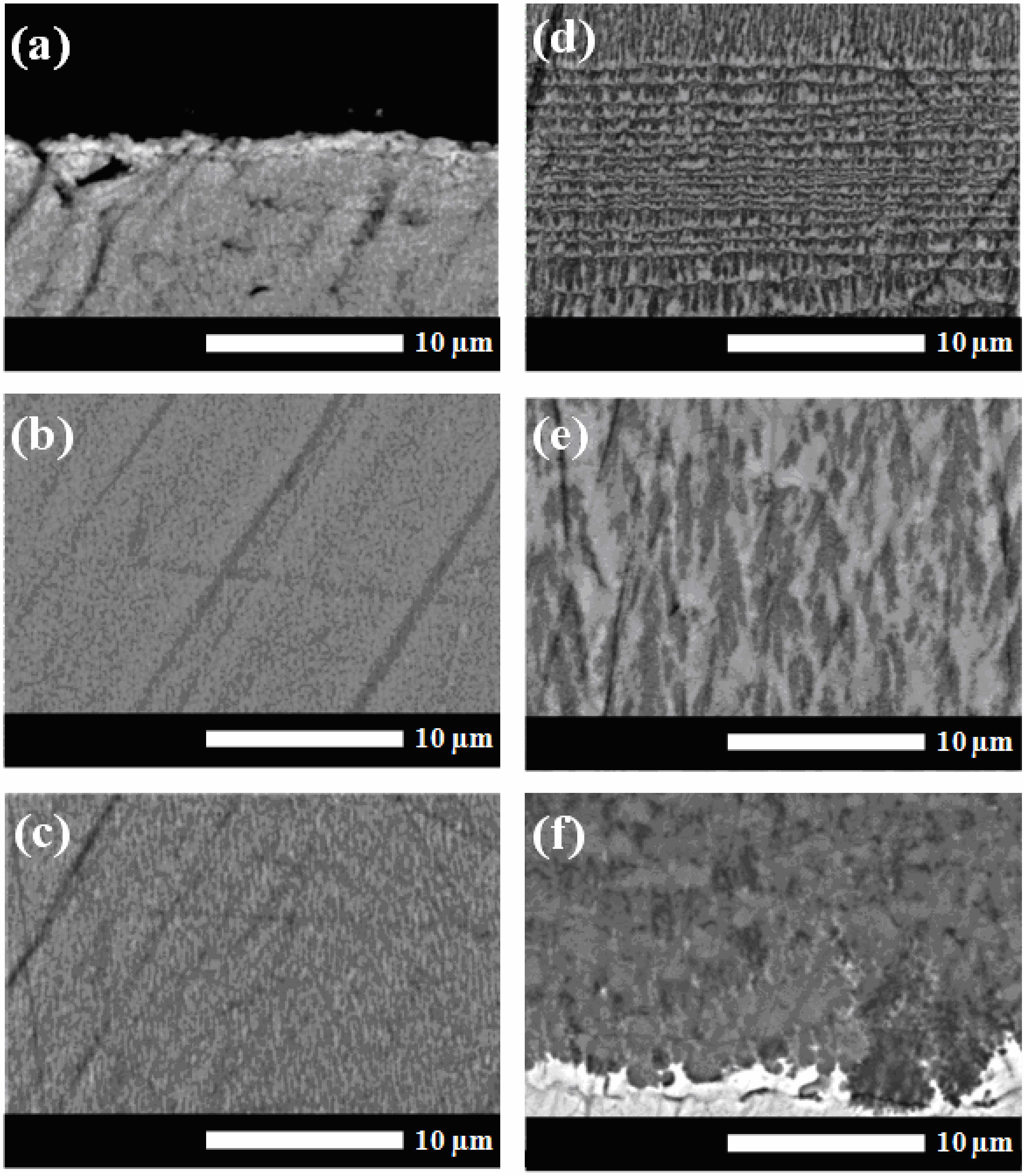

Figure 27. Detailed backscatter electron micrographs of the interdiffusion zone defined as interaction layer in U-10Mo vs. Al diffusion couple annealed at 600°C for 24 hours. (a) through (f) depict typical fine-scale microstructure from the Al/interdiffusion zone interface down to the interdiffusion zone/U-Mo interface.

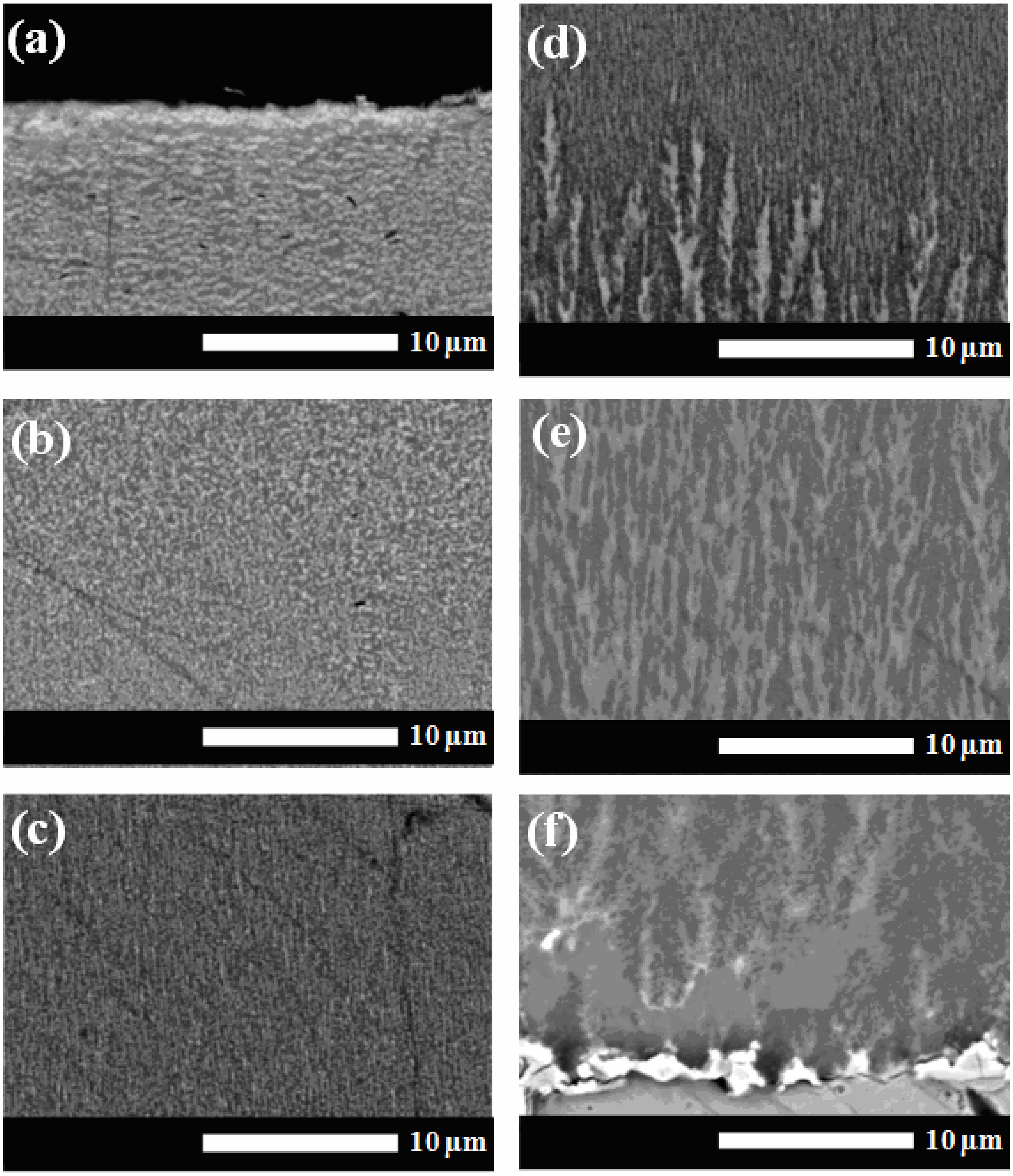

Figure 28. Detailed backscatter electron micrographs of the interdiffusion zone defined as interaction layer in U-12Mo vs. Al diffusion couple annealed at 600°C for 24 hours. (a) through (f) depict typical fine-scale microstructure from theAl/interdiffusion zone interface down to the interdiffusion zone/U-Mo interface.

Concentration profiles from these diffusion couples were determined by EPMA, and are presented in Figure 29 for the U-7Mo vs. Al, U-10Mo vs. Al and U-12Mo vs. Al diffusion couples, annealed at 600°C for 24 hours. The profiles appear very similar for all three couples. The concentrations of U, Mo and Al remained relatively constant throughout the entire interdiffusion zone thickness, despite the complex microstructure observed. Only a small variation (e.g., from high to low) in concentration in the order of a few atom percent over the entire length of the interaction layer was observed for U, Mo and Al in each diffusion couple. Although the measured changes in concentrations were repeatable based on multiple EPMA measurements, they fall within the experimental uncertainty and could not be analyzed further in terms of concentration gradients, $\partial c/\partial x$. Besides given the fine scale features with the presence of multi-phase layers observed by SEM, concentration measured by EPMA represents average value that depends both on fractional amount of constituent phases and composition of each phase. Figure 29 shows that a higher Mo concentration in the terminal U-Mo alloy gave rise to a higher concentration of Mo in the interdiffusion zone. An increase in Mo concentration in the diffusion zone corresponded to a decrease in U concentration. However, in all diffusion couples, the Al:(U+Mo) ratio remained consistently near 4:1. The actual measured compositions based on EPMA data had the average compositions for the U-7Mo, U-10Mo and U-12Mo vs. Al diffusion couples of 78.9Al-3.4Mo-17.6U, 79.7Al-4.4Mo-15.9U and 80.9Al-4.9Mo-14.2U (at.%), respectively, at the center of the interdiffusion zone. In accordance with backscatter electron micrographs, concentration profiles measured by EPMA showed that diffusion of Al into the bcc U-Mo alloys (e.g., solid-solution of Al in U-Mo alloys) and of U and/or Mo into the fcc Al (e.g., solid-solution of U or Mo in Al) did not occur as shown, and confirmed the limited solubility of the parent alloys into each other indicating that interactions immediately resulted in the development of the observed intermetallic phases.

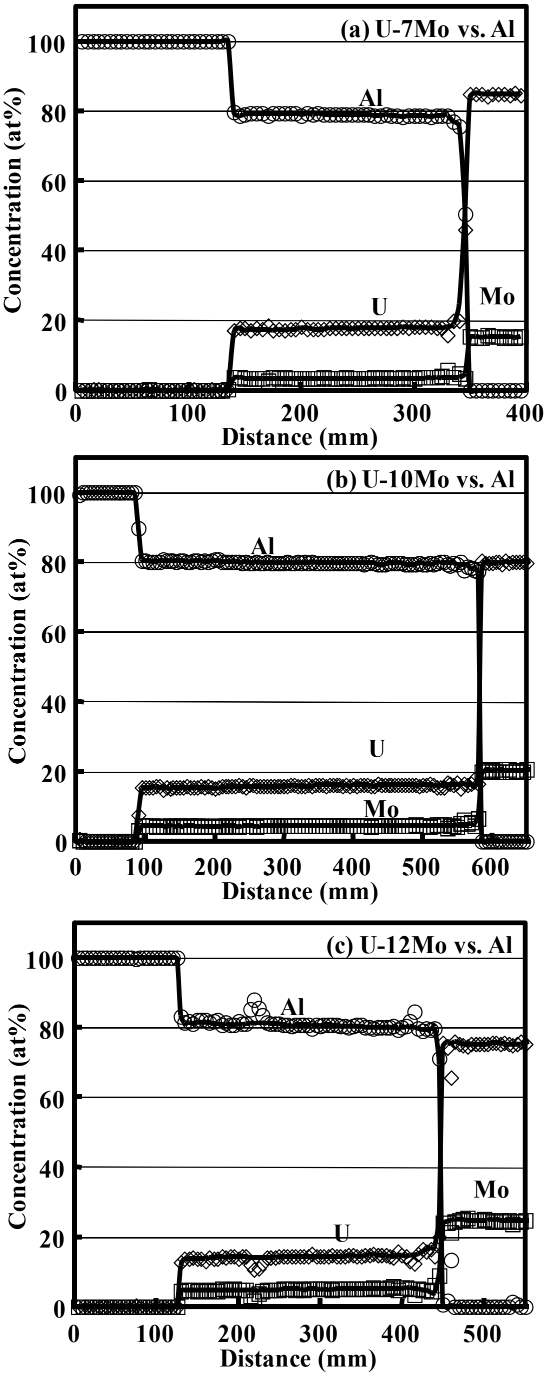

Figure 29. Concentration profiles measured by EPMA from the (a) U-7Mo vs. Al, (b) U-10Mo vs. Al and (c) U-12Mo vs. Al diffusion couples annealed at 600°C for 24 hours.

Further and detailed characterization of the interdiffusion zone was carried out by analytical TEM for phase constituent identification and semi-quanitative compositional analyses. The interdiffusion zone in the U-10Mo vs. Al diffusion couple was chosen for the analysis. The samples were prepared by FIB-INLO from each layer, both normal and along the direction of interdiffusion flux, and across relevant interfaces/boundaries observed in SEM. Figure 30 shows a FIB-generated micrograph of the interdiffusion zone in the U-10Mo vs. Al diffusion couple, and illustrates the locations where the TEM samples were prepared by FIB-INLO. The FIB-INLO sample preparation was carried out at locations that represented different microstructure observed by SEM (i.e., backscatter electron micrographs).

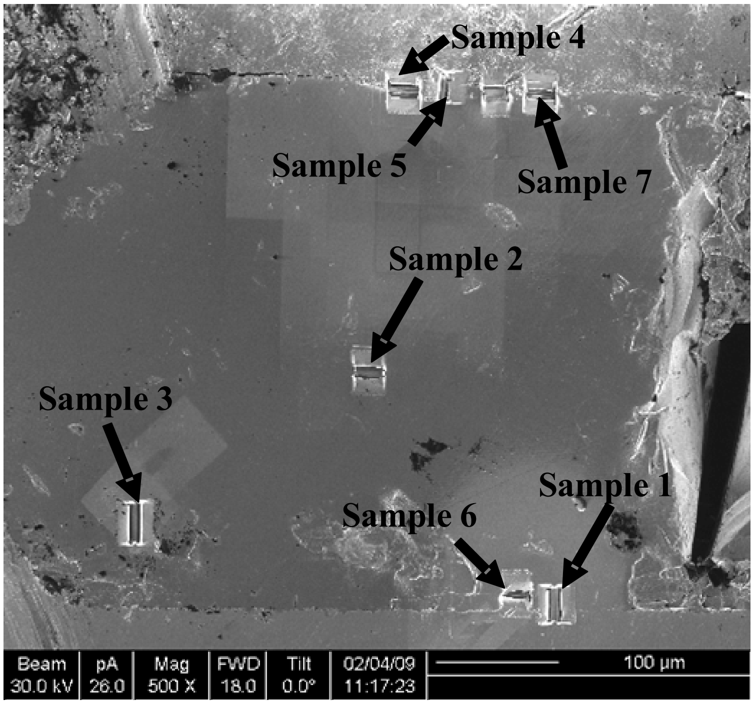

Figure 30. FIB-generated micrograph of the interdiffusion zone in the U-10Mo vs. Al diffusion couple, annealed at 600°C for 24 hours, illustrating the locations where the TEM samples were obtained by FIB-INLO.

Figure 31 (a-b) present typical bright-field TEM micrograph obtained from the middle of the interdiffusion zone of the U-10Mo vs. Al diffusion couple that was annealed at 600°C for 24 hours. This region made up most of the thickness (e.g., thickest layer observed in the backscatter electron micrographs) in the interaction layer. These micrographs show that the typical grain size observed is very small (~100 nm), in accordance with the fine features observed by backscatter electron micrographs shown in Figure 27(b,c).

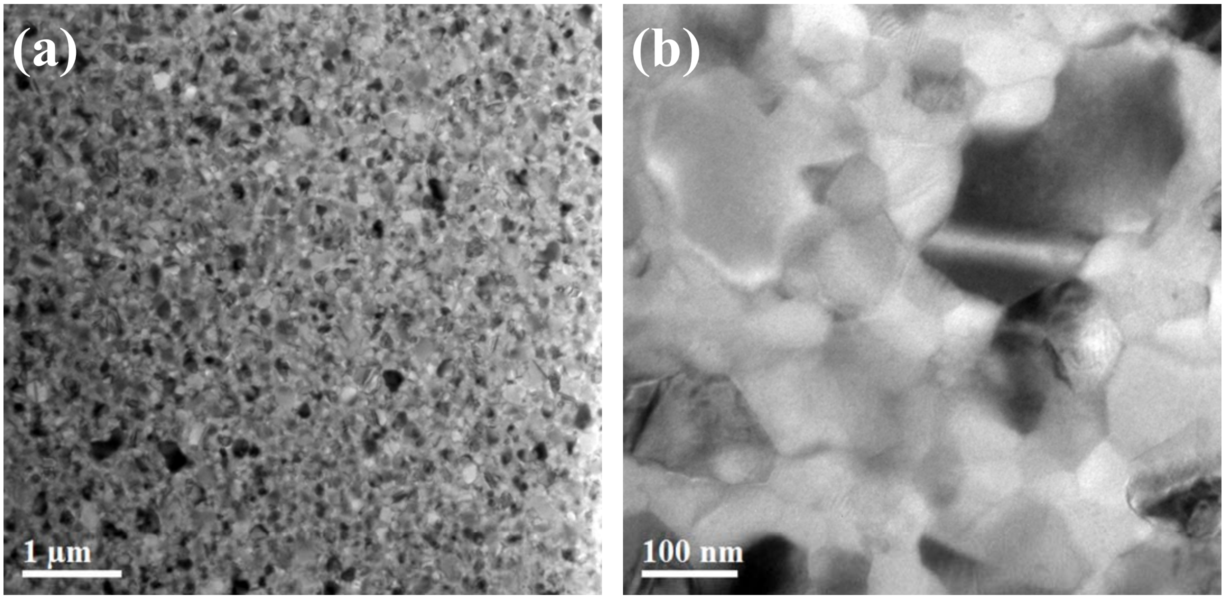

Figure 31. (a) A typical bright-field TEM micrograph obtained from the region near the center of the interdiffusion zone from the diffusion couple U-10Mo vs. Al, annealed at 600°C for 24 hours and (b) shows a detailed bright field micrograph of the same region.

Figure 32 presents HAADF micrographs from the same region in the middle of the interdiffusion zone in the U-10Mo vs. Al diffusion couple, annealed at 600°C for 24 hours. Based on compositional contrast of HAADF, these micrographs indicate that there are three phases present in this region. Selected area electron diffraction (SAED) patterns were collected and analyzed extensively to identify the three constituent phases, namely UAl_3, $U_6Mo_4Al_{43}$ and UMo_2Al_{20} as presented in Figure 33. Since the polycrystalline ring patterns from SAED, due to very small grain sizes, included several overlapping rings, their presence was further confirmed by convergent beam electron diffraction (CBED) as shown in Figure 34.

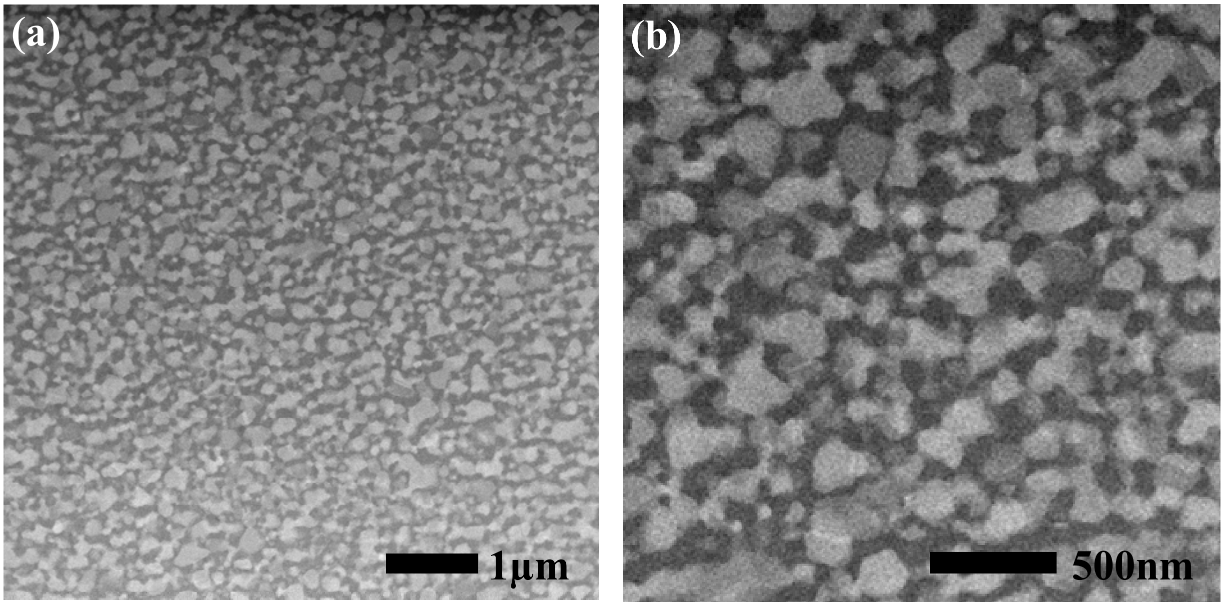

Figure 32 HAADF micrograph from (a) the middle of the interdiffusion zone in the diffusion couple U-10Mo vs. Al, annealed at 600°C for 24 hours; (b) showing the presence of three-phases. The HAADF contrast appears in (b) as dark gray, gray and light gray, and they correspond to UMo_2Al_{20}, $U_6Mo_4Al_{43}$, and UAl_3 phases based on atomic number contrast and electron diffraction analyses.

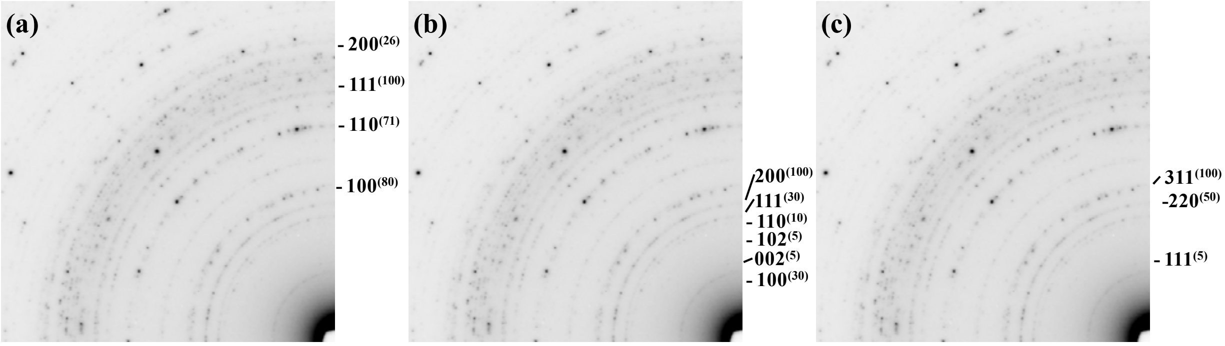

Figure 33. Selected area electron diffraction patterns obtained from the middle of the interdiffusion zone from the diffusion couple U-10Mo vs. Al, annealed at 600°C for 24 hours. The (a) UAl_3 (b) $U_6Mo_4Al_{43}$ and (c) UMo_2Al_{20} phases observed.

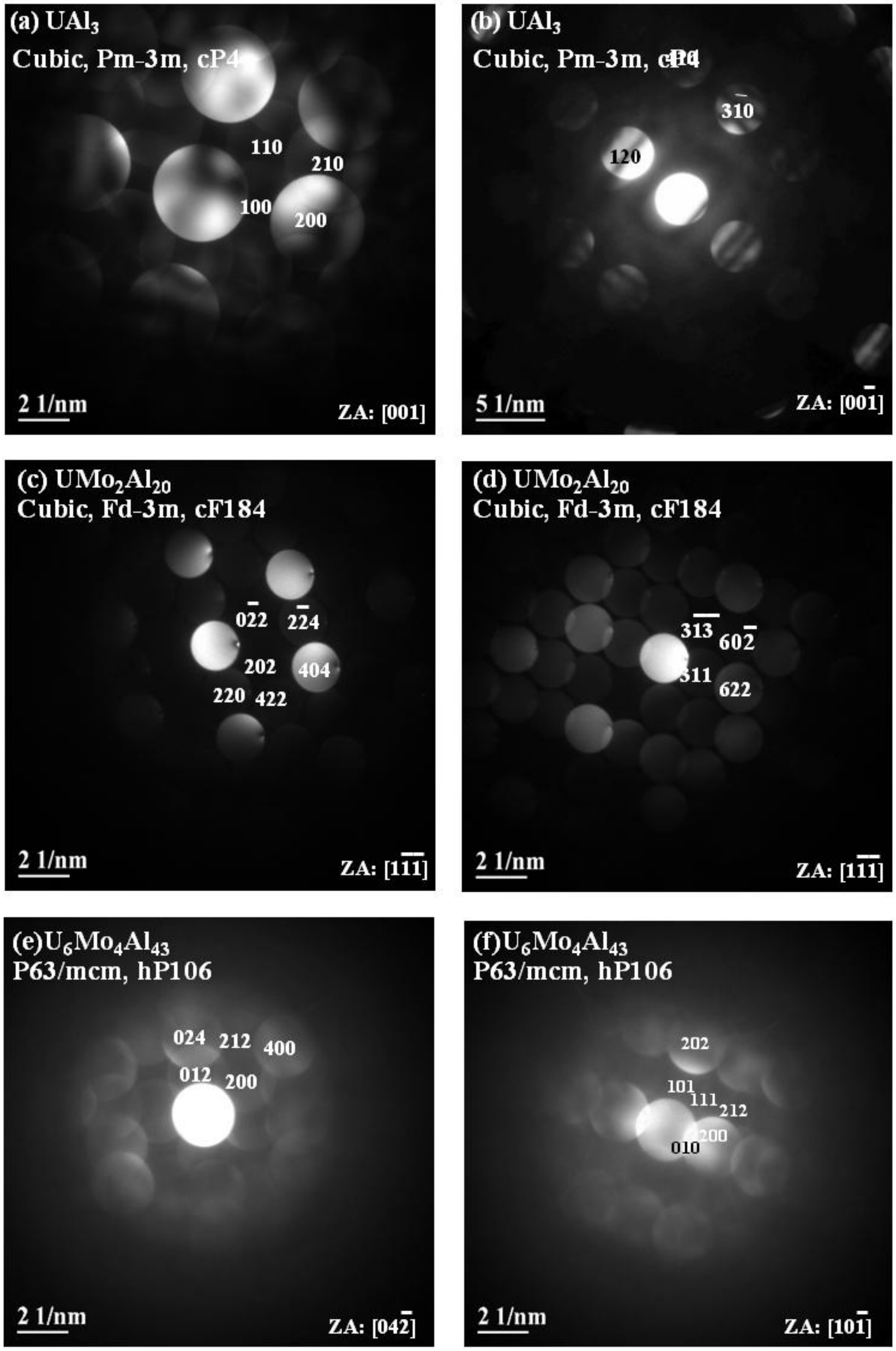

Figure 34. Convergent beam electron diffraction patterns obtained from the middle of the interdiffusion zone from the diffusion couple U-10Mo vs. Al, annealed at 600°C for 24 hours. The (a) UAl$_3$ (b) U$_6$Mo$_4$Al$_{43}$ and (c) UMo$_2$Al$_{20}$ phases observed.

A composite HAADF micrograph, presented in Figure 35, was obtained from a TEM specimen prepared by FIB-INLO parallel to the direction of interdiffusion flux from near the middle of the interdiffusion zone. It corresponds to the region shown by the backscatter electron micrographs shown in Figure 27(d). Detailed HAADF micrographs of selected regions shown in Figure 35(b) and Figure 35(c) and in more detail in Figure 35(d) and (e) highlight the distribution and fraction of phase constituents. These HAADF micrographs, again confirm that three phases are present within this region of the interdiffusion zone based on the contrast. The presence of these phases within the interdiffusion zone, namely the UAl_3, $U_6Mo_4Al_{43}$ and UMo_2Al_{20} phases was confirmed by additional electron diffraction analyses. However it should be noted that there is a substantial variation in the microstructure, i.e., layered vs. columnar, presented in Figure 35. These results indicate that the morphological variations do not correspond directly to the changes in the phase constituents. Furthermore, the expanding columnar microstructures observed in Figure 35(b-e) indicate that grain boundary or interphase boundary diffusion may play a significant role during the interdiffusion between U-Mo alloys and Al at 600°C.

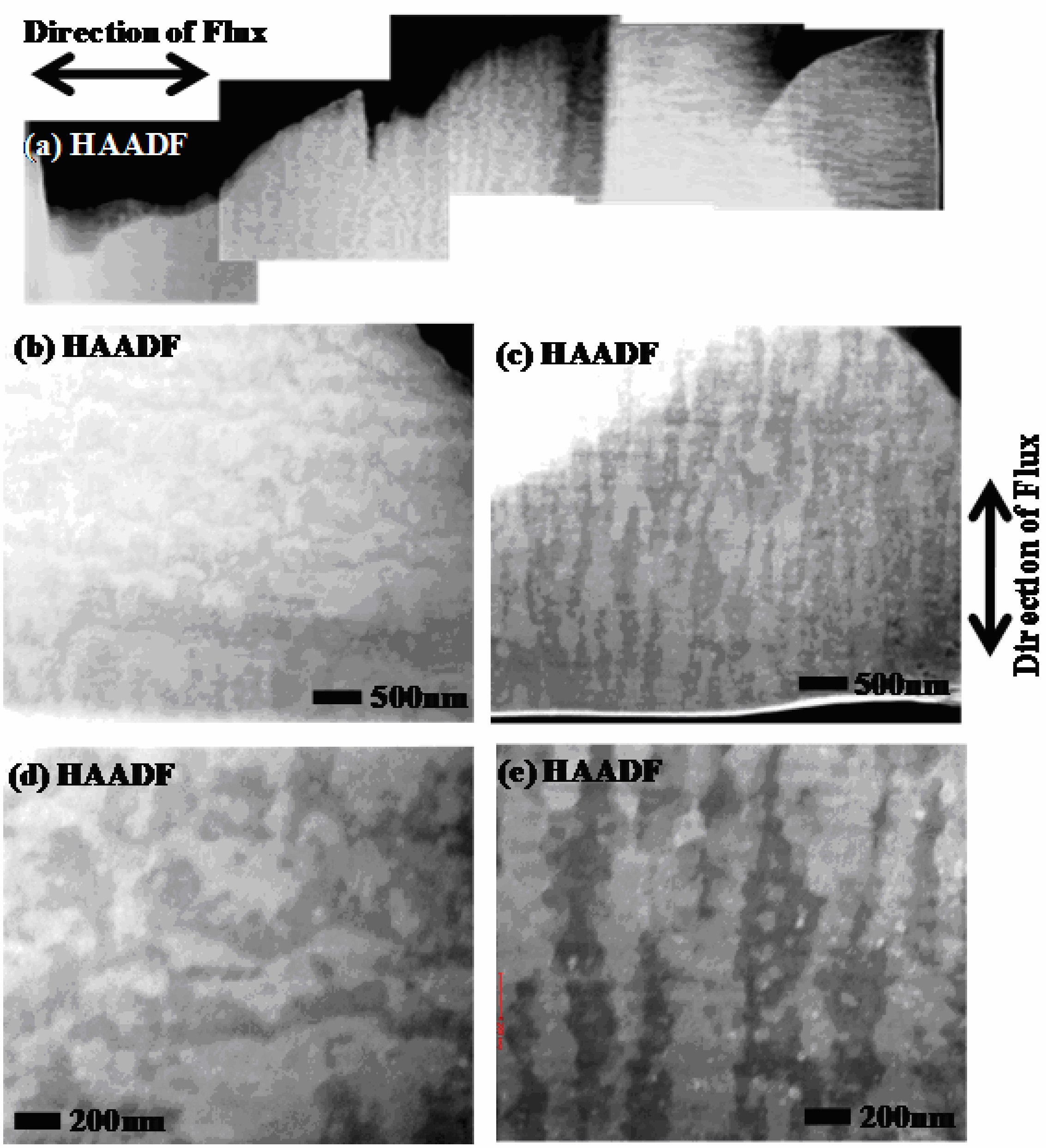

Figure 35. (a) HAADF micrographs obtained from the middle of the interdiffusion zone in the diffusion couple U-10Mo vs. Al, annealed at 600°C for 24 hours. TEM sample was prepared parallel to the direction of interdiffusion fluxes and (b,d) somewhat elongated layered structure and (c,e) columnar structure, despite having the same phase constituents of UAl_3, $U_6Mo_4Al_{43}$ and UMo_2Al_{20} phases.

Although some morphological changes were observed through the thickness of the interdiffusion zone as indicated by Figure 25(b) and Figure 27 (a-f), the three-phase region containing the UAl_3, $U_6Mo_4Al_{43}$ and UMo_2Al_{20} phases constituted the majority of the interdiffusion zone thickness, stretching from near the Al/interdiffusion zone interface to near U-Mo/interdiffusion zone interface. This three-phase layer was separated from the Al/interdiffusion zone interface by a thin, approximately 1µm thick, two-phase layer, as shown in Figure 27(a). Similar thin layers, observed by backscatter electron micrographs, were observed are shown in the U-7Mo and U-12Mo vs. Al diffusion couples respectively, and are shown in Figure 26(a) and Figure 28 (a). Figure 36(a) shows a HAADF micrograph of this region. The CBED patterns in Figure 36 (b-e) summarize the UAl_4 and UMo_2Al_{20} phases found within this layer. The phase compositions demonstrate Al enrichment of this layer due to its proximity to the Al/interdiffusion zone interface.

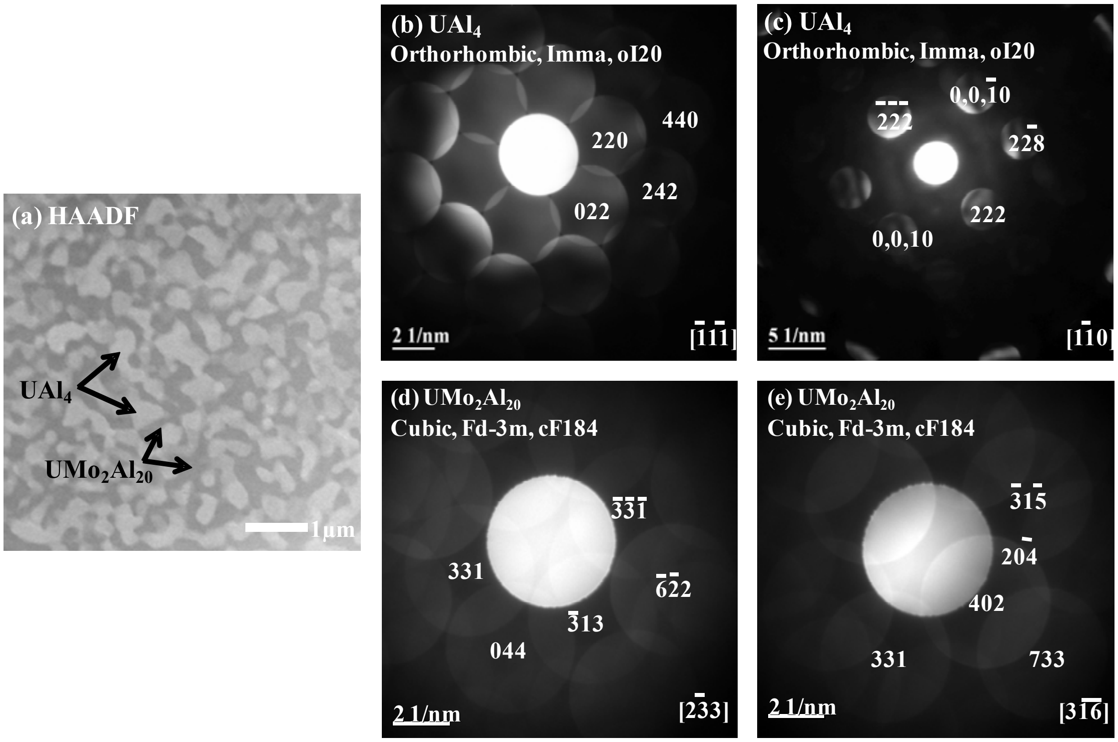

Figure 36. (a) HAADF micrograph from the thin layer observed near the Al/interdiffusion zone interface in the diffusion couple U-10Mo vs. Al, annealed at 600°C for 24 hours, and the corresponding CBED patterns from the (b-c) UAl4 and (d-e) UMo2Al20 phases.

Near the interface between the U-10Mo alloy and interdiffusion zone, despite the presence of a layered microstructure, in some areas the three-phase region containing UAl_3, $U_6Mo_4Al_{43}$ and UMo_2Al_{20} phases extended to the U-Mo alloy as presented in Figure 37(a). This TEM specimen was prepared parallel to the direction of the interdiffusion flux and includes the interface between the U-10Mo alloy and interdiffusion zone. In the U-Mo alloy very near the interface, the orthorhombic α-U grains were observed as shown in Figure 13(a). SAED patterns from α- and γ-U solid solution phases are presented in Figure 37(b) and Figure 37(c), respectively. This transformation of γ-to-α U solid solution was observed only at the interface between the U-10Mo alloy and interdiffusion zone, and not in the bulk U-Mo alloy. The Mo that was alloyed to stabilize the γ-U was depleted in the α-U grains observed near the interface.

Figure 38 presents backscatter electron micrographs of α-U phase layer observed at the interface between the U-Mo alloys and interdiffusion zone as a function of Mo content in the terminal U-Mo alloy. Cleary, as observed, the α-U layer developed on the U-7Mo vs. Al diffusion couple is more uniform and continuous than that found in the U-10Mo vs. Al diffusion couple. The α-U layer developed on the U-12Mo vs. Al diffusion couple is discontinuous. This series of backscatter electron micrographs indicate that the γ-to-α transformation was influenced by the Mo content in the initial U-Mo terminal alloy.

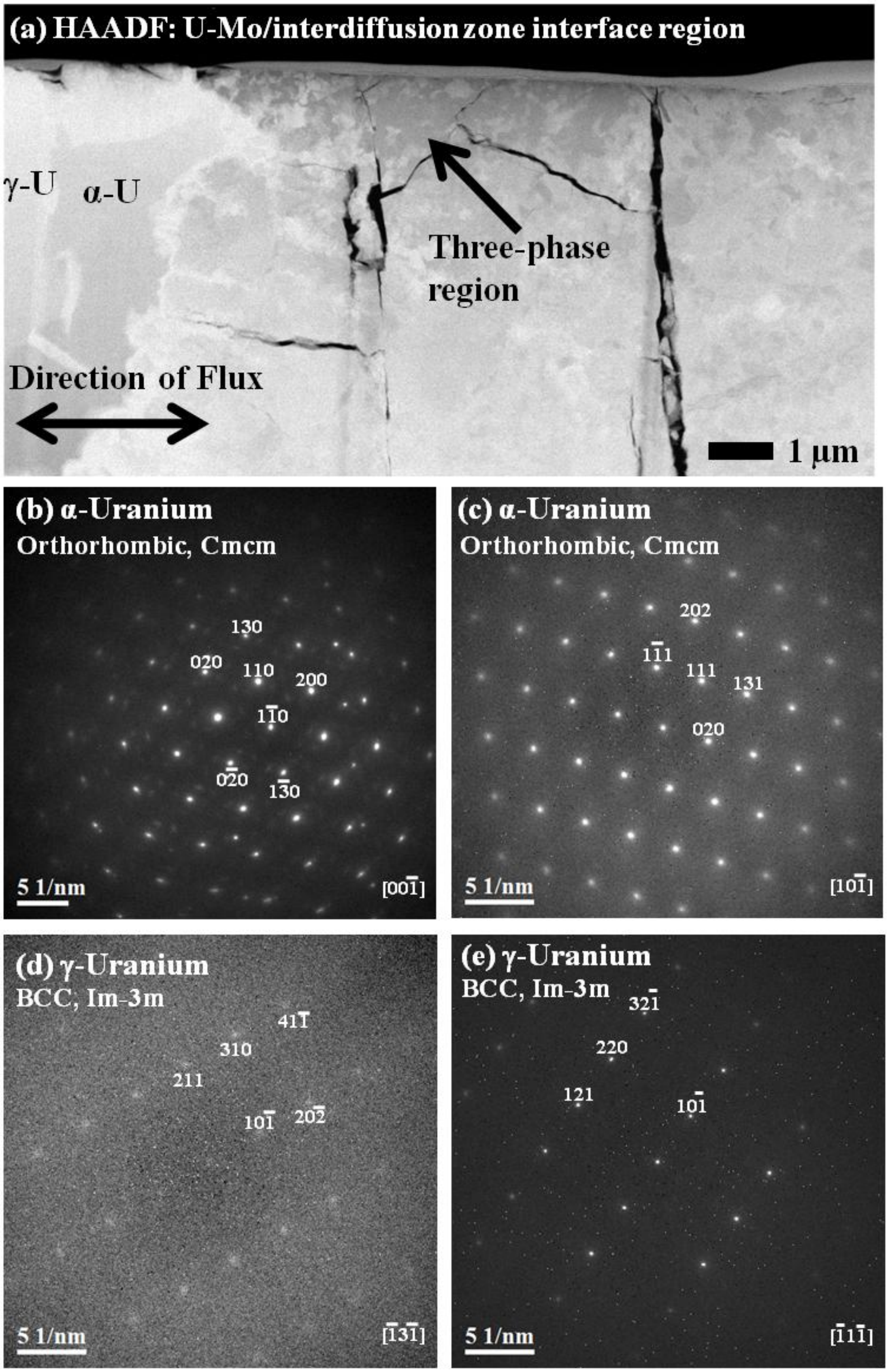

Figure 37. (a) HAADF micrograph of the interface between interdiffusion zone and U-10Mo alloy in the diffusion couple U-10Mo vs. Al, annealed at 600°C for 24 hours, and SAED patterns from the (b) orthorhombic α-U and (c) bcc γ-U phases.

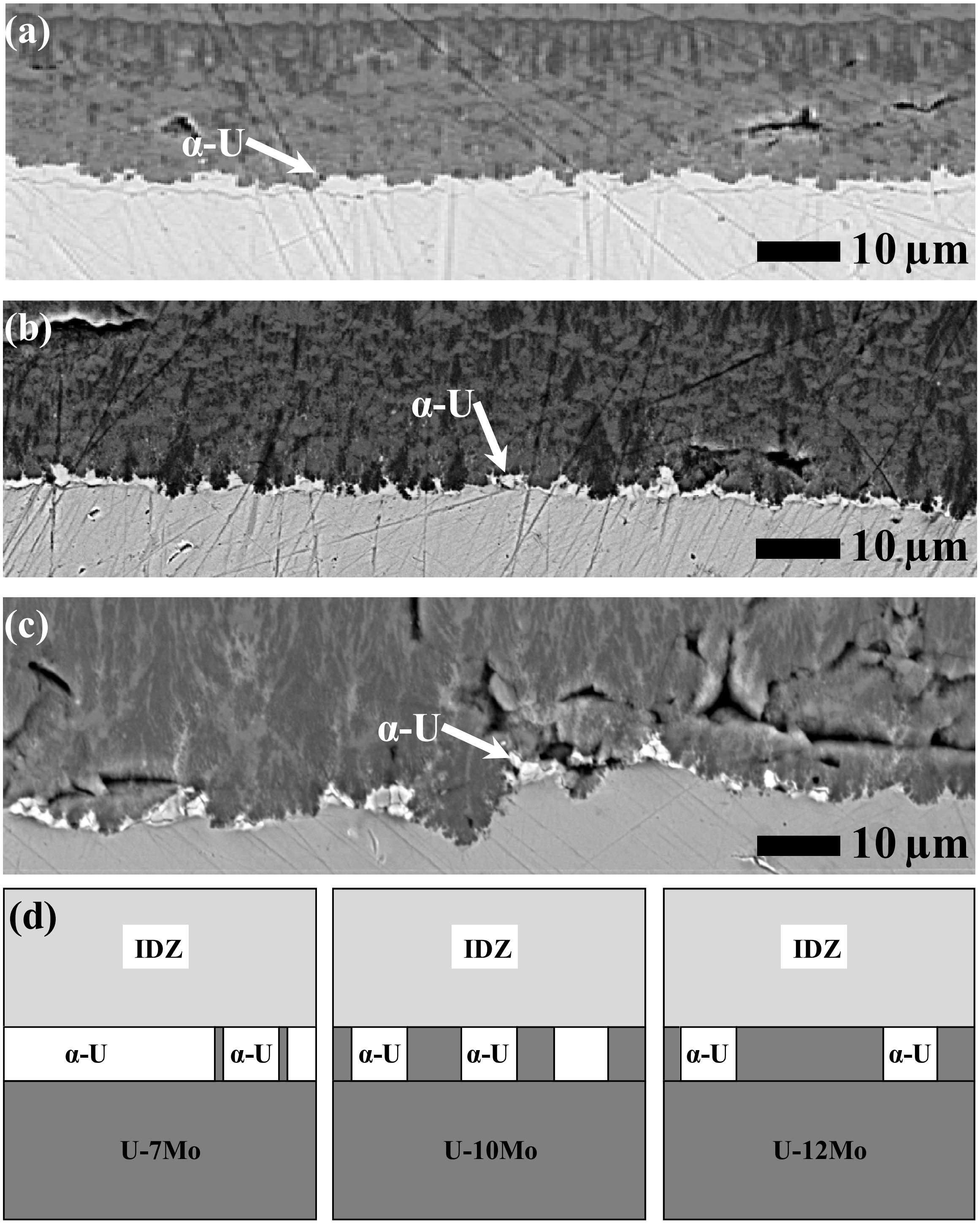

Figure 38. Backscatter electron micrographs illustrating the effect of Mo on the layer continuity of α-U phase from diffusion couples (a) U-7Mo vs. Al, (b) U-10Mo vs. Al and (c) U-12Mo vs. Al annealed at 600°C for 24 hours. (d) Schematic diagrams showing the differences in the interdiffusion zones.

4.4 Diffusion couples U-Mo vs. Al and Al-Si alloys annealed at 500°C for 1, 5 and 20 hours

A series of diffusion couples, U-7Mo, U-10Mo and U-12Mo vs. Al, Al-2Si and Al-5Si (wt.%), were annealed at 550°C for 1,5 and 20 hours. The compositions and temperatures were chosen to obtain relatively fast reaction rates and to prevent any unforeseen effects near the melting point of the Al-Si alloys. Table I summarizes thickness of the interdiffusion zones along with the calculated growth constants based on the assumption of parabolic growth in a fully diffusion controlled system, where the parabolic growth rate $K=T/t^{1/2}$ applies. The couples labeled N/A did not achieve acceptable bonding and were not considered in this study. Figure 39 presents backscatter electron micrographs of the U-7Mo, U-10Mo and U-12Mo vs. Al diffusion couples annealed at 550°C. Figure 40 shows the diffusion couples with U-7Mo, U-10Mo and U-12Mo vs. Al-2Si, and Figure 41 shows the U-7Mo, U-10Mo and U-12Mo vs. Al-5Si diffusion couples all annealed at 550°C.

Table 6. Thickness of the interdiffusion zone and growth constants for the U-7Mo, U-10Mo and U-12Mo vs. Al, Al-2Si and Al-5Si diffusion couples annealed at 550°C for 1, 5 and 20 hours.

Diffusion Couple 550°C	1 hour	5 hours (μm)	20 hours	Growth Constant (μm/sec$^{1/2}$)
U-7Mo vs. Al	31.4±1.8	158.7±59.8	N/A	0.85 ± 0.42
U-10Mo vs. Al	40.4±0.6	220.5±0.8	N/A	1.16 ± 0.69
U-12Mo vs. Al	22.4±1.2	182.2±1.9	628.4±6.3	1.36 ± 0.98
U-7Mo vs. Al-2Si	8.4 ± 1.4	N/A	N/A	0.14
U-10Mo vs. Al-2Si	9.7 ± 3.4	22.2 ± 3.1	29.7 ± 8.3	0.17 ± 0.01
U-12Mo vs. Al-2Si	10.1 ± 1.6	20.6 ± 2.3	52.2 ± 3.3	0.17 ± 0.02
U-7Mo vs. Al-5Si	7.0 ± 1.3	11.9 ± 2.5	13.3 ± 1.5	0.11 ± 0.02
U-10Mo vs. Al-5Si	8.6 ± 2.0	24.0 ± 1.8	56.7 ± 6.4	0.18 ± 0.03
U-12Mo vs. Al-5Si	6.8 ± 0.7	12.1 ± 2.8	28.9 ± 1.9	0.10 ± 0.01

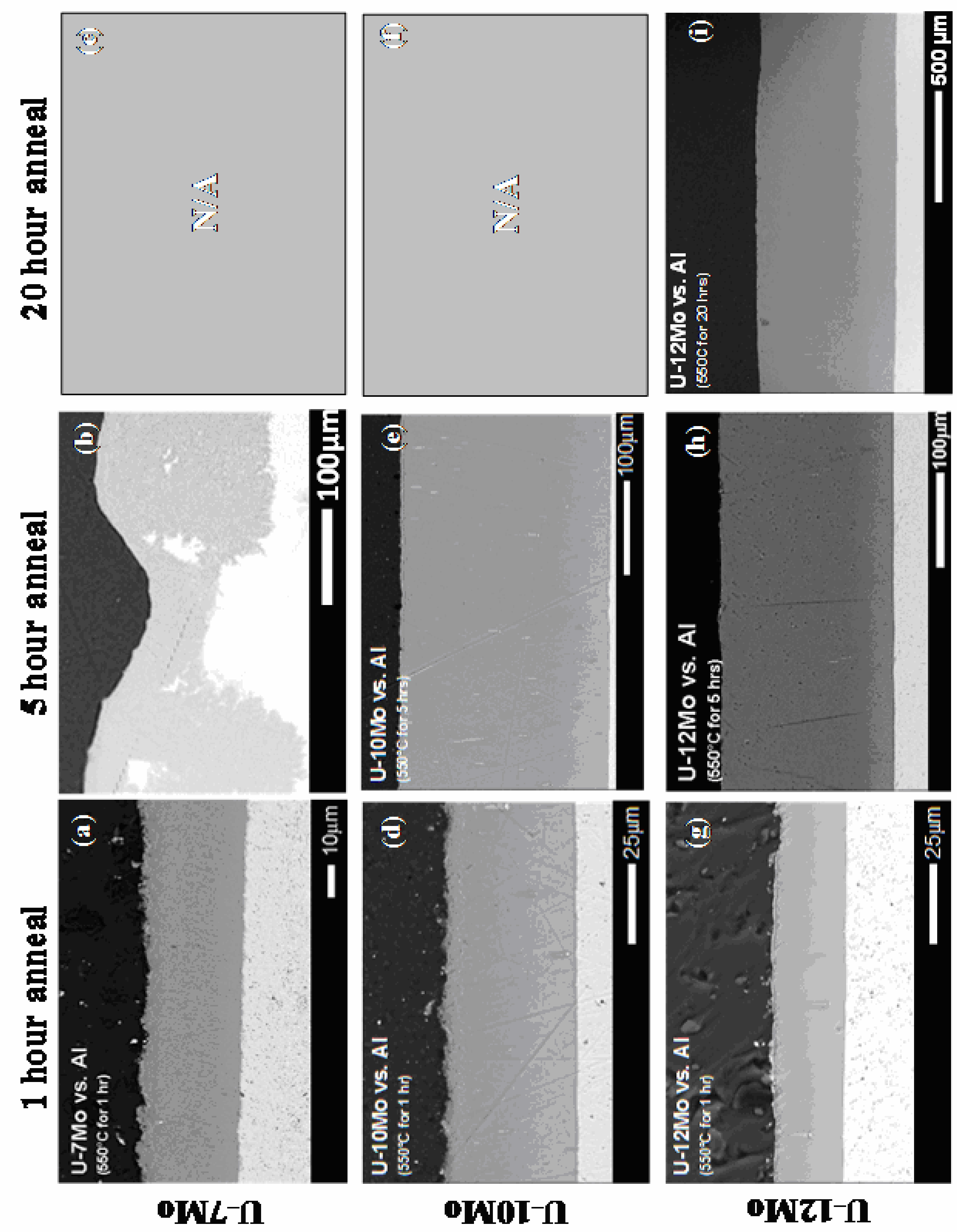

Figure 39. Diffusion couples of U-7Mo, U-10Mo and U-12Mo vs. Al annealed at 550°C for 1, 5 and 20 hours.

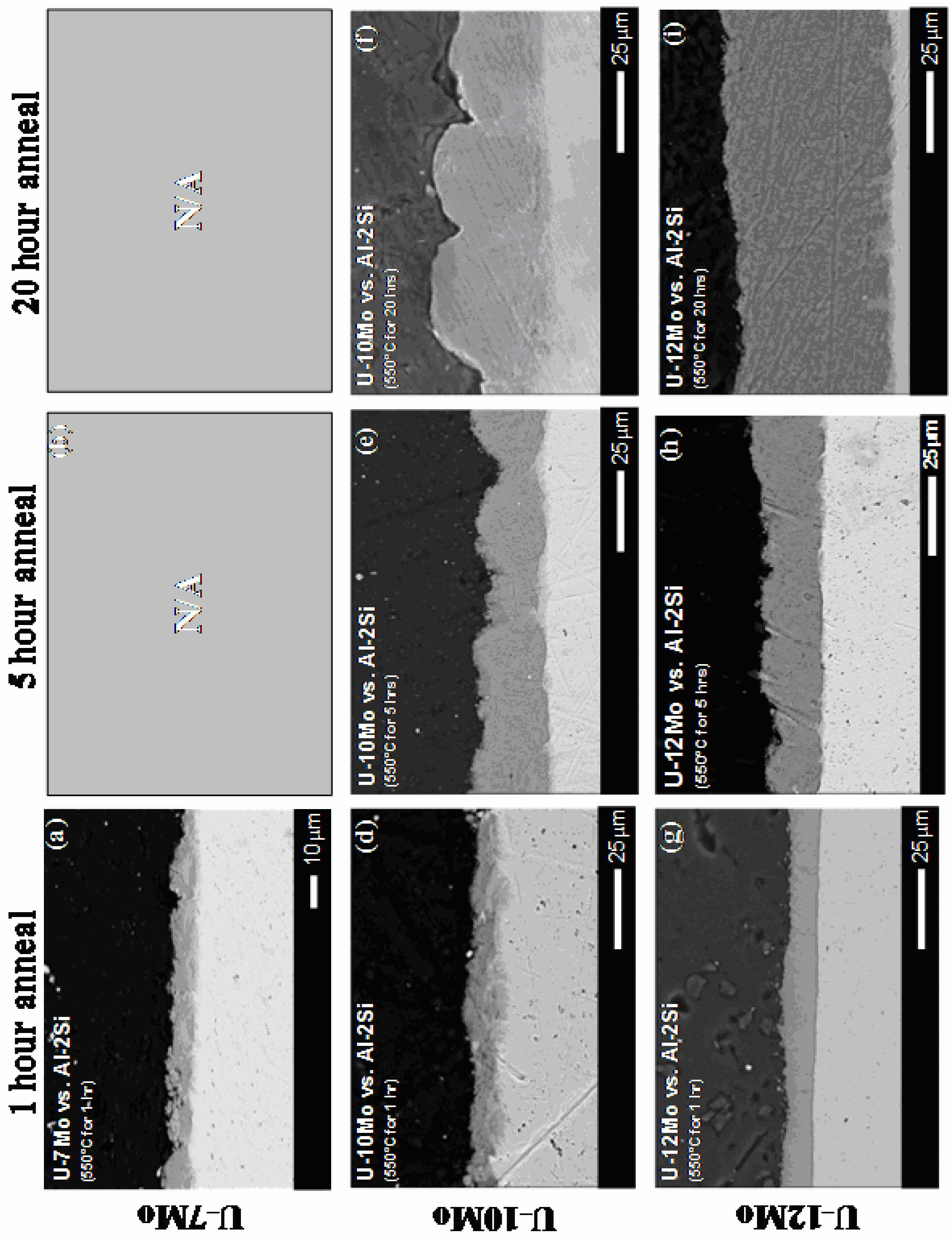

Figure 40. Diffusion couples of U-7Mo, U-10Mo and U-12Mo vs. Al-2Si annealed at 550°C for 1, 5 and 20 hours.

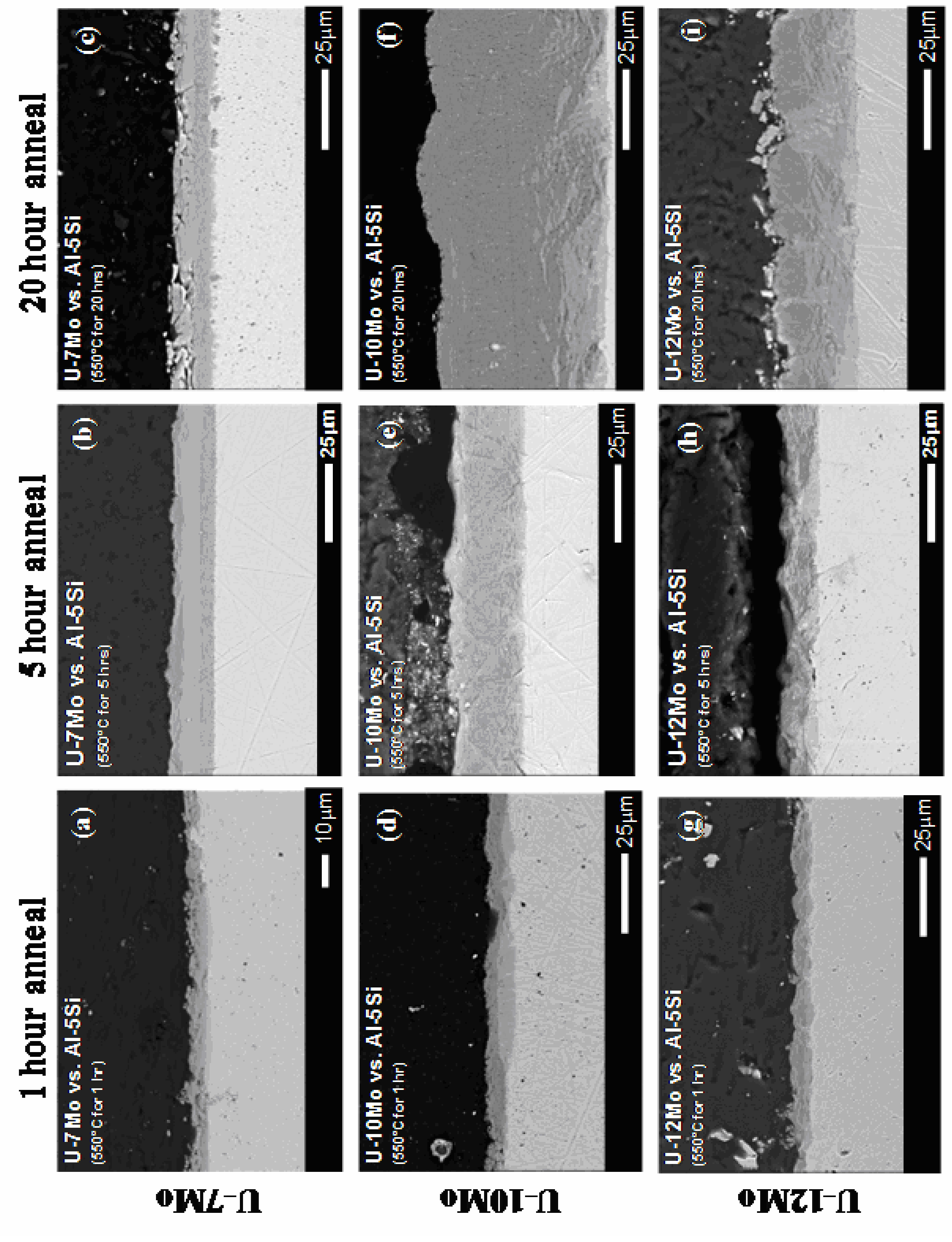

Figure 41. Diffusion couples of U-7Mo, U-10Mo and U-12Mo vs. Al-5Si annealed at 550°C for 1, 5 and 20 hours.

4.4.1 U-Mo vs. Al diffusion couples

Diffusion couples of U-7Mo, U-10Mo and U-12Mo vs. Al were annealed at 550°C for 1, 5 and 20 hours. Figure 39, Figure 40, and Figure 41 show backscatter electron micrographs of the U-Mo alloys vs. Al, Al-2Si and Al-5Si diffusion couples respectively, annealed at 550°C for 1, 5 and 20 hours showing the development of the interdiffusion zone as a function of time and composition. The γ-U$\rightarrow$(α-U + δ-U_2Mo) decomposition takes place below 573°C [21], as shown in Figure 1 for the compositions under consideration. Based on the decomposition rates measured in the U-Mo TTT-diagrams by P.E Repas [21] and Y. Goldstain [22], only the U-7Mo alloy was expected to undergo decomposition, given the chosen anneal times and temperatures. Where decomposition of the U-Mo alloy was not observed, the interdiffusion zone interfaces generally remained planar. Where decomposition of the γ-U phase took place, and due to fast Al diffusion in the α-U phase, the U-Mo/interdiffusion-zone-interface changed from planar interfaces to lamellar microstructures as shown in Figure 42(a-b). Figure 42(c) shows a detailed micrograph of the lamellar microstructure. The light-gray region is the unreacted γ-U phase. The mid-gray regions were regions that decomposed into the α-U phase, where Al has diffused. The dark bands that surround the reacted α-U phase and separate it from the γ-U phase, based on U-Mo decomposition, likely contain the δ-U_2Mo phase. Because of the fine microstructure, XEDS analysis by SEM of these phase regions was not possible.

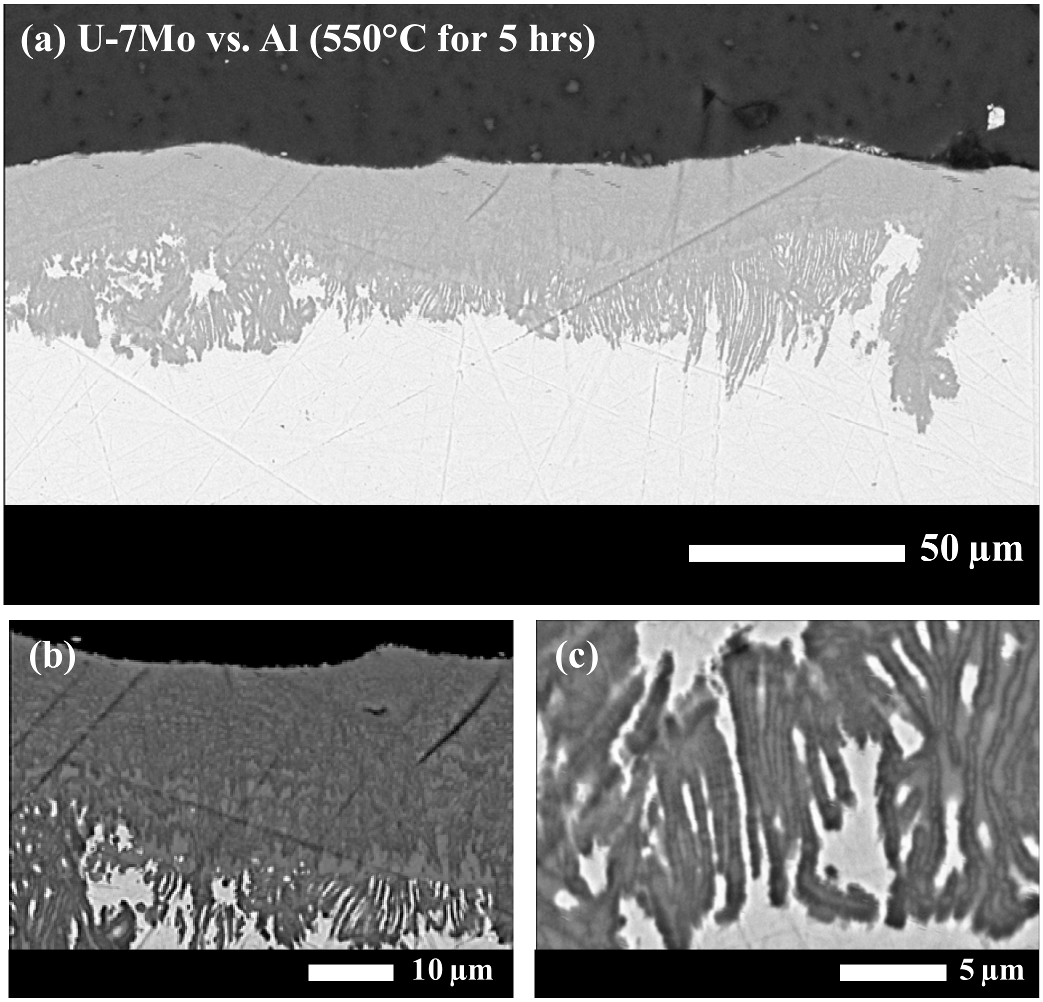

Figure 42. (a) Typical microstructure of diffusion couples of U-Mo vs. Al where the γ→(α+δ) decomposition has taken place, and (b) shows a more detailed micrograph, and (c) shows the detailed microstructure of the decomposed and interacted region of the U-Mo alloy.

The interdiffusion zones developed complex multiphase microstructures within one hour of diffusion anneal as shown in Figure 43 for the U-7Mo vs. Al diffusion couple annealed for 1 hour at 550°C. Figure 43 (a) shows the general morphology of the interdiffusion zone. Morphological differences were observed in the interdiffusion microstructures indicating the development of layered morphologies, and Figure 43 (b) and (c) show fine-grained microstructures typical of the diffusion couples annealed at 550°C. Near the top of the interdiffusion zone near the Al in Figure 43 (a) periodic layers appear to have developed, similar to those observed at 600°C. This study, therefore, assumed that the phase development of diffusion couples is identical or very similar to that at 600°C.

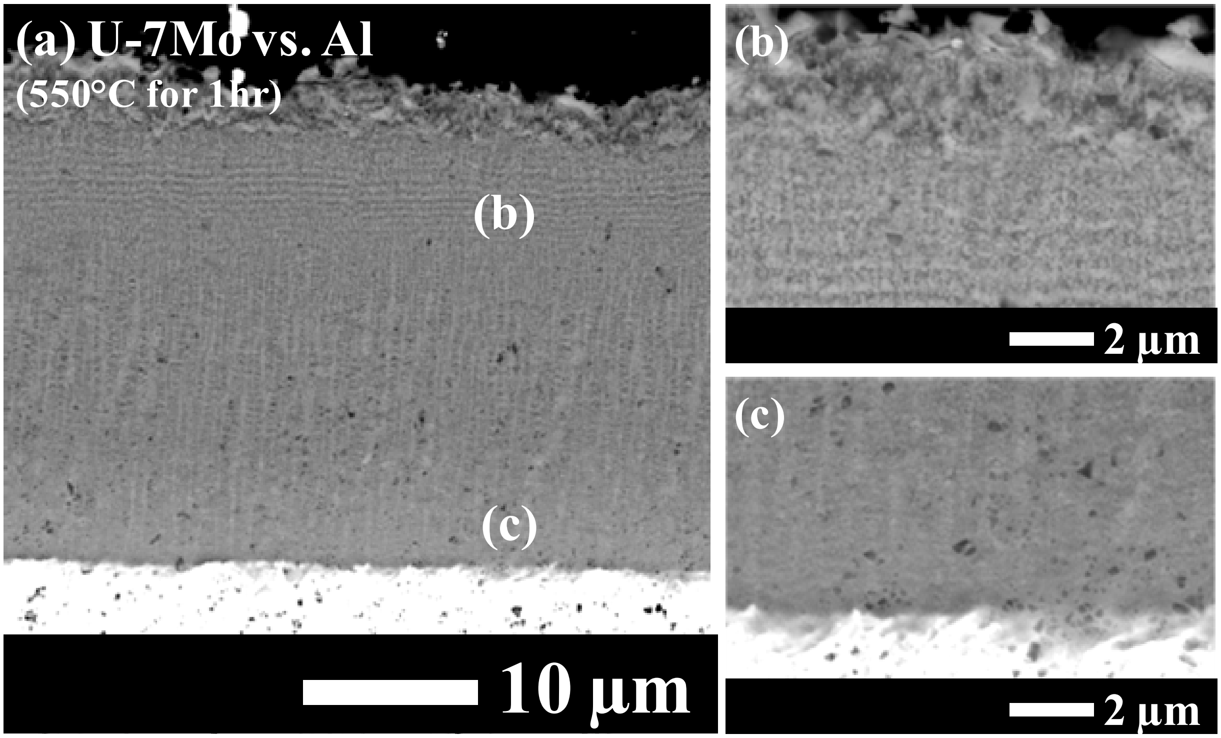

Figure 43. High contrast backscatter electron micrograph of the (a) U-7Mo vs. Al diffusion couple annealed for 1 hour showing the fine microstructure of the interdiffusion zone (b) near the Al interface and (c) near the U-Mo interface.

An analysis performed on the diffusion couples by XEDS standardless analysis showed that the interdiffusion zones in those couples had an Al average composition of approximately 75-80 at.%, with relatively flat concentration profiles where the average interdiffusion zone composition remained relatively constant throughout the interdiffusion zone thickness. Although within the experimental error of the XEDS equipment, a similar decrease in Al concentration, as was the case for the couples annealed at 600°C, from the Al side to the U-Mo side of the couples was observed in the concentration profiles of the couples annealed at 550°C. The Mo concentrations in the interdiffusion zones were similarly found to be a function of the Mo concentration in the terminal U-Mo alloy. Figure 44 shows a typical concentration profile for the diffusion couples containing U-Mo alloys vs. pure Al annealed at 550°C; the figure shows the concentration profile for the U-10Mo vs. Al diffusion couple annealed at 550°C for 5 hours.

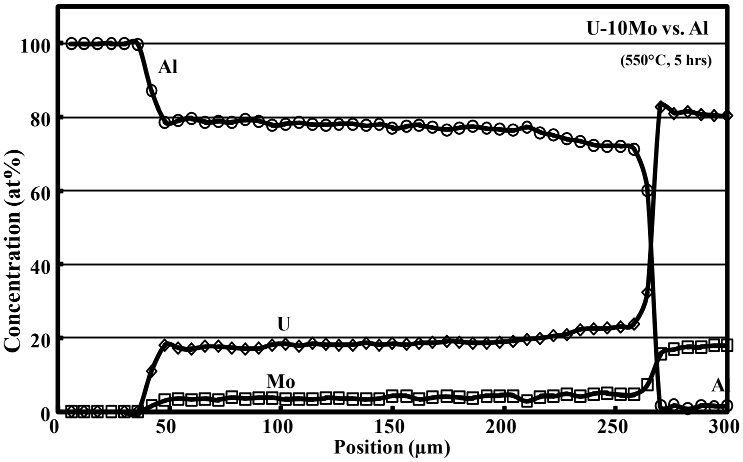

Figure 44. Concentration profile of the U-10Mo vs. Al diffusion couple annealed at 550°C for 5 hours.

Detailed characterization of the diffusion couples of U-10Mo vs. Al annealed at 600°C for 24 hours showed that the observed microstructures in diffusion couples of U-Mo vs. Al alloys consisted of two- and three-phase regions in layered microstructures that contained a combination of the UAl_3, UAl_4, $U_6Mo_4Al_{43}$ and UMo_2Al_{20} phases. The bulk of the interdiffusion zone was composed of a three phase region containing the UAl_3, $U_6Mo_4Al_{43}$ and UMo_2Al_{20} phases. The regions near the Al/interdiffusion-zone-interface and U-Mo/interdiffusion zone interfaces were composed of two-phase regions with (UAl_4+ UMo_2Al_{20}) and (UAl_3 + $U_6Mo_4Al_{43}$) phases respectively. Because of the similarities between the diffusion couples annealed at 600°C and 550°C, and because the UAl_3, $U_6Mo_4Al_{43}$ and UMo_2Al_{20} phases have been identified at lower temperatures [62], this study assumed that the interdiffusion zones in the diffusion couples of U-Mo vs. pure Al annealed at 550°C were similar in phase constituents to those of couples annealed at 600°C and contained similar phase distributions.

4.4.2 U-Mo vs. Al-Si diffusion couples

Diffusion couples of U-7Mo, U-10Mo and U-12Mo vs. Al-2Si and Al-5Si were annealed at 550°C for 1, 5 and 20 hours. Figure 40 and Figure 41 shows microstructures of the diffusion couples containing Al-2Si and Al-5Si, respectively. Typically, the interdiffusion zones in diffusion couples containing Al-Si alloys developed fine-grained microstructures similar only in appearance to that of the couples containing only pure Al, but with different compositions and phase constituent distributions. The interdiffusion zones typically developed planar interfaces at the U-Mo/interdiffusion-zone-interface, but showed some roughening at the Al/interdiffusion-zone-interface.

Figure 45 shows a detailed backscatter electron micrograph of the interdiffusion zone in the U-10Mo vs. Al-5Si diffusion couple annealed at 550°C for 5 hours. The interdiffusion zones in diffusion couples containing Al-2Si and Al-5Si in this study developed generally similarly to those shown in Figure 45: very fine multi-phase microstructures developed, and the interdiffusion zones partitioned into layered morphologies. The morphological changes generally marked variations in the distributions of the elements and/or phase constituents. The interdiffusion zones are typically divided into three regions labeled (i), (ii) and (iii) on the micrograph. Results from XEDS characterization showed that the average compositions of these regions varied in Al and Si concentrations. XEDS results showed that the Al and Si seemed to substitute for each other in the interdiffusion zones to maintain the composition near 75-80 at.% (Al,Si) for most of the interdiffusion zone thickness. XEDS of each diffusion couple containing Si showed that Si was present throughout the interdiffusion zone thickness. Nonetheless, in the diffusion couples of U-7Mo vs. Al-2Si and Al-5Si alloys, a Si enriched region developed near the center of the interdiffusion zone. In the U-10 and U-12Mo vs. Al-2Si and Al-5Si alloys, the Si-rich region of the interdiffusion zone always developed and remained near the U-Mo/interdiffusion zone interface. Figure 46 shows contrast enhanced backscatter electron micrographs of the (a) U-7Mo vs. Al-5Si and (b) the U-10Mo vs. Al-5Si diffusion couples annealed for 5 hours emphasizing the two different Si distributions.

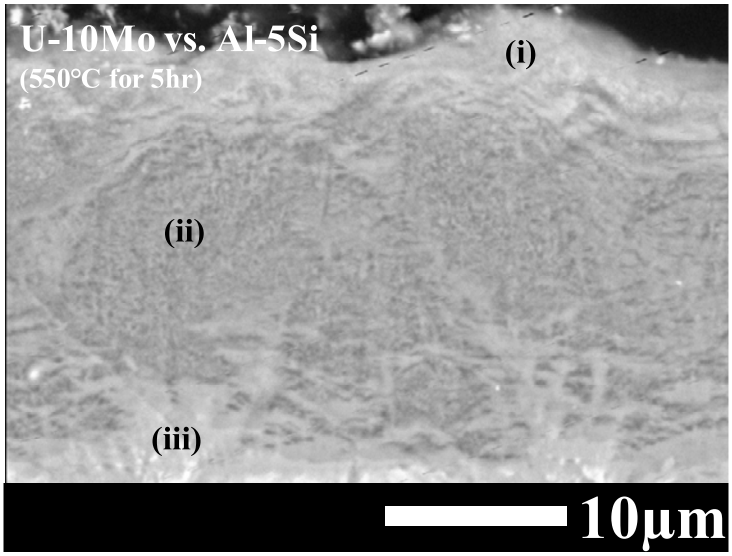

Figure 45. Backscatter electron micrograph of the interdiffusion zone in the U-10Mo vs. Al-5Si diffusion couple annealed at 550°C for 5 hours.

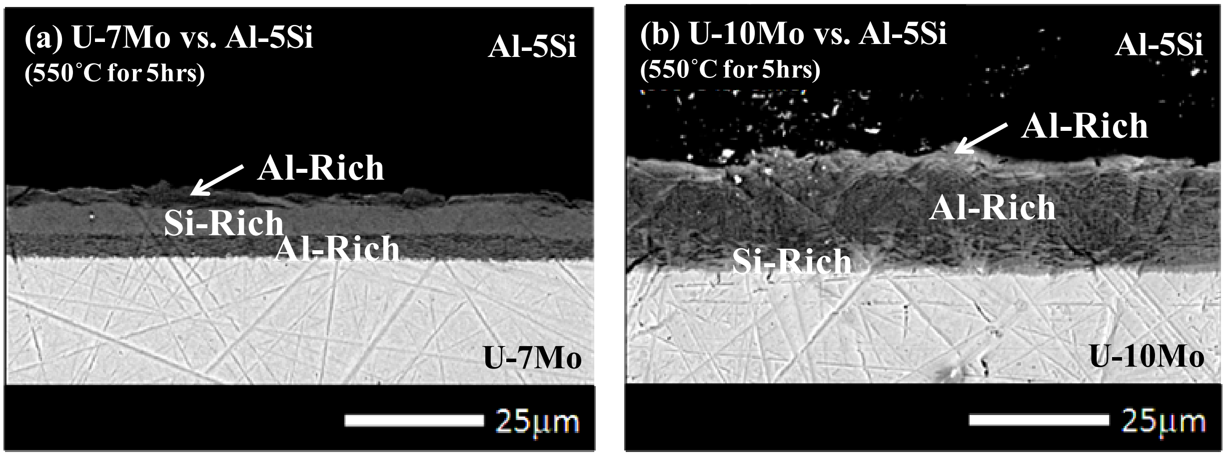

Figure 46. Contrast enhanced backscatter micrographs of the (a) U-7Mo vs. Al-5Si and (b) the U-10Mo vs. Al-5Si diffusion couples annealed at 550°C for 5 hours, showing Si distributions in the interdiffusion zones.

In order to characterize the phases in the interdiffusion zones of diffusion couples containing Si in the Al-alloy, a TEM analysis of the U-7Mo vs. Al-2Si and U-7Mo vs. Al-5Si diffusion couples annealed for 1 and 5 hours, respectively, was carried out. Because of the small grain size, only multi-grain SAED patterns of the interdiffusion zone were collected for the U-7Mo vs. Al-2Si annealed for 1 hour; Figure 47(a) shows a HAADF micrograph of the interdiffusion zone, and Figure 47(b) presents a very fine grained microstructure within the interdiffusion zone. Figure 48(a) shows a wide area electron diffraction pattern of the interdiffusion zone identifying the UAl_3 phase in the interdiffusion zone. Because XEDS analysis on single grains showed that grains with the UAl_3 crystal structure contained significant concentrations in Si and Mo, Si appears to open the solubility for Mo into this phase. The phase composition is re-written as $(U,Mo)(Al,Si)_3$ to account for solid solubility of the elements in this phase. The UMo_2Al_{20} was also identified throughout the thickness of the interdiffusion zone on relatively faint rings in the SAED patterns as presented in Figure 48(b).

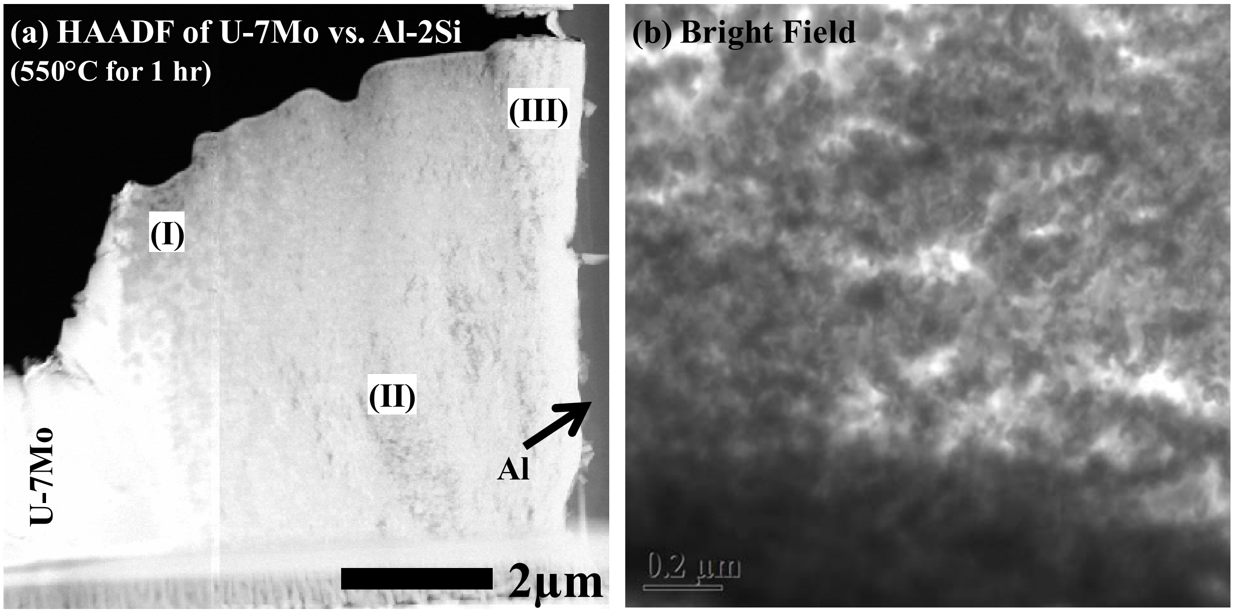

Figure 47. (a)HAAFD micrograph of the complete interdiffusion zone for the U-7Mo vs. Al-2Si annealed for 1 hour. (b) a detailed bright field micrograph.

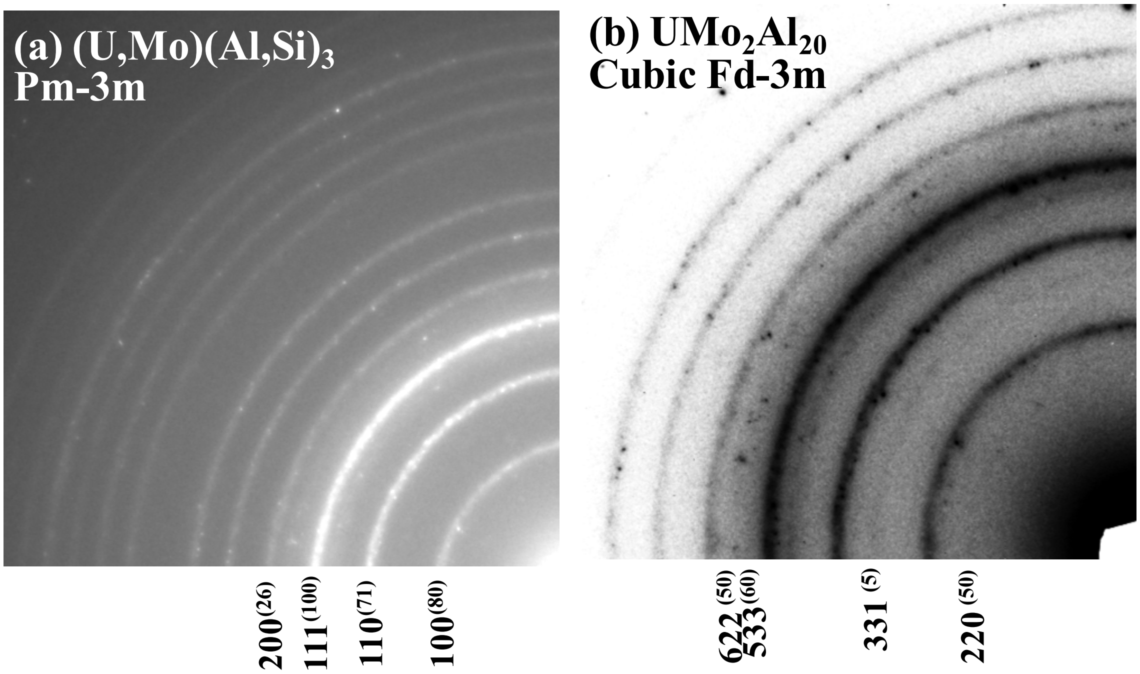

Figure 48. (a) SAED pattern corresponding to the (U,Mo)(Al,Si)$_3$ phase. (b) SAED pattern for the UMo$_2$Al$_{20}$ phase in the interdiffusion zone.

The $U_6Mo_4Al_{43}$ phase was identified in this couple near the Al/interdiffusion zone within the selected region shown in the HAADF micrograph in Figure 49(a), and in the bright field micrograph of the same region in Figure 49(b). Figure 49(c) shows the SAED pattern where the phase was discerned. The region corresponds to the dark phase region in Figure 46 (a) near the Al/interdiffusion zone interface. XEDS showed that this region was enriched with Al relative to the average composition of the interdiffusion zone, and contained very little Si.

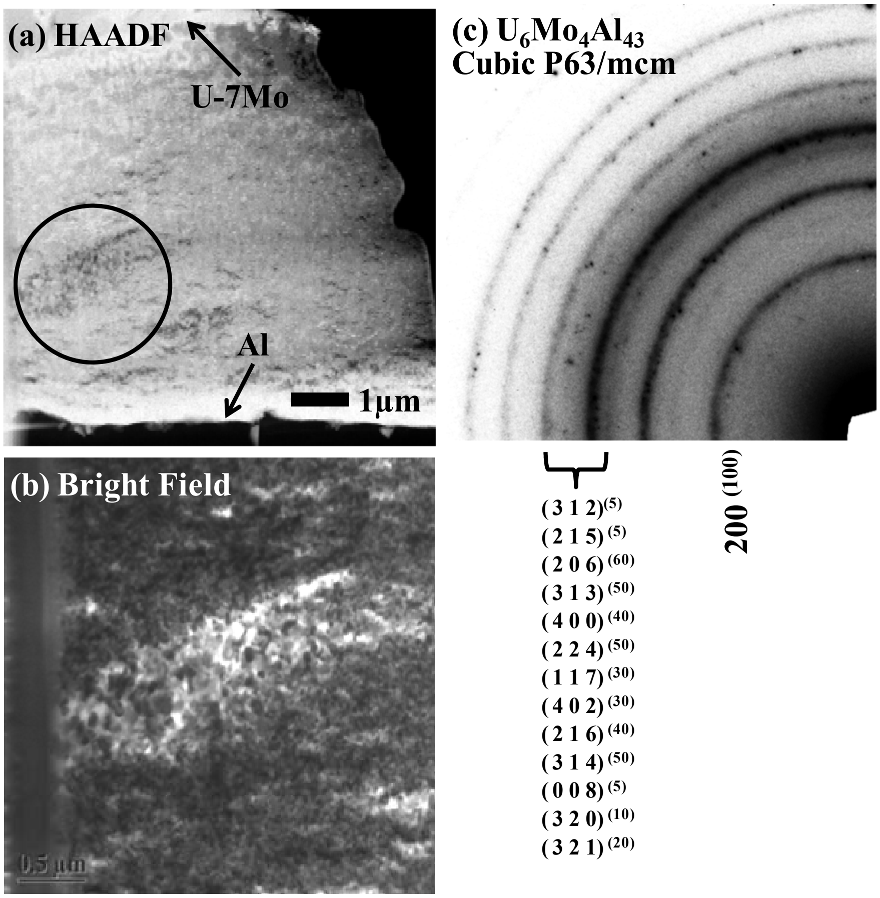

Figure 49. (a) Bright field micrograph of the selected region for analysis. (b) HAAFD micrograph of the complete interdiffusion zone for the U-7Mo vs. Al-2Si annealed for 1 hour showing the details of where the (c) SAED pattern corresponding to the as $U_6Mo_4Al_{43}$ phase was collected.

In order to determine the effect of Si concentration on the microstructural evolution of the interdiffusion zone, the U-7Mo vs. Al-5Si diffusion couple annealed for 5 hours at 550°C was also examined by TEM. Figure 50(a) shows a HAAFD micrograph of the entire interdiffusion zone for the U-7Mo vs. Al-5Si couple. Figure 50(b) shows a detailed bright field micrograph presenting a very fine grained microstructure very similar to that observed in the U-7Mo vs. Al-2Si diffusion couple annealed for 1 hour. Figure 51(a) shows a wide area electron diffraction pattern of the interdiffusion zone showing that the UAl_3 phase is present in the interdiffusion zone. The phase composition was also written as $(U,Mo)(Al,Si)_3$ to account for the same apparent solid solubility of the elements in this phase. The presence of the UMo_2Al_{20} phase was confirmed through grain specific electron diffraction analysis. Figure 51(b-d) show SAED patterns for a single grain of the UMo_2Al_{20} phase observed.

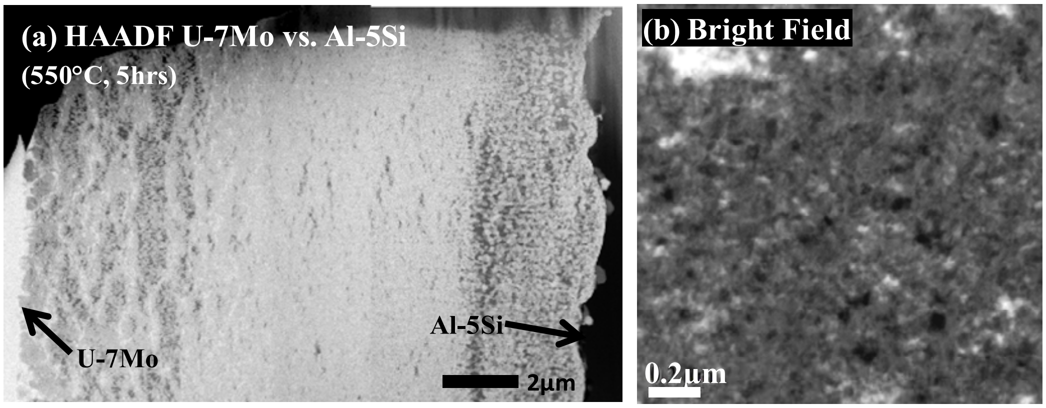

Figure 50. (a) HAAFD micrograph of the complete interdiffusion zone for the U-7Mo vs. Al-5Si annealed for 5 hours. (b) A detailed bright field micrograph.

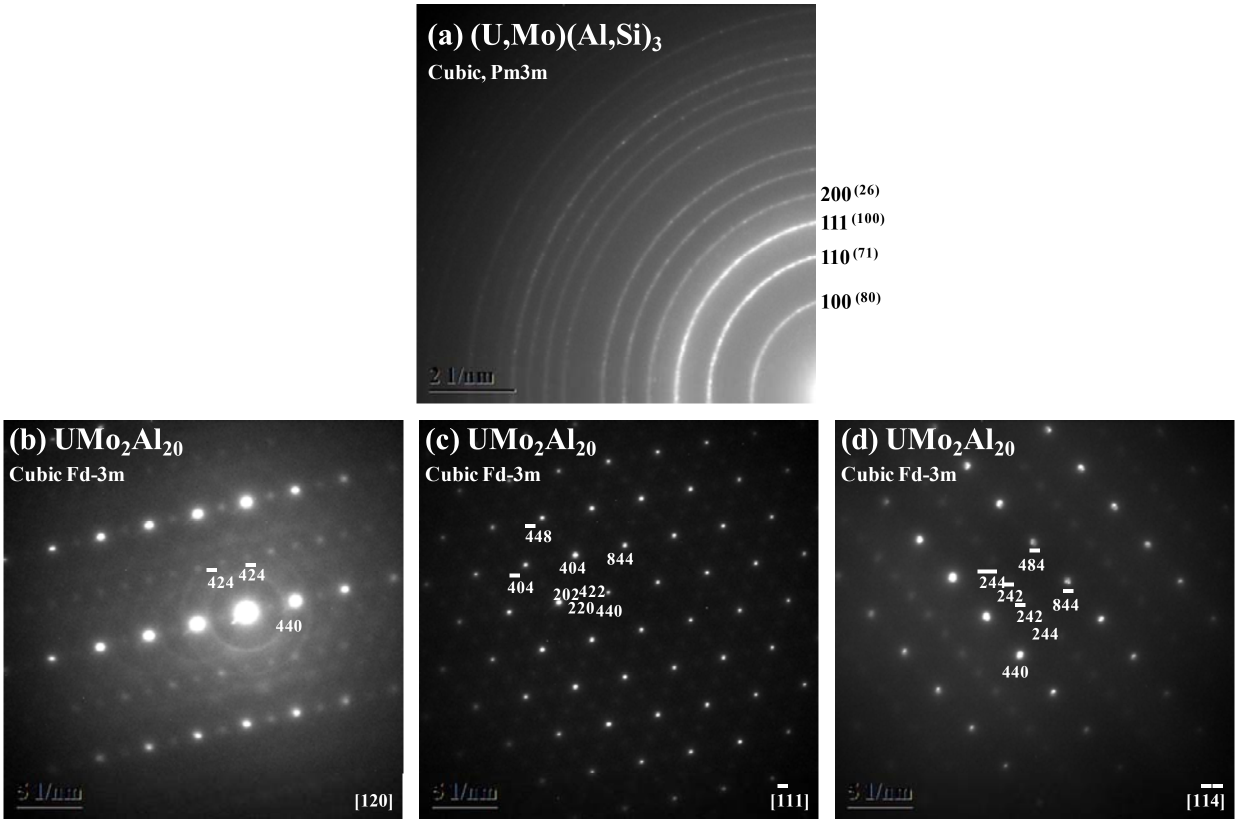

Figure 51. (a) SAED pattern corresponding to the as (U,Mo)(Al,Si)$_3$ phase. (b) Selected patterns for the observed UMo$_2$Al$_{20}$ phase in the interdiffusion zone.

Similar to the case of the U-7Mo vs. Al-2Si diffusion couple, the U$_6$Mo$_4$Al$_{43}$ phase was detected in the interdiffusion zone near the Al/interdiffusion zone interface through faint rings in the SAED patterns. In both diffusion couples, the U$_6$Mo$_4$Al$_{43}$ phase was found only in the dark phase-contrast regions in the micrographs in Figure 46(a) and Figure 49(a), but was not observed near the center of the interdiffusion zones where the Si concentration was higher, or near the U-Mo/interdiffusion zone interface. These results showed that in diffusion couples of U-7Mo vs. Al-2Si and Al-5Si, a three-phase region containing the (U,Mo)(Al,Si)$_3$, U$_6$Mo$_4$Al$_{43}$ and UMo$_2$Al$_{20}$ phases developed near the Al/interdiffusion zone interface. The other two phase regions observed in Figure 46(a) were composed of two-phase regions with higher Si content and the (U,Mo)(Al,Si)$_3$ and UMo$_2$Al$_{20}$ phases.

Although layered morphologies developed in the diffusion couples when Si was introduced to the Al, the periodic layer formation observed in the U-Mo vs. pure Al diffusion couples was not observed in any diffusion couple containing Si in this study. Periodic layer development appears to require stress accumulation within the interdiffusion zone so that the bands can develop. Their disappearance with the introduction of Si may mark a reduction of the internal residual stresses in the interdiffusion zone after phase evolution.

5. DISCUSSION

5.1 Cast 85.7Al-11.44U-2.86Mo and 87.5Al-10U-2.5Mo Alloys

Interactions between U-Mo and Al alloys have been shown to produce Al-rich binary and ternary compounds. The UAl_3, UAl_4, $U_6Mo_4Al_{43}$ and UMo_2Al_{20} phases have been identified in the literature [14, 17-24, 26, 27, 29, 32] and the possibility of other unidentified Al-rich phases has also been reported [9, 33]. In order to clarify and supplement the data on the Al-rich side of the U-Mo-Al system, and to determine if any unidentified phases remained to be discovered , the Al-rich portion of the U-Mo-Al ternary phase diagram at 500°C, shown in Figure 52, was constructed from the binary phase diagrams including ternary phases previously reported. The results of this study, discussed below, are compared to the literature [34] to confirm the Al-rich side of the ternary phase diagram.

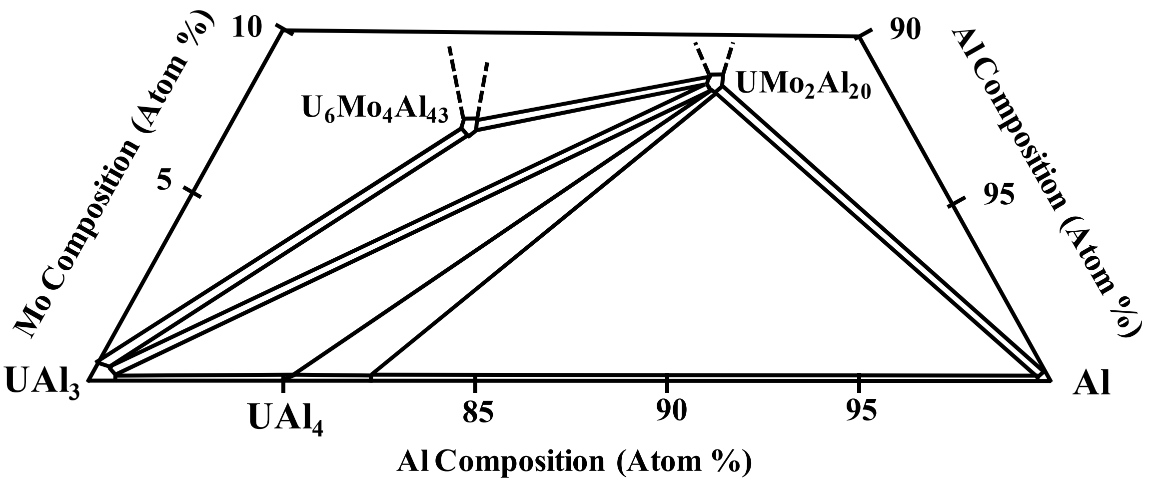

Figure 52. Al-rich portion of the U-Mo-Al ternary phase diagram at 500°C.

The 85.7Al-11.44U-2.86Mo and 87.5Al-10U-2.5Mo alloy compositions were selected and produced based on the compositions of the Al-rich layer observed during diffusional interaction in U-Mo dispersion/monolithic fuels with Al-alloy matrix. The different phases reported in these studies at or near 500°C are expected to have developed in the alloys examined in this study. Five and four phases were observed in 85.7Al-11.44U-2.86Mo and 87.5Al-10U-2.5Mo alloys, respectively. According to Gibb's phase rule, only three-phases are allowed under isothermal equilibrium condition for ternary alloys. The presence of extra phases indicates that these alloys did not achieve equilibrium, despite the homogenization at 500°C for 200 hours.

According to the U-Al binary phase diagram [33], and assuming for a moment that Mo, the minor alloying element in the system, does not play a significant role in the solidification path, the 85.7Al-11.44U-2.86Mo alloy would solidify via formation of first UAl_2, followed by UAl_3 and then (UAl_4+Al) phases at 500°C. The 87.5Al-10U-2.5Mo alloy would solidify via formation of UAl_3, and then (UAl_4+Al) phases only. Upon annealing, the phase constituents of these alloys would evolve towards equilibrium containing only the UAl_4 and Al-solid solution phases. This study did not observe the UAl_2 phase, and found a very small amount of UAl_3 phase locally in the 85.7Al-11.44U-2.86Mo alloy only. The presence of UAl_3 phase is then most likely a result of incomplete homogenization and/or microsegregation. Therefore, based on the U-Al binary phase diagram, and the amount of fcc-Al and UAl_4 phases observed, this study determined that the fcc-Al and UAl_4 phases are two equilibrium phases in the 87.5Al-10U-2.5Mo and 85.7Al-11.44U-2.86Mo alloys.

The $U_6Mo_4Al_{43}$ and UMo_2Al_{20} phases observed in both alloys are the result of Mo additions into the U-Al system. Figure 11 and Figure 12 show that the $U_6Mo_4Al_{43}$ is generally surrounded by UMo_2Al_{20}. In agreement with this study, F. Mazaudier et. al noted that the UAl_4 and $U_6Mo_4Al_{43}$ phases never coexisted in diffusion couples of U-Mo vs. Al alloys. On Figure 13, the phases come into contact in the presence of the UAl_3 phase; this is expected to be an artifact of remaining inhomogeneity in the casting.

The development of the UAl_3 and UAl_4 phases in the alloys requires that Mo be rejected from these two Mo-depleted phases to produce a Mo enriched phase. The UMo_2Al_{20} phase is slightly higher in Al and Mo content than the $U_6Mo_4Al_{43}$. Thus, based on sufficient Al content, presence of Mo, and microstructure of the alloys, that the UMo_2Al_{20} phase is likely the third equilibrium phase for the alloys examined in this study.

In agreement with the results of Palancher et. al [56], Table 1 reports that all measured compositions of the phases in the alloys had little variation. The solubility limits for the elements in the phases were not accurately determined, but the phases observed in these alloys have well defined compositions with little variation. Although the UAl_3 phase may not be an equilibrium phase in these alloys, both the UAl_3 and UAl_4 phases showed little or no solubility for Mo.

Other previously unidentified phases were not observed in the two alloys examined. Previous studies [9, 19-24] reported the probability of unidentified Al-rich phases within the multi-phase interdiffusion layers. The Al-rich phases observed in the diffusion couple experiments carried out at or near 500°C may contain various mixture of cubic-UAl_3, orthorhombic-UAl_4, hexagonal-

$U_6Mo_4Al_{43}$ and diamond cubic-UMo_2Al_{20} phases, depending on diffusion path (e.g., composition path) as a function of terminal alloy compositions. Other unknown phases are not expected to develop in diffusion couples or in out-of-pile dispersion/monolithic fuel experiments of similar composition.

In the ternary isothermal phase diagram, the 85.7Al-11.44U-2.86Mo and 87.5Al-10U-2.5Mo alloys should lie in a three-phase region composed of Al solid solution, UAl_4 and UMo_2Al_{20} phases, as shown in Figure 52. The ternary isothermal phase diagram shown in Figure 52 was drawn from the results of this study and data in the literature. It is in very good agreement with the one proposed by F. Mazaudier et. al. [57], with the exception that the solubility limits of the two and three-phase regions are reduced based on the EDS results in Table I, that show little variation in compositions of the phases. The accuracy of the EDS data collection may contain some error based on the nature of the process, but the EDS precision can be used to, at least, qualitatively measure compositional variations within a given phase.

5.2 Cast 19U-69Al-12Si and 22U-3Mo-56Al-19Si (at.%) Alloys Characterization

In this study, and commonly in the literature [4-42], interactions between U-Mo and Al alloys have been shown to produce microstructures containing the UAl_3, UAl_4, $U_6Mo_4Al_{43}$ and UMo_2Al_{20} phases in diffusion couples and cast alloy experiments. The ternary $U_6Mo_4Al_{43}$ phase has been shown to result in deleterious behavior under irradiation experiments [36-42]. In diffusion couples of U-Mo vs. Al, the UAl_2 phase has not been typically observed; the binary UAl_4 phase develops only near the Al parent alloy [56,57,59]. The UAl_3 phase, on the other hand, has been typically observed distributed through the majority of the interdiffusion zone thickness [54,59,87] indicating that this phase may significantly affect the microstructural development in the interdiffusion zones.

The introduction of Si into the system in diffusion experiments of U-Mo vs. Al-Si, showed that significant changes to the phase development could be accomplished [78-87]. The microstructures of diffusion couples of U-Mo vs. Al-Si alloys developed layered microstructures containing the mainly the (U,Mo)(Al,Si)$_3$ and UMo$_2$Al$_{20}$ phases as the main components in their microstructures, where the (U,Mo)(Al,Si)$_3$ phase has the UAl$_3$ crystal structure with Mo and Si solid solubility. Under irradiation experiments [63,88], the interdiffusion zones with U-Mo/Al-Si in dispersion fuels developed acceptable microstructures resistant to the typical deleterious effects observed in U-Mo/Al systems.

In order to develop a better understanding of the phase development in the interaction regions from U-Mo vs. Al-Si diffusion couples, two cast alloy compositions, 22U-3Mo-56Al-19Si and 19U-69Al-12Si (at.%), were prepared with bulk compositions chosen to be similar to the average compositions of the interdiffusion zones in diffusion couples. The 19U-69Al-12Si was considered to determine the effects of Si additions to the binary U-Al system. The 22U-3Mo-56Al-19Si composition was considered in order to attempt to obtain similar phase development as typically observed in U-Mo vs. Al-Si diffusion experiments, and to examine the effects of Mo.

Based on the Al- rich side of the binary U-Al [106] phase diagram shown in Figure 53 (a), at 550°C, the UAl$_2$, UAl$_3$ and UAl$_4$ phases may be expected to develop in an alloy depending on its

Al concentration, and the U and Al solid solutions have negligible solubility. All observed phases at this temperature have strict compositions, where Al enrichment or depletion resulted in phase transformations rather than solid solutioning. Furthermore, based on the melting point of each phase, the thermodynamic stability of the phases can be qualitatively described as decreasing with increasing Al concentration.

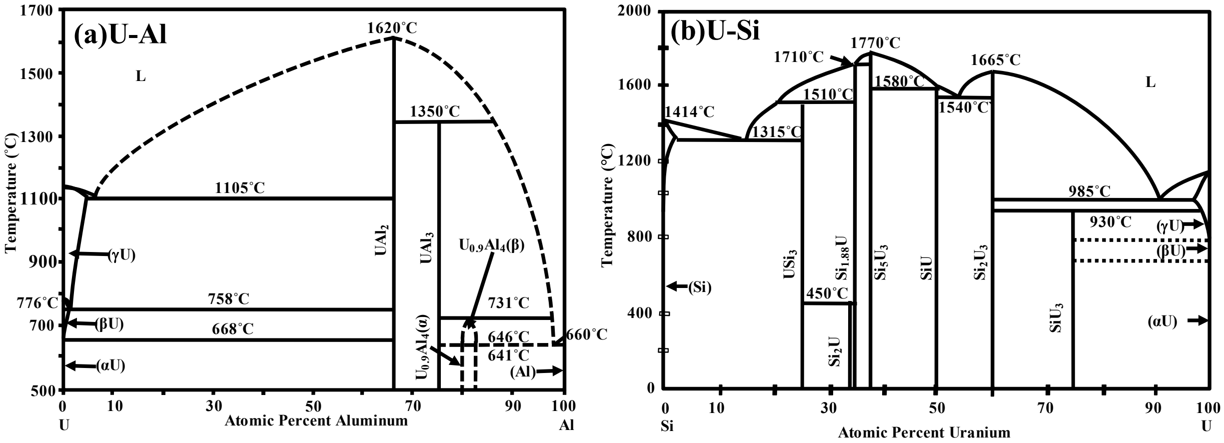

Figure 53. Equilibrium binary phase diagrams of (a) U-Al [106] and (b) U-Si [107].

The U-Si phase diagram shows a number of phases that have not typically been observed in the interdiffusion zones of U-Mo vs. Al-Si diffusion couples. The presence of Al appears to stabilize the USi_3 phase composition within the interdiffusion zone, probably because of its similarities to the UAl_3 phase. In the binary U-Si phase diagram, shown in Figure 53 (b) [107], the USi_3 phase develops with the same crystal structure [110] as the UAl_3 phase, Pm-3m (cP4, $AuCu_3$) where Al substitutes for Si. The UAl_3 and USi_3 phases have lattice parameters of 0.4263 and 0.403 nm respectively. Full solubility, with each other, of these phases may be expected. Dwight et. al [78] examined the phase equilibria on the U-Al-Si system and found full solubility between UAl_3 and USi_3 phases at 900°C, and reported that a miscibility gap may exist at lower temperatures, but did not record the transition temperature. The 19U-69Al-12Si alloy developed an Al-rich $U(Al,Si)_3$ composition, shown in Table 4.3.II. According to the XEDS data, all of the Si was found in solution within the $U(Al,Si)_3$ phase. The limited Si concentration in the cast alloy limited its concentration in the phase. Introduction of Si into the UAl_3 phase resulted in a decrease of the lattice parameter of the phase, as shown in Table 4.2.III.

The 22U-3Mo-56Al-19Si alloy, showed similar behavior to the 19U-69Al-12Si alloy in that a phase with the crystal structure of the UAl_3 phase developed. The phase composition in this case included Si and Mo solubility to develop the $(U,Mo)(Al,Si)_3$ phase composition. Again, in this case, due to the limited concentrations of Mo and Si in the cast alloy, the $(U,Mo)(Al,Si)_3$ phase contained limited amounts of these elements. The introduction of Si into the UAl_3 appears to open solubility for Mo into this phase. Additionally, however, this alloy developed the UMo_2Al_{20} phase which served as an additional Mo sink. An important result of the 22U-3Mo-56Al-19Si alloy is that the $U_6Mo_4Al_{43}$ phase typically observed in the U-Mo-Al system was not observed. The introduction of Si appears to have prevented the development of this phase in the microstructure of the alloy. The intermediate phase reactions by which the $U_6Mo_4Al_{43}$ and UMo_2Al_{20} phases develop were not considered in detail in this study, but the development of sub-lattice structures (polyhedron icosahedra) appears to be a pre-requisite for phase development. It is suspected that the introduction of Si into the U-Mo-Al system interrupts one or more intermediate reactions, preventing $U_6Mo_4Al_{43}$ phase development without affecting the development of the UMo_2Al_{20} phase. Jeitschko and Niemann [95,97,98] performed a detailed study on the crystal structures of the $U_6Mo_4Al_{43}$ and UMo_2Al_{20}, and showed that these phases develop with icosahedra structures that occupy the lattice positions. He showed that the

$U_6Mo_4Al_{43}$ phase developed ten different icosahedra substructures while the UMo_2Al_{20} develops five; two icosahedra are common to both structures. The development of the $U_6Mo_4Al_{43}$ phase can be retarded if the development of any of the eight remaining icosahedra structures is interrupted.

5.3 Diffusion couples U-Mo vs. Pure Al annealed at 600°C for 24 hours

A diffusion study in the U-Mo-Al system was undertaken using solid-to-solid diffusion couples characterized by SEM, EPMA and TEM in order to develop a better understanding of the interactions between U-Mo alloys and pure Al. There have been some disagreements in regards to the constituent phases that developed during interdiffusion between U-Mo and Al. The discrepancy in phase constituents, in general, originates from: (1) use of Al alloys with trace element additions, (2) identification of phases that contain Mo, (3) slight differences in sample preparation, oxides or nitride contamination, and temperature differences in diffusion anneals. These variations can alter the decomposition rates of U-Mo alloys, and can modify the overall thermodynamics and/or kinetics.

Based on bulk analysis by SEM, EPMA and XRD, Lee *et* al. [50] and Kim *et* al. [33] reported the presence of the UAl_3, and decomposition of γ-U to α-U and U_2Mo phases in U-Mo dispersion fuel in Al matrix after annealing at 400°C. Lee *et* al. [31] observed, by neutron diffraction, the UAl_2 and UAl_3 phases as the product of interdiffusion, along with $\gamma \rightarrow (\alpha + U_2Mo)$ transformation. Mirandou *et* al. [55], based on bulk analysis of diffusion couples annealed at 580°C, reported the $(U,Mo)Al_3$ and $(U,Mo)Al_4$ phase compositions, to allow for Mo solubility into the binary phases. More importantly, the presence of $U_6Mo_4Al_{43}$ and UMo_2Al_{20} phases in the interdiffusion zone was documented based on XRD. Palancher *et* al. [56] and Mazaudier *et* al. [57] determined that the binary UAl_3 and UAl_4 phases had little or no solubilities for Mo, supporting the formation of ternary $U_6Mo_4Al_{43}$ and UMo_2Al_{20} phases during interactions between U-Mo and Al. Parallel studies conducted on Al-rich cast U-Mo-Al alloys, by Keiser *et* al. [60], Noël *et* al. [61] and Perez *et* al. [62] further confirmed the presence of the ternary intermetallic phases and their limited solubility for Mo in binary UAl_3 and UAl_4 phases. Results by TEM from the current study on individual grains confirmed the presence of binary UAl_3 and UAl_4 phases with limited solubility for Mo, the ternary $U_6Mo_4Al_{43}$ and UMo_2Al_{20} phases and documented their distributions within the interdiffusion zones between U-Mo and Al.

The measured concentration profiles of each couple indicated that the three diffusion couples maintained an average composition of nearly 80 at.% Al throughout the thickness of the interdiffusion zones. Because the interdiffusion zones contained very fine microstructures with varying phase mixtures, each data point represented the average composition of the phases within the interaction volume of the electron beam. Characterization by TEM determined that the UAl_3, UAl_4, $U_6Mo_4Al_{43}$ and UMo_2Al_{20} phases were the phases present within the interdiffusion zones of diffusion couples of U-7Mo, U-10Mo and U-12Mo vs. pure Al at 600°C. These phases were found in two- and three-phase regions that developed into layered microstructures. The layers developed transverse to the direction of diffusion flux. Figure 26, Figure 27 and Figure 28 show the morphological changes observed in the U-7Mo, U-10Mo and U-12Mo vs. Al diffusion couples, respectively.

The UAl_3, UAl_4, $U_6Mo_4Al_{43}$ and UMo_2Al_{20} phases were identified by analytical TEM in a parallel study on Al-rich U-Mo-Al cast alloys with compositions chosen near to the typical average composition of the interaction regions between U-Mo and Al [62] as presented in section 4.1 and 5.1 of this document. The study added to the data on the ternary U-Mo-Al phase diagram at 500°C, and confirmed the low solid solubilities of the phases: Figure 52 shows the ternary U-Mo-Al phase diagram generated by combining the data in the study in combination with the ternary diagram proposed by Mazaudier et al. [57]. In the current study, the phases were identified from the U-10Mo vs. Al diffusion couple annealed at 600°C for 24 hours. Figure 54 presents schematic diagrams illustrating the phase constituents of all three diffusion couples examined in this study. Figure 54 (b) shows a schematic of the observed interdiffusion zone in the U-10Mo vs. Al diffusion couple, and shows that in this couple some of the layers anticipated by the phase diagram were not observed. The morphological changes observed in the backscatter electron micrographs were in good agreement with the phase distributions observed by TEM analysis. This indicated that the morphological changes within the interdiffusion zone indeed marked variations in the phase distributions of each interdiffusion zone.

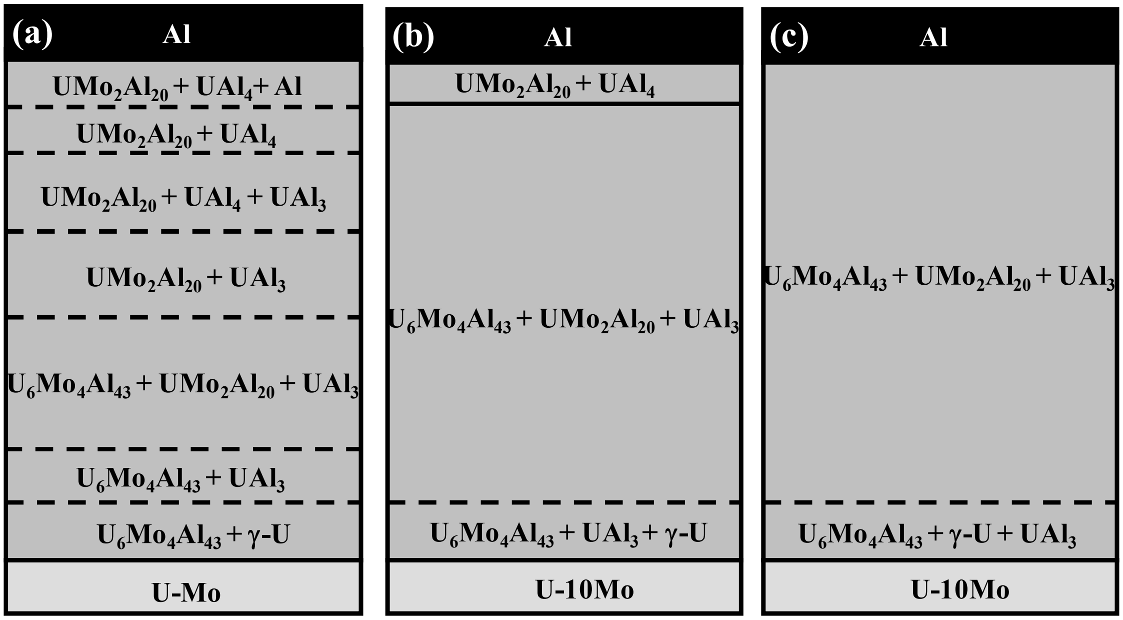

Figure 54. Schematic summary of phase constituent in the interaction layer developed in the (a) U-7Mo vs. Al, (b) U-10Mo vs. Al and (c) U-12Mo vs. Al diffusion couples annealed at 600°C for 24 hours.

The phase distributions of the U-7Mo and U-12Mo vs. Al diffusion couples were then projected based on the observed layered morphology, the diffusion paths generated from the concentration profiles, and the phase diagram in Figure 52. Figure 54(a) and Figure 54(c) present schematic diagrams of the interdiffusion zones of the U-7Mo vs. Al and U-12Mo vs. Al diffusion couples illustrating the plausible layered phase distributions in each couple. Based on the observed layered morphology of the interdiffusion zone, the U-7Mo vs. Al diffusion couple appears to have developed all the phase regions predicted by the phase diagram. Increased Mo concentration in the parent U-Mo alloy resulted in less layering with preference for increased thickness, relative to the overall interdiffusion zone thickness, of the three phase layer containing the UAl_3, $U_6Mo_4Al_{43}$ and UMo_2Al_{20} phases.

Mirandou *et* al. [55,58], Palancher *et* al. [56], Mazaudier *et* al. [57], Ryu *et* al. [51,52] and Perez *et* al. [59] have reported layered microstructures in the interdiffusion zones between U-Mo and Al based on backscatter electron imaging contrast, XRD, and μ-XRD. In the current study the phase volume fractions in the interdiffusion zone were measured from backscatter electron images based on phase contrast and area fractions. The phase fractions were then estimated through mass-balance using the phases' stoichiometric compositions (assuming zero solubility) and the measured average composition of the region under consideration. The measured and calculated values were found to be in good agreement. The three-phase regions containing (UAl_3 + $U_6Mo_4Al_{43}$ + UMo_2Al_{20}) on each diffusion couple accommodated the stoichiometric compositions of the different phases well within the measured composition of the region: for example, in the U-10Mo vs. Al diffusion couple, the phase fractions of the UAl_3 with $U_6Mo_4Al_{43}$ and UMo_2Al_{20} were found to be 41%, 14% and 44% respectively, and were in agreement with the area fractions from Figure 27(c-e). In the same couple, the binary phase region that consisted of UAl_3 + $U_6Mo_4Al_{43}$ near to the U-Mo alloy required wide solid solubility of Mo into the phases in order to accommodate the measured Mo content. This two-phase layer may be supersaturated with Mo, and suggests that Mo may be intrinsically diffusing faster than U. The average composition within the UAl_4 + UMo_2Al_{20} two-phase layer next to Al could not be measured by EPMA because of its limited thickness. Nonetheless, Al enrichment is obvious from the observed phase development.

Based on experimental results and the aforementioned simple analysis, there appear to be deviations from the assumption of local thermodynamic equilibrium, under constant temperature and pressure, employed for understanding classical ternary diffusion, as evidenced by supersaturated Mo-content in a two-phase layer and the presence of three-phase layers with any thickness, based on the available thermodynamic degrees of freedom.

U-Mo and Al interactions have been shown to result in significant volumetric expansion of the interdiffusion zone. D.B. Lee et al. [45] examined these effects on U-2 wt.% Mo and U-10 wt.% Mo dispersions in Al. The expansion is a direct result of the larger molar volume of the developed phases. The molar volume of U, Al, UAl_3, UAl_4, $U_6Mo_4Al_{43}$ and UMo_2Al_{20} phases are 14.08, 10.03, 46.75, 56.80, 554.49, 229.74 cm^3 per mole, respectively [93,94], and the average volumes per atom in each phase are 2.33×10^{-23}, 1.66×10^{-23}, 7.76×10^{-23}, 9.43×10^{-23}, 9.21×10^{-22} and 3.81×10^{-22} cm^3 per atom, respectively. As the phases develop and grow, stress accumulation takes place within the interdiffusion zone due to the molar volume differences between the phases and the parent alloys. The stress results in fracturing and bulk deformation of the parent U-Mo and Al in order to accommodate the interaction region. Figure 24 shows the presence of cracks along the direction of interdiffusion flux observed within the interaction layers of the diffusion couples, and the figure shows that fracturing within the interaction layer was more frequent as the Mo content in the U-Mo alloy increased in the U-Mo alloy. Because of the low solid solubilities, higher Mo-content within the U-Mo alloys resulted in higher volume fractions of the $U_6Mo_4Al_{43}$ and UMo_2Al_{20}, indicating that higher concentrations of these intermetallic phases increased the brittleness of the interdiffusion zone. Because increased lattice mismatch between two phases typically decreases ductility of a given material [96], an increase in brittle behavior may at least in part result from the increased stresses between the interphase boundaries of different phases. However, due to the conditions of this experiment, fracturing could have taken place during quenching.

Although the assumption of local thermodynamic equilibrium for diffusion at constant temperature and pressure does not allow for the presence of three-phase layers in a ternary system, these regions have been well documented in the U-Mo-Al system. Although the system may heavily deviate from equilibrium to develop the given microstructure, it is more likely that an additional thermodynamic degree comes into play to restore or maintain a near equilibrium condition. In the U-Mo-Al system, internal stresses within the interdiffusion zone can introduce the additional thermodynamic degree of freedom necessary to allow for the observed solid solubilities in the two phase regions, and for the three phase regions to grow (layer thickness >0) without large deviations from thermodynamic equilibrium.

The interdiffusion zones in each couple divided into layered microstructures where each layer evolved according to the local composition of the interdiffusion zone where the layers were observed. The phase distributions were explained by the diffusion path from the concentration profiles plotted in the ternary U-Mo-Al phase diagram. Within the (UAl_3 + $U_6Mo_4Al_{43}$ + UMo_2Al_{20}) layer, sub-layering of this region was observed with the development of periodic bands near the (UAl_3 + $U_6Mo_4Al_{43}$ + UMo_2Al_{20}) to (UAl_3 + $U_6Mo_4Al_{43}$ + UMo_2Al_{20}) transition region. The development of periodic layers, or bands, within the interdiffusion zone may suggest that a mechanism analogous to Liesegang band formation in gels, but observed in ternary and higher order solid interactions may play a role. The development of periodic bands in the interaction layers has been observed in the interdiffusion zones of some alloy systems. V.A. Van Rooijen et al. [99] observed them in oxidized alloys. K. Osinski et al. [100] observed periodic pattern formation in Fe-Si vs. Zn diffusion couples. The group of M.R. Rijnders et al. [101,102]

and A.A. Kodenstov [103] et al. observed similar results in Fe_3Si, Co_2Si and Ni_3Si_2 vs. Zn, in $Ni_{50}Co_{20}Fe_{30}$ vs. Mg, and in SiC vs. Pt diffusion couples. X. Su [104] also considered the Ni_3Si_2 vs. Zn and reached similar conclusions as M.R. Rijnders and A.A. Kodenstov. Their justification for the development of the periodic layers appears to be well justified for their systems, where the development of periodic layers in the interdiffusion zone stems from large differences in mobility of the elements in conjunction with the creation and diffusion of vacancies, and from the phase development at the substrate/interdiffusion zone interface of the substrate with the lower mobility elements that results in internal stress accumulation at this location. In their systems, secondary phases develop at the interface as the elements diffuse to saturate the region. As the secondary phases evolve at this interface, stress develops. The layer grows attached to the interface until a critical stress is reached. In order to relieve the stress, the layer detaches from the interface. After detachment, re-saturation of the region takes place, repeating the process.

In diffusion couples of U-Mo vs. Al, periodic layer development did not take place near the terminal alloy interfaces with the interdiffusion zone. Additionally, periodic banding was only observed in the U-7Mo and U-10Mo vs. Al diffusion couples. Although layered microstructures were observed throughout the interdiffusion zones in the couples, periodicity was observed only as a sub-layer near the center of the interdiffusion zone phase region away from the parent alloy interfaces. As a result, the mechanism of layer formation presented by K. Osinski, M.R. Rijnders, A.A. Kodenstov and X. Su does not seem to fully apply.

Because periodic layer development took place away from the parent alloy interfaces, local supersaturation of the elements must have taken place at some region within the interdiffusion zone, away from the parent alloys. The periodic layers started and increased in distance from a given region in the interdiffusion zone, as shown in Figure 27 (d) for the U-10Mo vs. Al couple. A qualitative description of the model by C.Wagner [105] provides an acceptable partial explanation for the phase development in the U-Mo vs. Al system: a high mobility species, Al, in the diffusion couple diffuses and rapidly saturates the interaction region, producing a fast moving diffusion front in one direction. Species with lower mobility do not have enough time to interact as they diffuse in the opposite direction, and they saturate a localized region of the interdiffusion zone. Only when a critical concentration above a supersaturation point is reached does a layer develop, resulting in localized equilibrium phase transformations.

In the U-Mo-Al system, phase transformations result in the development of the ternary $U_6Mo_4Al_{43}$ and UMo_2Al_{20} phases with large molar volume differences from the surrounding phases. According to K. Osinski [100], M.R. Rijnders [101,102] A.A. Kodenstov [103] and X. Su [104], the development of a given periodic layer requires localized evolution of stress at the location where the band develops, which in their cases, is always at the interface with one of the parent alloys. As stress accumulates, the developed band remains stationary, and the interface moves away further into the parent alloy to relieve the stresses, a supersaturated region develops and the process repeats. In the U-Mo-Al interdiffusion zone, the development of the $U_6Mo_4Al_{43}$ phase precedes that of the UMo_2Al_{20} phase: in the interdiffusion zone, the UAl_3 + $U_6Mo_4Al_{43}$ two-phase region near the U-Mo alloy develops first as the diffusion front penetrates the U-Mo alloy. As the concentration of the $U_6Mo_4Al_{43}$ phase increases, stress accumulates in this region. At a critical concentration of the $U_6Mo_4Al_{43}$ phase, the stresses appear to be significant enough to allow for the opening of a degree of freedom, as discussed above, and then with some enrichment and a crystallographic re-orientation the phase transforms to the UMo_2Al_{20} phase [95,97,98]. Because the $U_6Mo_4Al_{43} \rightarrow UMo_2Al_{20}$ phase transformation involves a reduction in molar volume, stress is relieved from the local region. When local three-phase equilibrium is achieved, growth of the interdiffusion zone resumes and it grows until stresses accumulate and the process repeats.

In this study, the U-7Mo and U-10Mo vs. Al diffusion couples developed well defined periodic bands in the UAl_3 + $U_6Mo_4Al_{43}$+ UMo_2Al_{20} phase region near to the transition to the UAl_3 + $U_6Mo_4Al_{43}$ two-phase region. The U-12Mo vs. Al transitioned the same phase region without periodic layer development. In other parallel studies [54,59], the similar behavior was observed with diffusion couples of the same compositions but with different anneal conditions, indicating that periodic bands are common in this system at different temperatures and compositions.

Periodic layer formation appears to require that the diffusing species have large differences in mobility. The presence of periodic bands was used as an indicator that the U, Mo and Al had significantly different mobility in the interdiffusion zone. Based on the microstructures developed by K. Osinski [100], M.R. Rijnders [101,102], A.A. Kodenstov [103] and X. Su [104], periodic bands always increase in distance proportionally to distance from the fast diffusing species. Thus, the fast diffuser could be and was identified from the periodic layered morphology: for the case of the U-Mo vs. Al diffusion couples, the interdiffusion zone morphologies indicated that Al was the fast diffusing species.

Interface diffusion should play an important role during interdiffusion between U-Mo and Al at 600°C. The microstructure observed by TEM in this study was, in general, extremely fine. Because grain boundary density is inversely proportional to grain size, and the typical grain size within the interdiffusion zone was in the range of 100nm, grain boundary density within the interdiffusion zone was very high. The elongated phase regions detailed in Figure 35 supported that the observed fine-scaled grains were present during isothermal anneal and that that they were not a product of quenching. These microstructures more importantly supported that grain boundary diffusion may have played a role in the evolution of the interdiffusion zone. Grain boundary diffusion supported the requirement that Al has high mobility in order to develop periodic bands. The U and Mo showed lower mobility than Al in the interdiffusion zone. Nonetheless, supersaturation of Mo near the U-Mo/interdiffusion zone interface indicated that Mo had a higher mobility than U.

The relevance of interphase boundary diffusion was further supported by the large difference in melting point compared to the diffusion anneal temperature. Melting points of 1510°C, 731°C, 1360°C and 1200°C [61] for the UAl_3, UAl_4, $U_6Mo_4Al_{43}$ and UMo_2Al_{20} phases, respectively indicate that, with the exception of the UAl_4 phase which was only observed very near the Al/interdiffusion zone interface, the anneal temperature of the diffusion couple was below ½ the melting temperature of the phases. In general within this temperature regime, lattice diffusional interactions are normally less significant, and grain boundary diffusion typically dominates.

A thin layer, almost continuous for U-7Mo and discontinuous for U-12Mo, of α-U phase was observed within the U-Mo alloy next to the interdiffusion layer as presented in Figure 38. The transformation of γ-U to α-U strongly depends on the Mo concentration, time and temperature. The presence of the α-U phase in the studies by Lee *et* al. [50] and Kim *et* al. [64] was a result of $\gamma \rightarrow (\alpha + \delta)$ decomposition due to lower temperature anneals. However, in this study at 600°C, the $\gamma \rightarrow \alpha$ decomposition was not expected and can be better explained by the depletion of Mo from the γ-phase U-Mo alloy. The presence of α-U was observed within the U-Mo alloy only near the interface, and δ-U_2Mo was never observed. This indicated that there was local depletion of Mo near the interface. The development of periodic layers in the interdiffusion zone further supports further suggested that Mo had a higher mobility, and it diffused faster than U from the U-Mo alloy.

An important finding of this study with respect to the application of U-Mo metallic fuel in Al matrix is the presence of UAl_3, UAl_4, $U_6Mo_4Al_{43}$ and UMo_2Al_{20} phases. According to a TEM study by Gan *et* al. [63] of Kr-irradiated alloys (i.e., 500 keV Kr ions at 200°C) containing these phases, the $U_6Mo_4Al_{43}$ phase transforms to amorphous structure at less than 1 dpa and forms a high density of voids at 100 dpa. The UMo_2Al_{20} and UAl_3 phases become amorphous at 10 dpa and ~2 dpa, respectively, however, without significant void formation, even up to 100 dpa. The UAl_4 remains crystalline without void formation even at 100 dpa. The presence of these phases may be responsible for the formation of amorphous interaction layers after irradiation. The $U_6Mo_4Al_{43}$ phase may be particularly responsible for the detrimental behavior of the interdiffusion zone during irradiation. Deleterious behavior of in reactor applications includes amorphization, poor mechanical integrity and void formation during in-reactor irradiation [42, 43, 63-66].

The development of ternary intermetallic phases containing Mo, which may give rise to poor irradiation performance, is primarily due to limited solubility of UAl_3 and UAl_4 phases. In order to partition Mo into the more stable binary aluminide phases, solubility limit must be increased. Experimental evidence has shown [87,88] that introduction of Si into the Al reduces the thickness and changes the phase constituents of the interdiffusion layer. There is strong evidence of the absence of the $U_6Mo_4Al_{43}$ phase [87] in the interdiffusion layer due to the fact that UAl_3 phase can accommodate Mo as $(U,Mo)(Al,Si)_3$ with extended solubility, or the mechanism that results in the development of the $U_6Mo_4Al_{43}$ phase may be disrupted. The presence of Si may hamper the formation of polyhedra substructures [95,97] of $Mo(U_2Al_{10})$, $MoAl_{12}$ and/or $(Al,Mo)(U_3Al_9)$ that form the $U_6Mo_4Al_{43}$ phase by interacting with Mo directly (e.g., silicide formation).

The use of high purity metals in this study permitted discussion of the phase development strictly based on the thermodynamic degrees of freedom available in U-Mo vs. Al diffusion couples, and allowed for a clear explanation of how the observed microstructures develop in the interdiffusion zones. The use of low purity metals, or commercial alloys with a large number of trace element additions, allow for the introduction of any given number of degrees of freedom into the interdiffusion zone by increasing the number of components in the system. These degrees of freedom may be expressed in the interdiffusion zones through the development of unpredictable and undesired phases and/or other unforeseen behavior of the interdiffusion zone. Therefore, in order to better predict and control the evolution of the interdiffusion zones, high purity metals may be recommended in lieu of commercial materials.

With regards to fuel plate manufacture, limiting the degrees of freedom through control of the initial alloy compositions, can significantly improve control during plate assembly, by limiting undesired interactions before the fuel plates enter the reactor. During irradiation conditions, any undesired phases can produce unforeseen behavior that may prevent any reliable study of in-reactor behavior.

5.4 Diffusion couples U-Mo vs. Al and Al-Si alloys annealed at 500°C for 1, 5 and 20 hours

A series of diffusion couples containing U-7Mo, U-10Mo and U-12Mo vs. Al, Al-2Si and Al-5Si were annealed at 550°C in order to develop an understanding on the phase development and evolution with time and composition.

5.4.1 U-Mo vs. Al diffusion couples

Alloy interactions in diffusion couples containing U-Mo alloys in contact with Al at 600°C resulted in the development of multiphase interdiffusion zones containing very fine-grained mixtures of the UAl_3, UAl_4, $U_6Mo_4Al_{43}$ and UMo_2Al_{20} phases in two- and three-phase layered microstructures. The U-10Mo vs. Al diffusion couple annealed at 600°C for 24 hours was used to characterize the phase development in the interdiffusion zones. This couple developed a layer containing the (UAl_3 + $U_6Mo_4Al_{43}$ + UMo_2Al_{20}) phase mixture that dominated the majority of the interdiffusion zone thickness. The regions near the Al/interdiffusion-zone-interface and U-Mo/interdiffusion-zone-interface developed two-phase regions containing (UAl_4 + UMo_2Al_{20}) and (UAl_3 + $U_6Mo_4Al_{43}$), respectively. The layered morphology in these couples was partially explained, through the ternary U-Mo-Al phase diagram and the diffusion path followed by each couple. Based on average compositional analysis coupled with backscatter electron image contrast, the phase development of the U-Mo vs. Al system at 600°C and 550°C appears to follow similar paths. The stability of the UAl_3, $U_6Mo_4Al_{43}$ and UMo_2Al_{20} at 550°C have been confirmed by Mirandou et al. [55], Palancher et al. [56] and Mazaudier et al. [57] in diffusion couples, and by Perez et al. [62] at 500°C in Al-rich cast alloys. Because the average compositions agree and the observed phases are stable at low temperature, the phase development at 600°C and 550°C was assumed to be the same.

As in the diffusion couples annealed at 600°C, periodic layer development was also observed at 550°C within the interdiffusion zones as a sub-section of the (UAl_3 + $U_6Mo_4Al_{43}$ + UMo_2Al_{20}) three-phase layer. The development of periodicity indicated that stress accumulation took place in the interdiffusion zones: periodic layer development appears to take place only when internal stresses are present within the interdiffusion zone. Bands develop as a result of localized supersaturation, stress accumulation and stress accommodation. The region where periodic layering was observed in the diffusion couples annealed at 600°C marked the position in the interdiffusion zone where the UMo_2Al_{20} phase appears to have initially developed. The phase developed from the $U_6Mo_4Al_{43} \rightarrow UMo_2Al_{20}$ phase transformation and allowed for the relief of some stress from the interdiffusion zone by volumetric reduction of the interaction region due to the lower molar volume of the UMo_2Al_{20} phase. Periodic layers also served as indicators that the U, Mo and Al had significantly different mobility.

In the diffusion couples annealed at 600°C, periodic bands were observed only in the U-7Mo and U-10Mo vs. Al diffusion couples; the U-12Mo vs. Al couple transitioned phase regions from the (UAl_3 + $U_6Mo_4Al_{43}$) to the (UAl_3 + $U_6Mo_4Al_{43}$ + UMo_2Al_{20}) phase regions without periodic layer development. For the case of the diffusion couples annealed at 550°C, only the U-7Mo vs. Al diffusion couples showed the development of periodic bands within the interdiffusion zone. Only the diffusion couple of U-7Mo vs. Al annealed for 1 hour showed clear periodic pattern as shown in Figure 43 (a). The couples of U-7Mo vs. Al annealed for longer times showed that the periodic bands developed, but their morphologies were affected by the γ-U → (α-U + δ-U_2Mo) alloy decomposition. The U-10Mo and U-12Mo vs. Al diffusion couples transitioned phase regions without observable periodic band development. Thus, the development of periodic layering of the interdiffusion zone in U-Mo vs. Al diffusion couples was affected by the Mo concentration in the U-Mo alloy and the anneal temperature. Also, the phase development of the interdiffusion zone does not appear to depend on periodic band formation. Conversely, periodic band formation in the U-Mo vs. Al interdiffusion zones depends on the phase development.

In contrast to the diffusion couples annealed at 600°C, at 550°C decomposition of γ-U to α-U and δ-U_2Mo was expected to take place. Dwight [16], Ivanov et al. [4,17,18], Streets et al. [19] and Comozov et al. [20] reported the $\gamma \rightarrow (\alpha+\delta)$ decomposition. Repas et al. [21] and Goldstein et al. [22] developed Time-Temperature-Transformation (TTT) diagrams for U-8 to 14 wt.% Mo alloys to summarize the γ-phase stability as a function of Mo concentration. Parida et al. [23]

reported the thermodynamic functions to describe the stability of the γ-phase, and several studies have been carried out to examine the influence of Mo-concentration and cooling rate on the γ→(α+δ) decomposition and stability of the γ-phase [50,51,52], including those as dispersion particles [31,33,48,49]. In U-7Mo alloys at 550°C, decomposition was expected to proceed within minutes. In the U-10Mo and U-12Mo alloys, the transformation time was beyond 20 hours, and the γ-U to α-U was not expected or observed as can be seen in the backscatter electron micrographs in Figure 39.

Based on the results of this study, periodic layer formation indicated that the U, Mo and Al had significantly different mobility in the interdiffusion zone. The high mobility of Al was further supported by the observed microstructures at the diffusion front where the γ→(α+δ) decomposition had taken place. Once γ→(α+δ) decomposition had taken place, the Al encountered a two-phase microstructure in the U-Mo alloy, and preferentially diffused through the α-U at a faster rate than in the γ-U phase resulting in expansion of the interdiffusion zone into the α-U. Figure 42 shows the typical microstructural evolution of diffusion couples containing pure U-Mo vs. pure Al where the γ→(α+δ) decomposition had taken place. The γ→(α+δ) transformations evolved as Al-enriched lamellar microstructures in the U-Mo alloy. At the U-Mo/interdiffusion-zone-interface, Al diffused through the α-U phase into the U-Mo alloy to produce the observed microstructures. Typically the overall result was increased interdiffusion rates with thicker and irregular interdiffusion zones. Al penetration into the U-Mo indicated that Al moved faster in the direction of the U-Mo than the Mo or U diffused in the opposite direction; lamellar microstructures could not develop if the U and/or Mo had higher mobility.

5.4.2 U-Mo vs. Al-Si

Diffusion couples of U-7Mo, U-10 and U-12 Mo vs. Al-2Si and Al-5Si were annealed and compared to couples with pure Al at 550°C for 1, 5 and 20 hours. The first and most prominent feature of the addition of Si to the Al was a significant decrease in the growth rate of the interdiffusion zone. Table 4.1 shows that there is approximately an order of magnitude difference in the growth constants between couples with and without Si additions. Although similar in appearance, the average composition of the interdiffusion zone, approximately 75 at.% (Al,Si), showed that Si was present in significant concentrations, and that the Si distribution in the interdiffusion zone varied through its thickness in accordance with Figure 46.

Characterization by TEM determined that the $(U,Mo)(Al,Si)_3$ and UMo_2Al_{20} phases developed throughout the thickness of the interdiffusion zone, and the $U_6Mo_4Al_{43}$ only developed in discrete locations. The SAED and CBED analyses from the U-7Mo vs. Al-2Si and U-7Mo vs. Al-5Si couples annealed at 550°C for 1 and 5 hours, respectively, did not identify any other phases.

An extensive search for the UAl_4 phases was conducted by TEM analysis. This phase did not develop in the interdiffusion zones when Si was present. Based on the phase diagram, the UAl_4 phase has a very low melting point with respect to the UAl_3 and USi_3 phases. The development of the UAl_4 phase is most likely suppressed in favor of the development of the more thermodynamically stable $(U,Mo)(Al,Si)_3$ phase. Thermodynamically, the UAl_3 and USi_3 phases have similar melting points, where that of the USi_3 phase is slightly higher. H.J. Ryu [51,52] showed that the UAl_3 phase is stabilized by Si additions and is de-stabilized by Mo additions. Si-enriched regions in the interdiffusion zones were observed even after 1 hour of diffusion anneal in all diffusion couples. This indicated that Si had a high mobility and was distributed throughout the interdiffusion zones. Because of its higher thermodynamic stability, the USi_3 phase may develop first in the interdiffusion zones, or because of the phase similarities, in conjunction with the UAl_3 phase. Once either phase is developed, Al and Si substitute for each other to develop the $U(Al,Si)_3$ phase; grains with this composition were observed throughout the interdiffusion zone. Si opens the solubility for Mo in this phase; then as a result of further interdiffusion, the $(U,Mo)(Al,Si)_3$ phase developed.

The mechanism that led to the suppression of the $U_6Mo_4Al_{43}$ phase when Si was introduced into the Al is not clearly understood, but it is suspected that one of the intermediate phases that compose the $U_6Mo_4Al_{43}$ phase does not develop, interrupting phase development. Comparison of the Mo-Al [108] and Mo-Si [109] binary phase diagram shows that, in general, all Mo-Si phases possess higher thermodynamic stability (based on melting points) than the Mo-Al phases. Therefore, it is possible that the polyhedral structures of $Mo(U_2Al_{10})$, $MoAl_{12}$ and/or $(Al,Mo)(U_3Al_9)$ cannot develop in Si enriched regions. TEM analysis showed that the regions where the $U_6Mo_4Al_{43}$ phase was observed were depleted in Si, supporting this hypothesis.

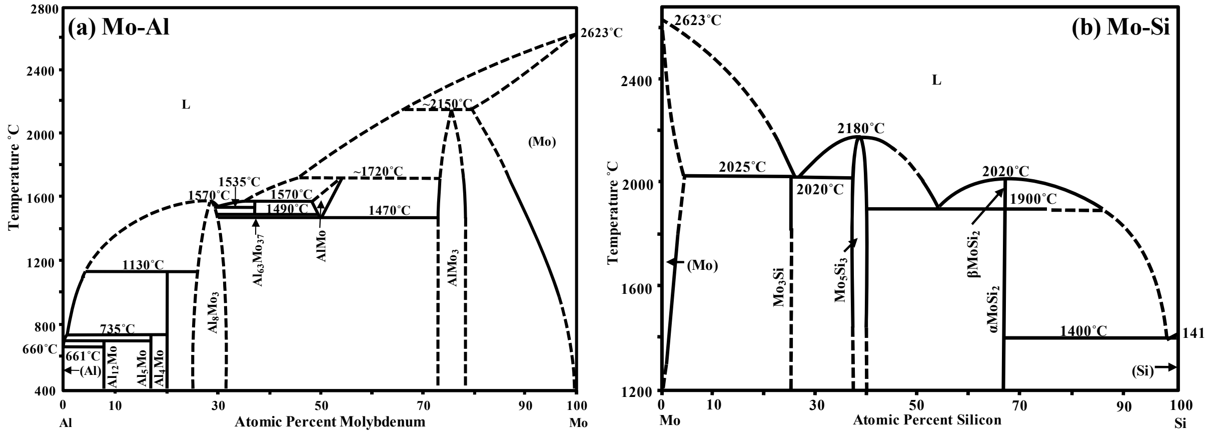

Figure 55. Equilibrium binary phase diagrams for (a) Mo-Al [108] and (b) Mo-Si [109].

The interdiffusion zones in U-Mo vs. Al-Si diffusion couples developed layered morphologies where the layers were characterized by microstructural variations, and by differences in the average composition of each layer. Based on a similar thermodynamic argument, as for the case of the U-Mo vs. Al diffusion couples, in the U-Mo-Al-Si four component system, at constant temperature and pressure, the thermodynamic degrees of freedom are used by growth of the interdiffusion zone and the development of the two- and three-phase regions, {$(U,Mo)(Al,Si)_3$ + UMo_2Al_{20}} and {$(U,Mo)(Al,Si)_3$ + $U_6Mo_4Al_{43}$ + UMo_2Al_{20}}, respectively. Within the two-phase regions in the interdiffusion zone, after considering layer growth, one degree of freedom remains open. Because extra phases were not observed, this degree of freedom appears to have been used to allow solid solubility in the $(U,Mo)(Al,Si)_3$ phase and/or for the development of irregular interfaces. In the three-phase regions, in the quaternary system, three-phase growth is permitted, and the remaining degree of freedom was used for layer growth.

The γ→(α+δ) decomposition of the parent U-Mo alloy was observed in some of the diffusion couples studied. The development of the lamellar microstructures, shown in Figure 2 for the diffusion couple containing U-7Mo vs. Al annealed at 550°C for 5 hours, were not observed in

U-Mo vs. Al-Si diffusion couples. Upon full decomposition of the U-Mo, the interdiffusion zone very near the U-Mo/interdiffusion-zone-interface contained a two phase microstructure. The U-Mo alloy also contained two phases, and the (U,Mo)(Al,Si)$_3$ experienced solid-solubility. The remaining degree of freedom allows the interdiffusion zone to grow. Because all degrees of freedom are accounted for, the interface should resist deformation from a planar interface, even in the presence of decomposed U-Mo alloy.

6. CONCLUSIONS

Interdiffusion and microstructural development in the U-Mo-Al system was examined using solid-to-solid diffusion couples, U-7wt.%Mo, U-10wt.%Mo and U-12wt.%Mo vs. pure Al, annealed at 600°C for 24 hours. Findings from this study are summarized below:

- The interdiffusion zone consisted of layered microstructures with varying amounts of finely dispersed UAl_3, UAl_4, $U_6Mo_4Al_{43}$, and UMo_2Al_{20} phases. The average composition throughout the interdiffusion zone remained approximately constant at approximately 80 at.% Al.

- Interdiffusion microstructure, observed by SEM/TEM/STEM analyses, included two- and three-phase layered microstructures, microcracks, elongated grains, and localized periodic band formation. These observations suggested that several mechanisms were at play in order to develop the observed morphologies. The assumption of significant deviations from thermodynamic equilibrium was not necessary to explain microstructural evolution when internal residual stresses in the interdiffusion zone were considered. Near equilibrium conditions along with variation in molar volumes, saturation with Mo and high mobility of Al in the interdiffusion zone controlled phase development and resulted in the development of periodically layered microstructures.

- The presence of the ternary intermetallic $U_6Mo_4Al_{43}$ in the interdiffusion layer, documented by TEM in this study, appears to be responsible for the development of large internal residual stresses that result in the development of three-phase layers and periodic layering within the interdiffusion zones.

- The $U_6Mo_4Al_{43}$ may be responsible for several deleterious behavior of in reactor applications including amorphization, poor mechanical integrity and void formation during in-reactor irradiation. Methods for the mitigation of this phase by Si addition were reported, and suggestions were made to control its development.

Also, interdiffusion and microstructural development in the U-Mo-Al-Si system was examined using solid-to-solid diffusion couples, U-7wt.%Mo, U-10wt.%Mo and U-12wt.%Mo vs. pure Al, Al-2wt.%Si and Al-5wt.%Si annealed at 550°C for 1, 5 and 20 hours. Findings from this study are summarized below:

- The presence of Si in diffusion couples with Al-Si alloys significantly reduced the growth rate of the interdiffusion zones. In absence of Si, even locally, the γ-U→(α-U+δU_2Mo) decomposition was observed in some of the U-Mo alloys after diffusion anneal, and resulted in increased thickness of the interdiffusion zone and in irregular morphologies. When Si was present in the Al alloy, even though decomposition took place in some alloys, the interdiffusion zones did not develop the lamellar microstructures typical of diffusion couples of U-7Mo vs. pure Al.

- Interdiffusion microstructures, observed by SEM/TEM/STEM analyses, included two- and three-phase layered microstructures with very fine-grained mixtures containing mainly $(U,Mo)(Al,Si)_3$ and UMo_2Al_{20}. Si enriched and Al enriched layers developed distinctively within the interdiffusion zone. Extensive TEM characterization determined that the $U_6Mo_4Al_{43}$ phase scarcely developed in the interdiffusion zone of the U-7Mo vs. Al-2Si and Al-5Si only within the Al-enriched regions.

- Periodic band development did not take place when Si was present in the interdiffusion zone presumably due to a reduction of the internal residual stresses within the interdiffusion zone.

APPENDIX: LIST OF PUBLICATIONS AND CONFERENCE PRESENTATIONS

Journal Publications

1. E. Perez, B. Yao, D.D. Keiser, Jr., Y.H. Sohn, “Role of Si on Interdiffusion Between U-Mo and Al-Si Alloys,” *Metallurgical and Materials Transactions A*, Submitted, February, 2011.

2. B. Yao, E. Perez, D.D. Keiser, Jr., J.F. Jue, C.R. Clark, Y.H. Sohn, “Microstructure characterization of as-fabricated and 475ºC annealed U-7wt.%Mo dispersion fuel in Al-Si alloy matrix,” *Materials Characterization*, Submitted, January, 2011.

3. D.D. Keiser, Jr., J.F. Jue, B. Yao, E. Perez, Y.H. Sohn, C.R. Clark, “Microstructural Characterization of U-7Mo/Al-Si Alloy Matrix Dispersion Fuel Plates Fabricated at 500°C, *Journal of Nuclear Materials*, Accepted for Publication, in Press, 2011.

4. E. Perez, D.D. Keiser, Jr., Y.H. Sohn, “Phase Constituents and Microstructure of Interaction Layer Formed in U-Mo Alloys vs. Al Diffusion Couple Annealed at 600°C,” *Metallurgical and Materials Transactions A*, Accepted for Publication, in Press, 2011.

5. A. Ewh, E. Perez, D.D. Keiser, Jr., Y.H. Sohn, “Characterization of Interaction Layer in U-Mo-X (X = Nb, Ti, Zr) vs. Al Diffusion Couples Annealed at 600°C for 10 hours,” *Defects and Diffusion Forum*, 2011, Accepted for Publication and in Press.

6. E. Perez, B. Yao, D.D. Keiser, Jr., Y.H. Sohn, “Microstructural Analysis of As-Processed U-10wt.%Mo Monolithic Fuel Plate in AA6061 Matrix with Zr Diffusion Barrier,” *Journal of Nuclear Materials*, Vol. 402 (2010) pp. 8-14.

7. A. Ewh, E. Perez, D.D. Keiser, Jr., Y.H. Sohn, “Microstructural Characterization of U-Nb-Zr, U-Mo-Nb, and U-Mo-Ti Alloys via Transmission Electron Microscopy,” *Journal of Phase Equilibria and Diffusion*, Vol. 31 (2010) pp. 216-222.

8. E. Perez, A. Ewh, J. Liu, B. Yuan, D.D. Keiser, Y.H. Sohn, “Transmission Electron Microscopic Study of Phase Constituents in Al-rich U-Mo-Al Alloys,” *Journal of Nuclear Materials*, Vol. 394 (2009) pp. 160-165.

9. E. Perez D.D. Keiser, Jr., Y.H. Sohn “Phase Constituents and Growth Kinetics of Aluminides in U-Mo vs. Al Diffusion Couples,” *Defects and Diffusion Forum*, Vol. 289-92 (2009) pp. 41-49.

10. E. Perez, N. Hotaling, A. Ewh, D.D. Keiser, Y.H. Sohn, “Growth Kinetics of Intermetallic Phases in U-Mo vs. Al Alloy Diffusion Couples at 550ºC,” *Defects and Diffusion Forum*, Vol. 266 (2007) pp. 149-156.

11. Y.H. Sohn, E. Perez, N. Garimella, R. Mohanty, J. Liu, “Integrated, Effective and Average and Their Applications in Multicomponent Alloys for Energy Production Systems,” *Defects and Diffusion Forum*, Vol. 258-260 (2007) pp. 346-359.

Peer Reviewed Conference Proceedings

1. D.D. Keiser, Jr., B. Yao, E. Perez, Y.H. Sohn, “SEM and TEM Characterization of As-Fabricated U-Mo Dispersion Fuel Plates,” Proceedings of the 31st International Meeting on Reduced Enrichment for Research and Test Reactors (RERTR 2009), November 1-5, 2009, Beijing, China, INL/CON-09-17107.

2. E. Perez, D.D. Keiser, Jr., Y.H. Sohn, “Interdiffusion Kinetics and Phase Development in Solid-to-Solid Diffusion Couples: U-Mo vs. Al and Ai-Si at 550°C,” Proceedings of the 31st International Meeting on Reduced Enrichment for Research and Test Reactors (RERTR 2009), November 1-5, 2009, Beijing, China, INL/CON-09-17105.

Invited Presentations

1. Y.H. Sohn, E. Perez, B. Yao, A. Ewh, D.D. Keiser, Jr., “Selected Observations from Interdiffusion Study in U-Mo-Al System,” Invited Presentation at 2011 TMS Annual Meeting & Exhibition: Hume-Rothery Symposium Thermodynamics and Diffusion Coupling in Alloys - Application Driven Science in honor of Prof. John Agren, February 27 - March 3, 2011, San Diego, California, USA.

2. A. Ewh, E. Perez, D.D. Keiser, Jr., Y.H. Sohn, “Characterization of Interaction Layer in U-Mo-X (X = Nb, Ti, Zr) vs. Al Diffusion Couples Annealed at 600°C for 10 hours,” Invited Presentation at the 6th International Conference on Diffusion in Solids and Liquids (DSL-2010), July 5-7, Paris, France.

3. Y.H. Sohn, E. Perez D.D. Keiser, Jr., "Phase Constituents and Growth Kinetics of Aluminides in U-Mo vs. Al Diffusion Couples," Invited Presentation at the 7th International Conference on Diffusion in Materials, October 28-31, 2008, Lanzarote - Canary Island, Spain.

4. E. Perez, D.D. Keiser, Jr., Y.H. Sohn, "U-Mo vs. Al Diffusion Couples: Fuel-Cladding Interactions," Invited Presentation at the 2008 National Institute of Standards and Technology Diffusion Workshop, May 12 – 13, 2008, Gaithersburgh, Maryland, USA.

Contributing Presentations

1. E. Perez, B. Yao, D.D. Keiser, Jr., Y.H. Sohn, "Role of Si on Interdiffusion Between U-Mo and Al-Si Alloys," The Nuclear Materials Conference, October 4-7, 2010, ZKM, Karlsruhe, Germany.

2. E. Perez, Y.H. Sohn, D.D. Keiser, Jr., "Growth Kinetics and Phase Development in Diffusion Couples: U-Mo vs. Al-Si," Presented at 2010 TMS Annual Meeting & Exhibition: Symposium on Nuclear Energy Processes and Policies, February 14-18, 2010, Seattle, WA, U.S.A.

3. D.D. Keiser, Jr., J. Jue, B. Yao, E. Perez, Y.H. Sohn, "TEM Characterization of a Monolithic U-Mo Plate-Type Nuclear Fuels," Presented at 2010 TMS Annual Meeting & Exhibition: Symposium on Nuclear Energy Processes and Policies, February 14-18, 2010, Seattle, WA, U.S.A.

4. D.D. Keiser, Jr., B. Yao, E. Perez, Y.H. Sohn, "SEM and TEM Characterization of As-Fabricated U-Mo Dispersion Fuel Plates," Presented at 31st International Meeting on Reduced Enrichment for Research and Test Reactors (RERTR 2009), November 1-5, 2009, Beijing, China.

5. E. Perez, Y.H. Sohn, D.D. Keiser, Jr., "Growth Kinetics and Phase Development in Diffusion Couples: U-Mo vs. Al-Si," To be Presented at 31st International Meeting on Reduced Enrichment for Research and Test Reactors (RERTR 2009), November 1-5, 2009, Beijing, China.

6. E. Perez, D.D. Keiser Jr., Y.H. Sohn, "Effects of Silicon on Interdiffusion Behavior of U-7Mo, U-10Mo and U-12Mo Alloys in Contact with Al, Al-2Si, and Al-5Si alloys at 550°C,"

7. E. Perez, B. Kempshall, A. Ewh, D.D. Keiser, Y.H. Sohn, “Interdiffusion Microstructure of U-Mo vs. Al Diffusion Couples Annealed at 600°C for 24 hours,” Presented at 2009 TMS Annual Meeting & Exhibition: Symposium on Diffusion in Materials for Energy Technologies, February 15-19, 2009, San Francisco, CA, U.S.A.

8. E. Perez, D.D. Keiser, Y.H. Sohn, “Interdiffusion and Microstructural Development of U-7Mo, U-10Mo and U-12Mo Alloys in Contact with Al, Al-2Si, Al-5Si, 6061Al and 4043Al alloys at 550°C,” Presented at 2009 TMS Annual Meeting & Exhibition: Symposium on Diffusion in Materials for Energy Technologies, February 15-19, 2009, San Francisco, CA, U.S.A.

9. A. Ewh, E. Perez, D.D. Keiser, Jr., Y.H. Sohn, Interdiffusion in U-Mo-X (X = Nb, Ti, Zr) vs. Al Diffusion Couples,” Presented at 2009 TMS Annual Meeting & Exhibition: Symposium on Diffusion in Materials for Energy Technologies, February 15-19, 2009, San Francisco, CA, U.S.A.

10. E. Perez, D.D. Keiser, Jr., Y.H. Sohn, “Interdiffusion Microstructure in U-Mo vs. Al Diffusion Couples,” Presented at Materials Science and Technology 2008 Conference: Symposium on Phase Stability, Diffusion Kinetics and Their Applications – PSDK III, October 5-9, 2008, Pittsburgh, Pennsylvania, U.S.A.

11. E. Perez, A. Ewh, N. Hotaling, D.D. Keiser, Y.H. Sohn, ”Phase Constituents in Al-rich U-Mo-Al Alloys,” Presented at Materials Science and Technology 2007 Conference and Exhibition, September 16-20, 2007, Detroit, Michigan, USA.

12. E. Perez, N. Hotaling, A. Ewh, D.D. Keiser, Y.H. Sohn, ”Diffusional Growth of Reaction Layer in Diffusion Couples Between U-Mo and Al Alloys,” Presented at Third International Conference on Diffusion in Solids and Liquids, July 4-7, 2007, Algarve, Portugal.

13. E. Perez, N. Hotaling, A. Ewh, Y.H. Sohn, D.D. Keiser, “Interdiffusion behavior in U-7, 10 and 12 wt.%Mo Alloys in Contact with Al Alloys at 500 and 600°C,” Presented TMS 2007: 136th Annual Meeting and Exposition, February 25 – March 1, 2007, Orlando, FL, USA.

REFERENCES

1. D.D. Keiser Jr., Def. Diff. Forum, 266, 2007, pp. 131-48.

2. Federal Register, Rules and Regulations, Vol. 51, No. 37, Feb. 25, 1986.

3. J.L. Snelgrove, G.L. Hofman, M.K. Meyer, C.L. Trybus, T.C. Wiencek, Nucl. Eng. And Des., 178, 1997, pp. 119.

4. O.S. Ivanov, T.A. Badaeva, R.M. Sofronova, V.B. Kishenevshii, N.P. Kushnir, O.S. Ivanov, Phase Diagrams of Uranium Alloys, Amerind Publishing Co. Pvt. Ltd., New Delhi, 1983.

5. D. Ahmann, A.L. Snow, A.S. Wilson, "The Uranium-Molybdenum binary system", 1945, CT-2946.

6. P.C.L. Pfeil, , J. Inst. Metals, 77, 1950, pp. 553.

7. P.C.L. Pfeil, , J. Inst. Metals, 78, 1950-1951, pp. 762.

8. A.U.Seybold, R.K. McKechnie. J Inst. Metals, 78, 1950-1951, pp. 760.

9. C.W. Tucker, J. Inst. Metals, 78, 1950-1951, pp. 760.

10. H.A. Saller, F.A. Rough, D.A. Vaughan. The constitution diagram of uranium-rich uranium-molybdenum alloys, BMI-72, 1951.

11. H.A. Saller, F.A. Rough, D.C. Bennet. The constitution diagram of uranium-rich uranium-molybdenum alloys, BMI-730, 1952.

12. P.L.C. Pfeil, J.D. Browne. Superlattice formation in uranium-molybdenum alloys. AERE M/R 1333, 1954.

13. E.K. Halteman, Acta crystallogr. 10, 1957, pp.166.

14. O.S. Ivanov, T.A. Badaeva. Trudi Vtorio Mezhdunarodnoi energii. T. 3. Yadernoe goryuchee I reaktornye materialy (Proceedings of the Second U.N. International Conference on the Peaceful Uses of Atomic Energy, Vol. 3, Nuclear Fuels and Reactor Materials). Atomizdat, 1959, pp.347.

15. O.S. Ivanov, A.S. Zaimovskii and others. Trudi Vtorio Mezhdunarodnoi Konferentsii po mirnomu ispol'zovaniyu atomnoi energii. T. 3. Yadernoe goryuchee I reaktornye materialy (Proceedings of the Second U.N. International Conference on the Peaceful Uses of Atomic Energy, Vol. 3, Nuclear Fuels and Reactor Materials). Atomizdat, 1959, p.396.

16. A.E. Dwight, Jour. Nucl. Mater., Vol. 2, No. 1 (1960) p.81.

17. O.S. Ivanov, T.A. Badaeva, A.T. Semenchenkov, R.I. Kuznetsova. Sb. "Stroenie splavov nekotorykh sistem s uranom i toriem (Collection of the Structure of Alloys of Some Systems with Uranium and Thorium). Atomizdat, 1961, p.48.

18. O.S. Ivanov, A.T. Semenchenkov, N.I. Kozlov. Sb. "Stroenie splavov nekotorykh sistem s uranom i toriem (Collection of the Structure of Alloys of Some Systems with Uranium and Thorium). Atomizdat, 1961, p.68.

19. F.G. Streets, J.J. Stobo, J. Inst. Metals, 92, N6 (1964), p.171.

20. L.I. Gomozov, E.M. Lyntina, O.S. Ivanov. Izv. AN SSSR, Metally (1970).

21. P.E. Repas, R.H. Goodenow, R.F. Hehemann, Trans. ASM, Vol. 57 (1964), p.150.

22. Y. Goldstein, A. Bar-Or, Jour. Inst. Metals., Vol. 95 (1967) p.17.

23. S.C. Parida, S. Dash, Z. Singh, R. Prasad, V. Venugopal, Jour of Phys. Chem. of Solids., 62, (2001) p.585.

24. R.F. Hills, B.R. Butcher, J.A. Heywood, Jour. Less-Common Metals, 3 (1961), p. 155.

25. R.F. Hills, B.W. Howlet, B.R. Butcher, Jour. Less-Common Metals, 5 (1963), p. 369.

26. G.H. May, Jour. Nucl. Mater., 7, No.1 (1962) p.72.

27. D.J. Marsh, G.F. Slattery, J.H. Gittus, Jour. Inst. Metals. (1965), p. 260.

28. G.I. Terekhov, Izvestiya Akademii Nauk SSSR. Metally, No. 2, (1987) p.197.

29. Konobeevsky, Pravdyuk, Kutaitsev, Proceedings of the International Conference of the Peaceful Uses of Atomic Energy, 7 (1956), p.433.

30. S.T. Konobeevsky, Jour. Nucl. Energy, 1, (1956), p.356.

31. J.-S. Lee, C.-H. Lee, K.H. Kim, V. Em, Jour. Nucl. Mater. , 280 (2000), p.116.

32. Y.V. Vamberskiy, A.L. Udovskiy, O.S. Ivanov, Jour. Nucl. Mater., 46 (1973), p. 192.

33. K.H. Kim, D.B. Lee, C.K. Kim, G.E. Hofman, Jour. Nucl. Mater., 245 (1997), p.179.

34. V.K. Orlov, M.V. Teplinskaya, Atomic Energy, Vol. 86, 2 (1999) p.118.

35. A.V. Vatulin, A.V. Morozov, V.B. Suprun, Y.I. Petrov, Y.I. Trifonov, Mt. Sci. & Heat Treat., Vol. 46, No. 11, (2004) p.484.

36. M.L. Bleiberg, L.J. Jones, B. Lustman, Jour. Appl. Phys., Vol 27, No. 11 (1956), p.1270.

37. M.L. Bleiberg, Nucl. Sci. & Eng., 5 (1959) p.78.

38. M.L. Bleiberg, Jour. Nucl. Mater., 2 (1959) p.182.

39. M.K. Meyer, G.L. Hofman, S.L. Hayes, C.R. Clark, T.C. Wiencek, J.L. Snelgrove, R.V. Strain, K.–H. Kim, Jour. Nucl. Mater., 304 (2002), p.221.

40. A. Leenaers, S. Van den Berghe, E. Koonen, C. Jarousse, F. Huet, M. Trotabas, M. Boyard, S. Guillot, L. Sannen, M. Verwerft, Jour. Nucl. Mater., 335 (2004) p.39.

41. A.V. Vatulin, A.V. Morozov, V.B. Suprun, Y.I. Petrov, Y.I. Trifonov, Atomic Energy, Vol. 100, 1, (2006) p.37.

42. S.V. Berghe, W.V. Renterghem, A. Leenaers, J. Nucl. Mater., 375 (2008) p.340.

43. H. Palancher, N. Wieschalla, P. Martin, R. Tucoulou, C. Sabathier, W. Petry, J.-F. Berar, C. Valot, S. Dubois, Jour. Nucl. Mater., 385 (2009), p.449.

44. DOE Fundamentals Handbook, Materials Science, Vol 2 of 2. U.S. Department of energy, FSC-6910, Materials Science Module 5 Plant Materials, DOE-HDBK-1017/2-93 p.49.

45. D.B. Lee, K.H. Kim, C.K. Kim, Jour. Nucl. Mater., 250 (1997) p.79.

46. S.H. Lee, J.C. Kim, J.M. Park, C.K. Kim, S.W. Kim, Int. Jour. Thermophys., Vol. 24, 5, (2003), p.1355.

47. S.H. Lee, J.M. Park, C.K. Kim, Int. Jour. Thermophysics, 28, 5 (2007) 1578.

48. B.-S. Seong, C.H. Lee, J.-S. Lee, H.-S. Shim, J.-H. Lee, K.H. Kim, C.K. Kim, V.Em. Jour. Nucl. Mater. 277 (2000) p.274.

49. V.P. Sinha, G.J. Prasad, P.V. Hedge, R. Keswani, C.B. Basak, S. Pal, G.P. Mishra, Journal of Alloys and Compounds, 473 (2009), p.238.

50. J.-S. Lee, C.-H. Lee, K. H. Kim, V. Em, Jour. Nucl. Mater., 306 (2002) p.147.

51. H.J. Ryu, Y.S. Han, J.M. Park, S.D. Park, C.K. Kim, Jour. Nucl. Mater., 321 (2003) p.210.

52. H.J. Ryu, J.M. Park, C.K. Kim, G.L. Hofman, Jour. Phase Equil. and Diff., Vol 27, No. 6, (2006) p.651.

53. D.D. Keiser Jr., Def. Diff., Vol. 266 (2007) p.131.

54. E. Perez, N. Hotaling, A. Ewh, D.D. Keiser, Y. H. Sohn, Def. Diff., Vol. 266 (2007) p.149.

55. M.I. Mirandou, S. Balart, M. Ortiz, M.S. Granovsky, Jour. Nucl. Mater., 323 (2003) p.29.

56. H. Palancher. P. Martin, V. Nassif, R. Tucoulou, O. Proux, J.-L.- Hazemann, O. Tougait, E. Lahéra, F. Mazaudier, C. Valot, S. Dubois, Jour. Appl. Cryst. 40 (2007) p.1064.

57. F. Mazaudier, C. Proye, F. Hodaj, Jour. Nucl. Mater, 377 (2008) p.476.

58. M.I. Mirandou, S.F. Arico, S.N. Balart, L.M. Gribaudo, Mat. Char. 60 (2009) p. 888.

59. E. Perez, D.D. Keiser, Y.H. Sohn, Def. Diff. Forum, Vols. 289-292 (2009) p.41.

60. D.D. Keiser Jr., C.R. Clark, M.K. Meyer, Scripta Mater. 51 (2004) p.893.

61. H. Noél, O. Tougait, S. Dubois, Jour. Nucl. Mater., 389 (2009) p.93.

62. E. Perez, A. Ewh, J. Liu, B. Yuan, D.D. Keiser Jr., Y.H. Sohn, Jour. Nucl. Mater., 394 (2009) p.160.

63. J. Gan, D.D. Keiser Jr., D.M. Wachs, A.B. Robinson, B.D. Miller, T.R. Allen, Jour. Nucl Mater., 396 (2010) p.234.

64. K.H. Kim, J.M. Park, C.K. Kim, G.L. Hofman, M.K. Meyer, Nucl. Eng. Des., 211 (2002) p229.

65. H.J. Ryu, Y.S. Kim, G.L. Hofman, Jour. Nucl. Mater, 385 (2009) p.623.

66. D.D. Keiser Jr., A.B. Robinson, J.F. Jue, P. Medvedev, D.M. Walch, M. R. Finlay, Jour. Nucl. Mater, 393 (2009) p.311.

67. H. Etherington, Nuclear Engineering Handbook, McGraw Hill Book Company, Inc., York, PA, (1958), p.12-54.

68. J.E. Matos, J.L. Snelgrove, “Research reactor core conversion guidebook, Vol 4, IAEA, IAEA-TECDOC-643.

69. D. Stahl, “Nuclear Converter Reactor Fuel Cycle Technology”, ANL-83-5, DE83 014267, 1982.

70. H. Okamoto, Journal of Phase Equilibria and Diffusion, Vol. 12, 2 (1991) p.148.

71. R.W.G. Wyckoff, Crystal Structures, 2nd ed., Wiley, New York, (1965).

72. C. W. Jacob, B. E. Warren, Jour. Am. Chem. Soc., Vol. 59, 12, (1937) p.2588.

73. E.K. Halteman, Acta Crystallogr., Vol. 10 (1957) p.166.

74. N. Ridley, J. Less-Common Metals, 8, (1965) p.354.

75. H.E. Swanson, E. Tatge, Natl. Bur. Stand. (U.S.), Circ. 539, Vol. I (1953) p.11.

76. C.R. Hubbard, H.E. Swanson, F.A. Mauer, Jour. Appl. Crystallogr., 8 (1975) p.45.

77. T.B. Massalski, H. Okamoto, P.R. Subramanian, L. Kacprzak, W.W. Scott, Jr., M.A. Fleming, R. Boring, A. Losasso, Binary alloy phase diagrams Vol. 1, Metals Park (OH): ASM; 1990. p.211.

78. A.E. Dwight, Argone Nat. Lab., UC-25, ANL-82-14 (1982).

79. C.-K. Rhee, S.-I. Pyun, I.-H. Kuk, J. Nucl. Mater., 184 (1991), p.161.

80. M. Ugajin, M. Akabori, A.itoh, N. Ooka, Y. Nakakura, J. Nucl. Mater., 248, (1997), p.204.

81. J.W. Richardson Jr., R.C. Birtcher, S.-K. Chan, Physica B, 241-243 (1998), p.390.

82. M.R. Finlay, G.L. Hofman, J.L. Snelgrove, J. Nucl. Mater., 325, (2004), p.118.

83. Y.S. Kim, G.L. Hofman, J. Rest, A.B. Robinson, J. Nucl. Mater., 389, 2009, p.443.

84. H.J. Ryu, Y.S. Kim, G.L. Hofman, J.M. Park, C.K. Kim, J. Nucl. Mater., 358, (2006), p.52.

85. M. Mirandou, S. Aricó, M. Rosenbusch, M. Ortiz, S. Balart, L. Gribaudo, J. Nucl. Mater., 384 (2009). P.268

86. D.D. Keiser Jr., J. Gan, J.F. Jue, B.D. Miller, C.R. Clark, Mater. Char., 61 (2010) p.1157.

87. E. Perez, B. Yao, Y.H. Sohn, D.D. Keiser Jr. Proc. of RERTR 2009, Nov. 1-5, 2009, Beijing, China.

88. J. Allenou, H. Palancher, X. It is, M. Cornen, O. Tougait, R. Tucoulou, E. Welcomme, Ph. Martin, C. Valot, F. Charollais, M.C. Anselmet, P. Lemoine, J. Nucl. Mater., 399, (2010), p.189.

89. P. Villars, L. Calvert, Pearson's Hbk. Cryst. Data for Intermetallic Phases, 2nd Ed. Materials Park, OH (1991) p.1027.

90. P. Villars, L. Calvert, Pearson's Hbk. Cryst. Data for Intermetallic Phases, 2nd Ed. Materials Park, OH (1991) p.1028.

91. B.S. Borie Jr., Jour. of Metals (1951) p.800.

92. V.Y. Zenou, G. Kimmel, C. Cotler, M. Aizenshtein, Jour. of Alloys and Comp., 329 (2001) p.189.

93. W. Jeitschko, W. Wilhelms Univ., Munster, Germany. ICDD Grant-in-Aid (1994).

94. W. Jeitschko, W. Wilhelms-Univ., Munster, Germany. ICDD Grant-in-Aid (1996).

95. S. Niemann, W. Jeitschko, Z. Metallkd. 85 (1994), 5, p. 345.

96. X. Chu, S.A. Barnet, Jour. Appl. Phys, 77, Vol. 9, (1995), p.4403.

97. S. Niemann, W. Jeitschko, Jour. Solid State Chem., 116, (1995) p.131.

98. S. Niemann, W. Jeitschko, Jour. Solid State Chem., 114, (1995) p.337.

99. V.A. van Rooijen, E.W. van Royen, J. Vrijen, S. Radelaar, Acta Metallurgica, Vol. 23 (1975) p. 987.

100. K. Osinski, A. W. Vriend, G.F. Bastin, F.J.J van Loo, Zeitschrift fur Metallkunde, Vol. 73, 4, (1982), p. 258.

101. M.R. Rijnders, A.A. Kodentsov, Cs. Cserháti, J. van den Akker, F.J.J. van Loo, Defect Diff. Forum, Vols. 129-130 (1996) p.253.

102. M.R. Rijnders., A.A. Kodentsov, J.A. van Beek, J. van den Akker, F.J.J. van Loo, Solid State Ionics, 95 (1997), p.51.

103. A.A. Kodentsov, M.R. Rijnders, F.J.J. van Loo, Acta Mater., Vol. 46, 18 (1998), p. 6521.

104. X. Su, C.L.S. Yang, F. Yin, J. Wang, Scripta Mater., 62 (2010) p. 485.

105. C. Wagner, J. Colloid Sci., Vol. 5 (1950) p. 85.

106. T.B. Massalski, H. Okamoto, P.R. Subramanian, L. Kacprzak, W.W. Scott, Jr., M.A. Fleming, R. Boring, A. Losasso, Binary alloy phase diagrams Vol. 1, Metals Park (OH): ASM; 1990. p.230.

107. T.B. Massalski, H. Okamoto, P.R. Subramanian, L. Kacprzak, W.W. Scott, Jr., M.A. Fleming, R. Boring, A. Losasso, Binary alloy phase diagrams Vol. 3, Metals Park (OH): ASM; 1990. p. 3374.

108. T.B. Massalski, H. Okamoto, P.R. Subramanian, L. Kacprzak, W.W. Scott, Jr., M.A. Fleming, R. Boring, A. Losasso, Binary alloy phase diagrams Vol. 1, Metals Park (OH): ASM; 1990. p. 174.

109. T.B. Massalski, H. Okamoto, P.R. Subramanian, L. Kacprzak, W.W. Scott, Jr., M.A. Fleming, R. Boring, A. Losasso, Binary alloy phase diagrams Vol. 3, Metals Park (OH): ASM; 1990. p.2664.

110. Kaufmann et al. Jour. Met., Vol.9 (1957) p.23.